STUDIES OF LIPID BILAYER STRUCTURE AND DYNAMICS

STUDIES OF LIPID BILAYER STRUCTURE AND DYNAMICS

By

MARTIN D. KAYE, B.Sc.

A Thesis
Submitted to the School of Graduate Studies
in Partial Fulfillment of the Requirements
for the Degree
Master of Science

McMaster University
©Copyright by Martin D. Kaye, 2011.

MASTER OF SCIENCE (2011) McMaster University
(Physics) Hamilton, Ontario

TITLE: Studies of lipid bilayer structure and dynamics

AUTHOR: Martin D. Kaye, B.Sc.(University of New Brunswick)

SUPERVISOR: Dr. Maikel Rheinstädter

NUMBER OF PAGES: xi, 111

Abstract

The biological membrane is one of the fundamental components in nature, however it is still not well understood. The variety of lipids and other macromolecules found in the membrane makes it very difficult to discern its properties in vivo. Lipid bilayers form the backbone of biological membranes and provide an ideal model system with which to study membrane function and properties. Here we present the results of studies of lipid bilayer structure and dynamics with neutron and x-ray scattering techniques. In particular, the diffusion of single solid supported bilayers and the collective dynamics of lipid-ethanol systems were studied. The first observations of single bilayer diffusion with quasi-elastic neutron scattering are presented. Single solid supported bilayers of 1,2-dimyristoyl-sn-glycero-3-phosphatidylcholine (DMPC) were prepared and examined with a backscattering spectrometer. Diffusion constants were found to be consistent with multilamellar systems. Single solid supported bilayer diffusion was also found to exhibit a continuous character with enhanced diffusion at the nearest neighbour distance.

Investigations of the effects of ethanol on collective lipid tail dynamics are also presented. Highly oriented multilamellar solid supported DMPC bilayers were prepared and immersed in a 5% ethanol/water solution. Inelastic neutron scattering experiments and all atom molecular dynamics simulations reveal the presence of a new low-energy dynamic mode in the lipid tails of DMPC-ethanol systems. This mode exhibits little dispersion and appears in addition to the high energy acoustic mode associated with lipid tail fluctuations in pure lipid systems, which is also observed. Both modes demonstrate in-plane and perpendicular character which may be related to the transport of small molecules through the membrane core. Additional x-ray diffraction studies of DMPC-ethanol systems hydrated from the vapour phase demonstrate that lipid tail fluctuations in DMPC-ethanol systems exhibit lengthscales equal or less than the thickness of the bilayer.

Acknowledgements

I would like to acknowledge the contributions of my collaborators Dr. Mounir Tarek, Dr. Karin Schmalzl and Valeria Conti Nibaldi for their help with the simulations and phonon analysis. I would also thank Dr. Madhusudan Tyagi and Dr. Timothy Jenkins for their expertise with the single bilayers.

Without the use of a neutron beam, none of this would have been possible, so I would acknowledge the institutions who graciously allowed our experiments: Chalk River Laboratories Canadian Neutron Beam Centre, Oak Ridge National Labs Spallation Neutron Source, The Institut Laue Langevin and National Institute for Standards and Technology Center for Neutron Research. The instrument scientists at these institutions were also indispensible: Dr. Michaela Zamponi and Dr. Eugene Mamontov (BASIS), Dr. Georg Ehlers (CNCS), Dr. Norbert Kùcerka and Dr. Zahra Yamani (CNBC N5). I would also like to acknowledge the various agencies which funded this research, including NSERC, CFI and NRC.

Special thanks goes out to the members of our lab group. Thanks to Clare Armstrong and Matthew Barrett for supporting me at every turn and being an all-around amazing scientists. In addition I'd like to thank a few students in the office including Josh McGraw, Mark Healey and Andreas Deschner for late night science chats and general inspiration. Thank go to Jessica Carvahlo for the help with my thesis and to Philip Ashby for late night latex help.

Finally I would like to thank my supervisor Prof. Maikel C. Rheinstädter who has been a great inspiration and a positive force for science in biophysics.

Contents

List of Figures

LIST OF FIGURES

List of Tables

LIST OF TABLES

List of Symbols

APTES	3-Aminopropyltriethyloxysilane
BLADE	Biological Large Angle Diffraction Experiment
DMPC	1,2-dimyristoyl-sn-glycero-3-phosphatidylcholine
GMV	Giant multilamellar vesicle
$\mathbf{L}_{\alpha}$	Lamellar fluid phase
$\mathbf{L}_{\beta'}$	Lamellar gel phase
$\mathbf{P}_{\beta'}$	Lamellar ripple phase
PEG	Polyethyleneglycol
SLB	Single lipid bilayer
SNS	Spallation Neutron Source
SUV	Small unilamellar vesicle
TFE	2,2,2-trifluoroethanol

LIST OF TABLES

Introduction

In terms of biology, there is no more important unit than the cell. Cells are the building blocks which make up most complex organisms on Earth. However, in order to make a cohesive unit, the cell needs a mechanism to separate itself from the surrounding environment. This mechanism is the biological membrane, which is ubiquitous throughout biology. Biological membranes are the primary interface between the cell and the surrounding environment and as a result understanding membrane structure and function is critical to our understanding of inter-cellular communication, cell permeability, tissue formation, and important cell processes such as cell division and apoptosis. This is particularly important in medicine, where membrane properties can impact drug delivery, vein and artery clogging and neurodegenerative disorders such as Alzheimers disease. These are only several of many reasons why the study of biological membranes is quickly becoming a popular field.

There have been many studies which describe the basic structure of biological membranes. These have shown that membranes are composed of lipid molecules arranged in a bilayer which act as a barrier to the cell interior. This bilayer has long been considered a simple passive barrier, however dynamic membrane processes such as mitosis or vesicle formation seem to indicate that lipid bilayers play a much more active role in membrane function. As a result, the investigation of the molecular structure and dynamics of lipid bilayers may reveal more about their role in membrane function and properties. The diversity and composition of biological membranes is also believed to play an important role in membrane function. Although lipid bilayers form the backbone of the membrane, molecules such as proteins, cholesterols and

short chain alcohols also participate in biological membranes. Macromolecules such as cholesterol and short chain alcohols are known to impact membrane properties such as elasticity and permeability. However the mechanism by which these effects are achieved is still unknown. The impact of these membrane active macromolecules on lipid bilayer structure and dynamics may reveal how they modify membrane properties.

While the dynamics of lipid bilayer systems have been examined for decades, the microscopic motions of lipids themselves remain a matter of much debate. The impact of collective lipid dynamics on membrane properties is also of interest. In this document, investigations of lipid bilayer structure and dynamics with x-ray and neutron scattering will be detailed. In particular the examination of diffusion in solid supported bilayers and the impact of ethanol on lipid bilayer collective dynamics will be discussed. The first observations of single solid supported bilayer diffusion with quasi-elastic neutron scattering are presented. Investigations of the collective dynamics of lipid-ethanol systems with inelastic neutron scattering and complimentary x-ray diffraction experiments are discussed. A review of lipid bilayer structure and morphology is also presented as well as a discussion of the role of macromolecules in lipid bilayer structure and properties. The preparation of both the single solid supported and highly oriented multilamellar solid supported lipid bilayers is also detailed. A discussion of the neutron and x-ray scattering instrumentation employed in these experiments is provided as well as an overview of scattering theory.

Chapter 1

Model membranes

Biological membranes are complex, multi-scale materials which demonstrate structure and dynamics over a large range of length and time scales. Singer and Nicholson first described the membrane as a selectively permeable fluid array of lipids, proteins and macromolecules such as cholesterol, peptides and proteins [1]. The animal plasma membrane is composed of a sythesis of an extracellular matrix containing sugars, protein protrusion and lipid headgroups, a liquid crystalline lipid-protein layer and an intracellular cytoskelleton which supports the membrane and gives its shape [2]. The variety of lipids, proteins, cholesterols, alcohols and sugars present in biological membranes (as demonstrated in Figure 1.1), often make biological membranes too complex for physical studies. However, lipids self-assemble into a two-dimensional bilayer which forms the backbone of the membrane and provides a fluid matrix for other macromolecular inclusions. The ordered nature of these bilayers make them an ideal model system for membrane structure and dynamics.

1.1 Lipids

Lipids, along with proteins, nucleic acids and sugars, are one of the four basic building blocks of life [4]. Over 30000 naturally occurring chemical structures and isomers are classified as lipids, which are known to play a role in energy storage, signalling processes and of course cellular membranes [5]. In general, lipids can be described as amphipathic (amphiphilic) molecules composed of an elongated hydrophobic domain,

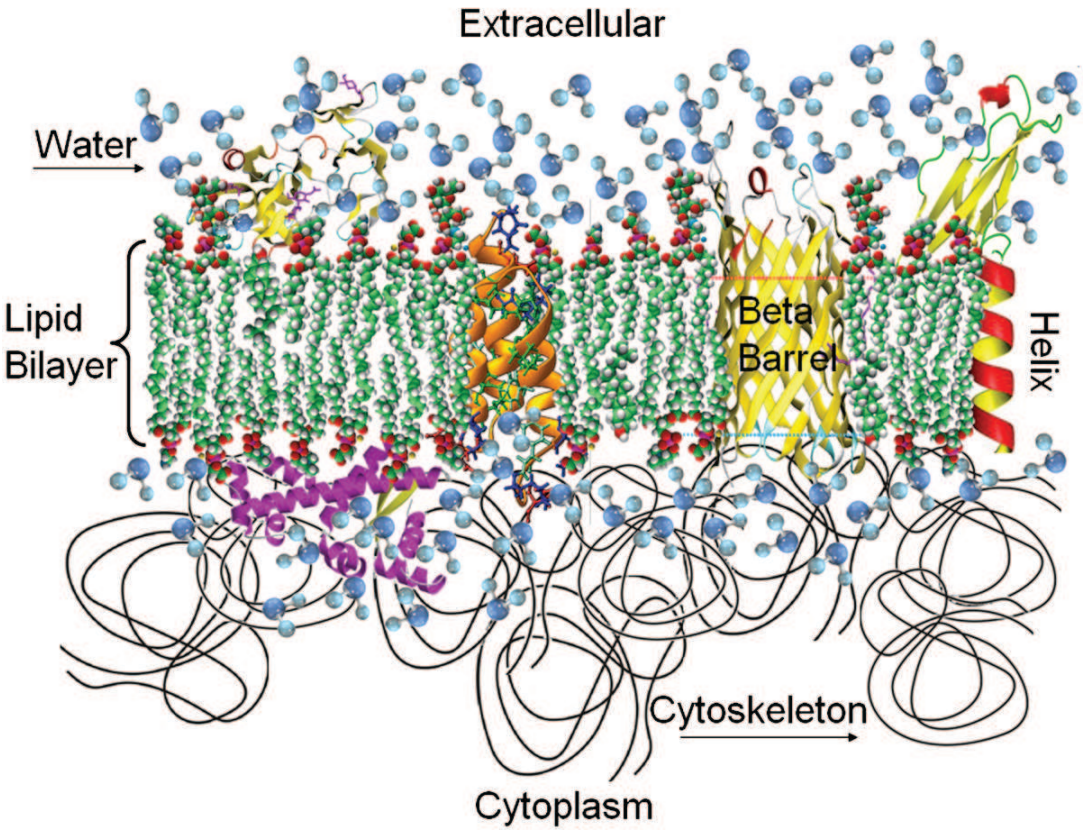

Figure 1.1: A schematic of a cellular plasma membrane. The membrane contains a variety of molecules including proteins, sterols, alcohols, water, proteins and sugars. The primary component are lipids, which form a bilayer, acting as a backbone for other molecules [3].

a semipolar backbone and a head group [2, 4]. The hydrophobic domain is typically made up of one or more fatty acid chains, or 'tails'. Fatty acid chains are composed primarily of tightly packed non-polar CH_2 groups which prevent Hydrogen bonding and ensure hydrophobicity. These chains are attached to the backbone, which is a molecule such as sterol, glycerol or sphingosine. Backbone molecules have two or more functional groups (hydroxyl for glycerol) which bond preferentially with non-polar fatty acids or headgroup. The polar headgroup may be a sugar, amino acid or other functional group and is bound to the remaining backbone group. Common backbone and headgroup molecules are shown in Figure 1.2b. To date eight broad categories of lipid have been identified (classified by their backbone) [6], three of which are the primary constituents of biological membranes: glycerophospholipids, sphyngolipids and glycerolipids. Glycerolipids such as diacylglycerol and triacylglycerol, which have two and three acyl tails respectively, are found in animal membranes at concentrations of up to 8% by mass [2]. Sphingolipids are unique because their bases (most commonly amino alcohols called sphingosines) already have a hydrophobic chain, so only one fatty acid must be attached [4, 7]. Sphingomyelines are the most common sphingolipid to participate in biological membranes and are found primarily in human liver and red blood cells at concentrations up to 19% by mass [7, 8]. The most abundant lipids in biological membranes are glycerophospholipids. Glycerophospholipids are glycerol based lipids with a phosphate (PO_4) group in the headgroup and make up more than 40% of the total lipid mass in mamalian cellular and intra-cellular membranes [2]. Glycerophospholipids, often grouped with sphyngomyelin, are referred to as *phospholipids*. Phospholipids are two-chain lipids with the phosphate group attached directly to the backbone. A typical phospholipid is shown in Figure 1.2a. With the exception of sphyngomyelin, we define four primary classes of phospholipids by headgroup: phosphatidylcholine (PC), phosphatidylethanolamine (PE) phosphatidylserine (PS) and sphyngomyelin (SM). The electrical properties of the headgroup, number of carbons and double bonds in each acyl tail and structural differences between tails allow further classification. Phosphatidylserines carry one negative charge, where phosphatidylcholines, phosphatidylethanolamines and sphingomyelines contain counteracting charges (zwitterions). Chain length is calculated as the number of carbons from the backbone to the end of the tail as shown in Figure 1.2a. Common lipid tail

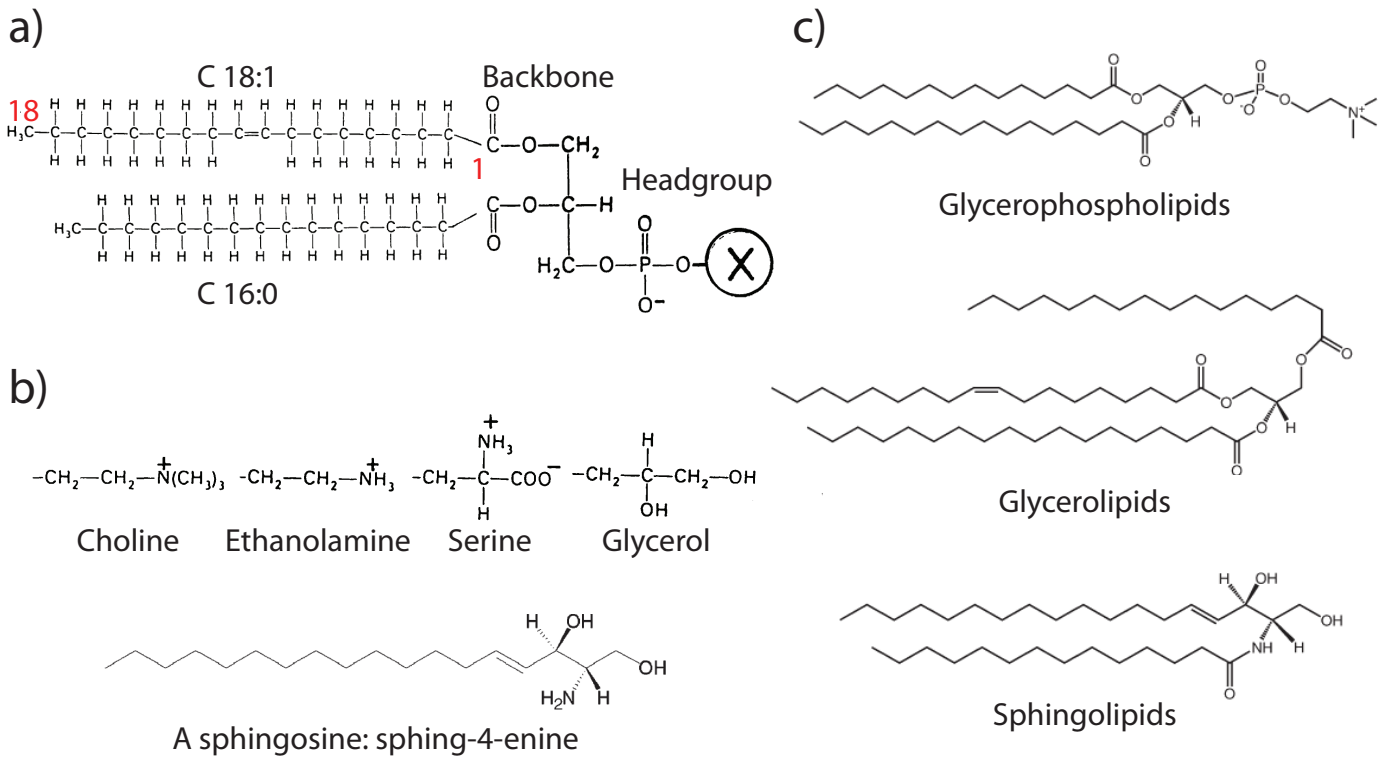

Figure 1.2: Common lipid structures. A generalized phospholipid is shown in a) [2]. The headgroup, backbone and tail region are shown. Tail length is counted from the backbone to the end of the tail, and is denoted by m:n, where m is the length and n is the number of chain double bonds. Common backbone and headgroup molecules are shown in b). An example of glycerolipids, sphingolipids and glycerophospholipids are shown in c) [6].

lengths range from 12-24 carbons and 0-6 double bonds. Lipids with no tail double bonds are called *saturated*. Carbon double bonds in lipid tails cause kinks in the tail structure, spreading the lipids apart and creating disorder. The notation m:n shown in Figure 1.2a denotes the chain length (m) and number of double bonds (n). Phosphatidylcholines tend to be short-chain lipids (14-18) with unsaturated tails appearing only in the longer chains. Phosphatidylethanolamines and Phosphatidylserines tend to be longer-chain (18-22 carbons) lipids ∼40% of which have tails with more than one carbon double bond (polyunsaturated tails). Sphingomyelines contain 50% 24 length chains with one, or no unsaturated bonds [2]. Common experimental phospholipids include 1,2-dimyristoyl-sn-glycero-3-phosphatidylcholine (DMPC), 1,2-dipalmitoyl-sn-glycero-3-phosphatidylcholine (DPPC), 1,2-distearoyl-sn-glycero-3-phosphatidylcholine (DSPC), 1,2-dioleoyl-sn-glycero-3-phosphoethanolamine (DOPE), 1,2-dimyristoyl-sn-glycero-3-phospho-L-serine (DMPS) and 1,2-dioleoyl-sn-glycero-3-phospho-L-serine (DOPS). Properties of these lipids are shown in Table 1.1. The 14 carbon saturated lipid DMPC was used for our experiments. DMPC structure is shown in Figure 1.3 and its properties are enumerated in Table 1.2. In general lipids are treated as amphiphilic molecules with a rigid hydrophobic headgroup and floppy hydrophobic tails as shown in figure 1.4.

Properties of common experimental lipids				
Abbrev.	Formula	Chain Length	Molecular Weight	Gel-Fluid Transition
DPPC	$C_{40}H_{80}NO_8P$	16:0	734.039 g/mol	314 K
DSPC	$C_{44}H_{88}NO_8P$	18:0	790.039 g/mol	328 K
DOPE	$C_{41}H_{78}NO_8P$	18:1	744.034 g/mol	283 K
DMPS	$C_{35}H_{65}NO_{10}PNa$	14:0	701.844 g/mol	308 K
DOPS	$C_{42}H_{77}NO_{10}PNa$	18:1	810.025 g/mol	262 K

Table 1.1: Properties of phospholipids commonly used in experiment. Chain lengths are indicated in m:n format, where m is the number of carbons in the tail and n is the number of tail double bonds. Gel-fluid transition temperatures shown are for bilayers containing only these lipids [9].

Lipid aggregates self-assemble into a variety of structures. This structure is influenced by the shape of the lipids, the level of hydration, defined by the number of water molecules per lipid head group, and the temperature [2]. Lipid monolayers assemble due to their amphiphilic nature and assume a natural curvature based on the

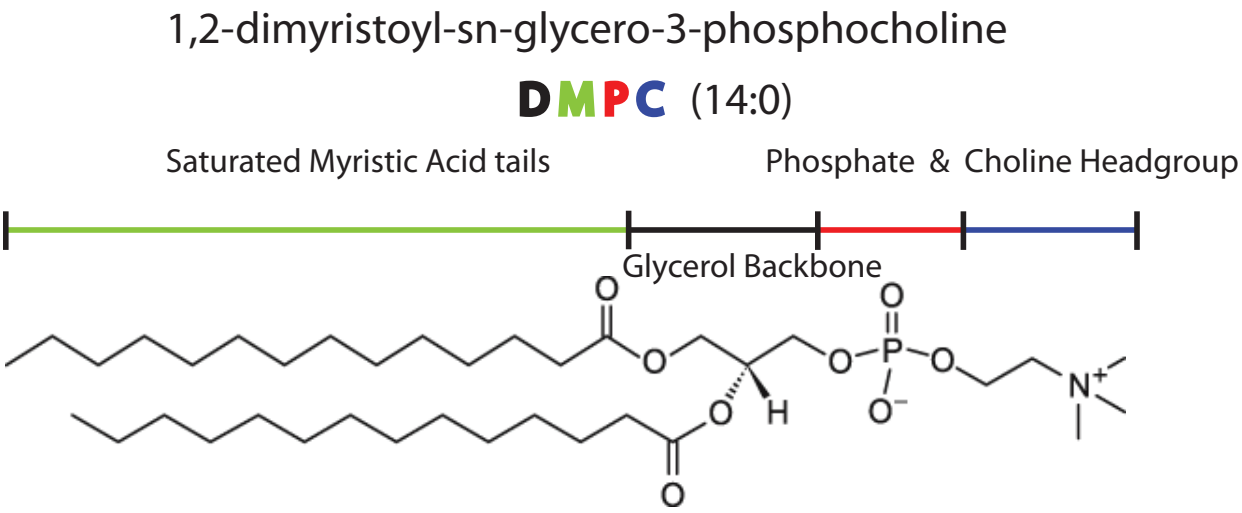

Figure 1.3: Chemical structure of 1,2-dimyristoyl-sn-glycero-3-phosphatidylcholine (DMPC).

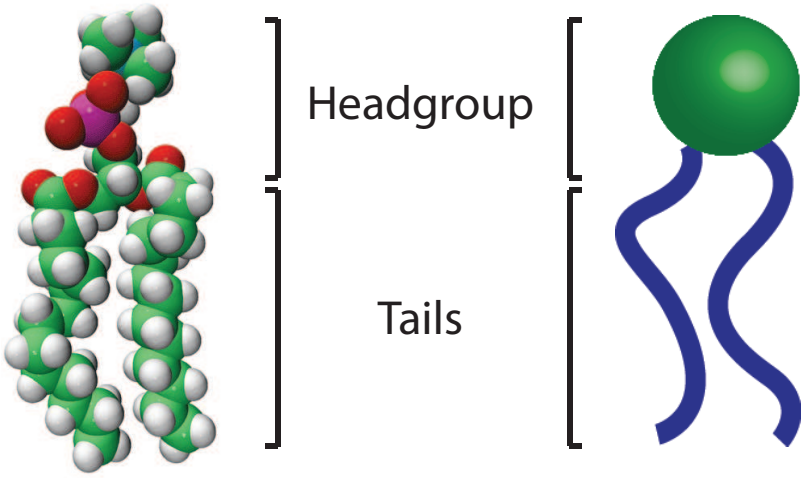

Figure 1.4: The chemical structure of a lipid (DMPC) is shown on the left. We model these lipids as a large rigid hydrophobic headgroup (green) with two floppy hydrophobic tails (blue).

Properties DMPC	
Chemical Formula	$C_{36}H_{72}NO_8P$
Chain Length	2×14
Saturation	Saturated
Charge	Zwitterionic
Molecular Weight	677.933 g/mol
Chain Size	12.7 Å
Bilayer Thickness*	62.6 Å
Tail-Tail Spacing*	4.50 Å
Area per Lipid*	60.6 $Å^2$
Gel-Fluid ($L_{\beta'} \rightarrow L_\alpha$) Transition	296 K
Gel-Ripple ($L_{\beta'} \rightarrow P_{\beta'}$) Transiton	287 K

Table 1.2: Properties of 1,2-dimyristoyl-sn-glycero-3-phosphocholine (DMPC). Transition temperatures are for multilamellar DMPC bilayers. (*) Area per lipid, bilayer spacing, headgroup spacing and chain size are calculated for fluid (L_α) phase fully hydrated DMPC bilayers at 303 K [10]. Lipid tail spacing is also for fully hydrated fluid bilayers at 303 K [11].

lipid geometry. The natural curvature of a monolayer is determined by the *packing parameter* $p = \frac{V}{A \cdot L}$, where V is the volume of the entire lipid molecule, L is its length and A is the headgroup area at the lipid-water interface as shown in Figure 1.5b [12]. The denominator $A \cdot L$ describes a static cylindrical shape. The numerator V is dependent on the lipid shape. A conical shape indicates the lipid tails and headgroups occupy different areas. If the lipid tails require more area than the headgroups, $p > 1$ and lipids form the hexagonal $H_{||}$ phase shown in Figure 1.5c. Conversely, if the lipid headgroups require more area than the tails, $p < 1$ and micelles form (Figure 1.5a). Flat lamellar phases (L_α, $L_{\beta'}$ and $P_{\beta'}$) form when lipid tails occupy the same in-plane area as the headgroups ($p = 1$). A spherical bilayer, or *vesicle*, forms when a balance is struck between the bilayer bending energy and the hydrophobic interfacial energy. Phosphatidylethanolamines and diacylglycerol have small hydrophilic areas, and so prefer hexagonal phases. Phosphatidylcholines and sphingomyelines are generally cylindrical and form bilayers [13]. The packing parameter also depends on temperature and water content. Temperature increases enhance disorder in the lipid tails, creating larger tail volumes. Increased hydration amplifies lateral repulsions between polar headgroups, creating more water-headgroup area [2].

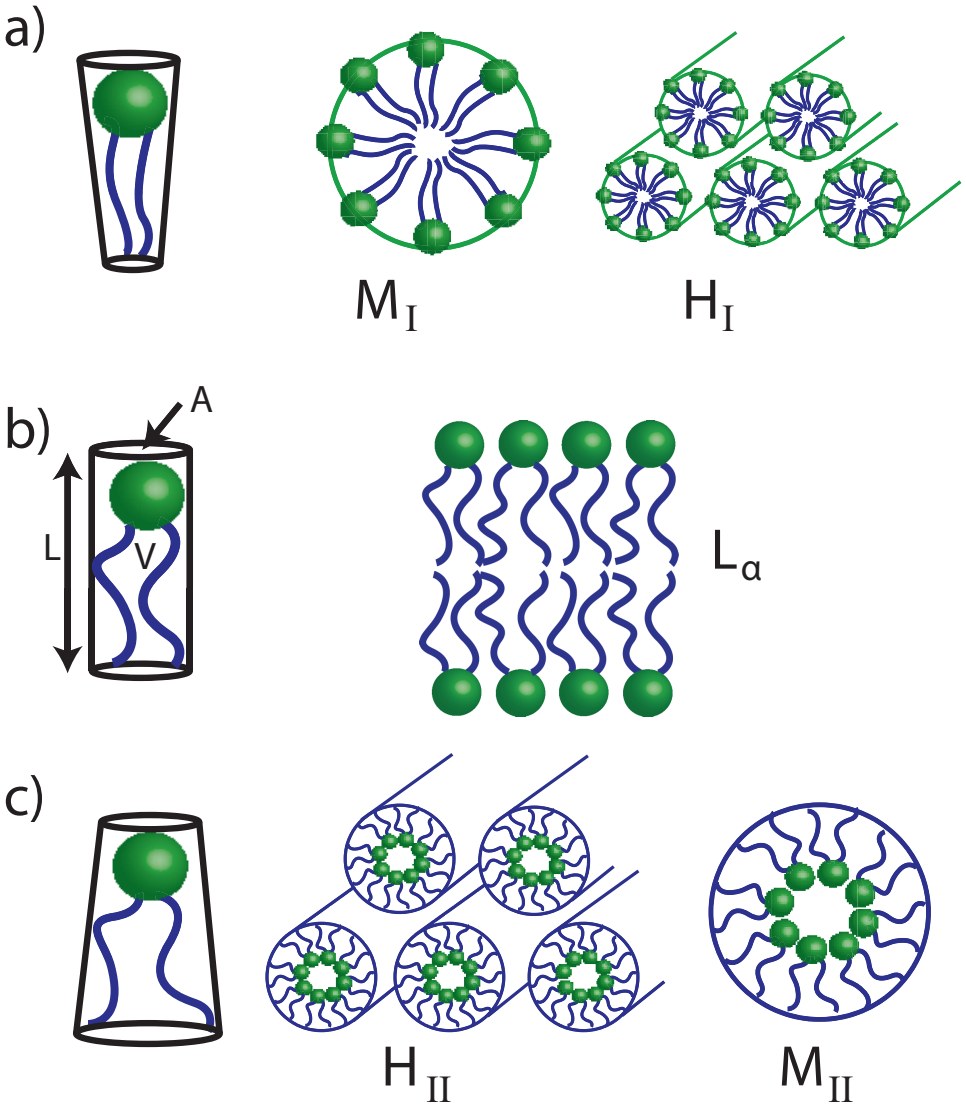

Figure 1.5: Basic lipid morphologies. a) depicts the micelle (M_I) and hexagonal micelle rod phases (H_I) which occur when $p < 1$. b) depicts the familiar fluid bilayer (L_α) phase. c) depicts inverse micelle phases M_{II} an H_{II}.

1.2 Lipid Bilayers

Fluid phase (L_α) lipid bilayers compose the backbone of biological membranes [3]. However bilayers exist in a variety of phases. Figure 1.7a shows the three primary lamellar phases: L_α (fluid) , $L_{\beta'}$ (gel) and $P_{\beta'}$ (ripple) [14]. Relative humidity is measured as $100\times$ P/P_0, where P is the partial water vapour pressure near bilayer and P_0 is the vapour pressure over pure water and is analagous to water content[15]. The $L_{\beta'}$ phase is known as the gel phase and is characterized by 2D ordered and tilted lipid tails [16]. Lipid tails in this phase exhibit hexagonal packing, however the headgroups remain disordered, providing no overall lipid molecular order [3, 17]. The three subphases L_{β_F}, L_{β_L} and L_{β_I} shown in Figure 1.7b represent different tail tilt angles. The angle ϕ between the hexagonal lattice position and the direction of tilt ranges between 0^o for L_{β_F} to 30^o for L_{β_I}[15]. The $P_{\beta'}$ is characterized by ripples as shown in Figure 1.8b. Ripples form by freezing undulation dynamics out of the fluid (L_α) phase or due to packing defects in the tilted $L_{\beta'}$ phase [18, 19]. In multilamellar DMPC, ripples exhibit a periodicity of $\sim$100 Å which increases when approaching the transition to L_α [20]. The L_α, or fully hydrated fluid phase exhibits lipid tails in the 'melt' state which demonstrate no long range order [3]. A low temperature subgel phase ($L_{c'}$) has also been observed, which demonstrates increased tail tilt angles and headgroup ordering [21].

The lipid bilayer is composed of two lipid monolayers (leaflets). Hydrophobic tails in each leaflet come together to form the centre of the bilayer, while hydrophilic headgroups line the exterior. Lipid bilayer structure therefore consists of two domains: a hydrophilic headgroup region and a hydrophobic core (Figure 1.6). Orientation is defined in terms of the bilayer surface normal as either perpendicular to (z-direction) or in the plane of the bilayer. The structure of fluid phase (L_α) bilayers has been well characterized by X-ray scattering techniques [10, 22]. Structural parameters for common lipids are shown in Figure 1.9 and Table 1.3 [10, 22]. In general, the hydrophobic core is $\sim$40 Å thick (D_C), each headgroup is $\sim$9 Å thick, and multilamellar repeat distances (d_z) are $\sim$60 Å. For DMPC the fluid phase bilayer thickness is 62.6 Å, the in-plane lipid nearest neighbour distance is $\sim$6 Å and the in-plane tail spacing is 4.50 Å [11]. The number of interlamellar water molecules per lipid required for fully hydrated DMPC is calculated to be 26 by observing the point where additional

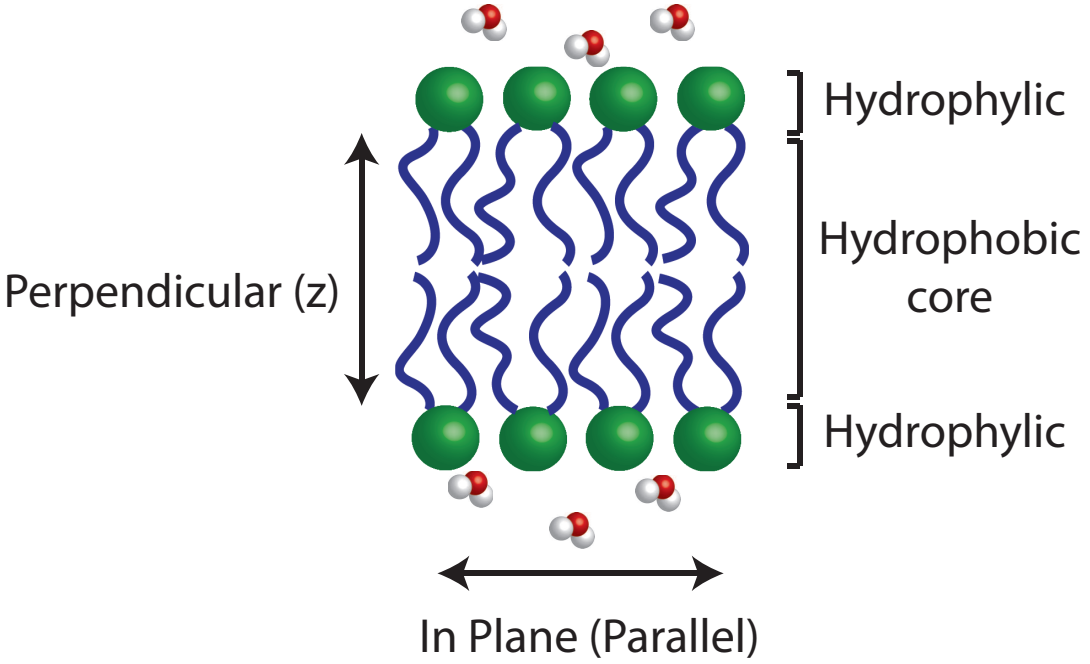

Figure 1.6: A model lipid bilayer demonstrating how the headgroups point outwards allowing the formation of a hydrophobic membrane core. Orientations are indicated as either parallel (in-plane) or perpendicular to the plane of the bilayer.

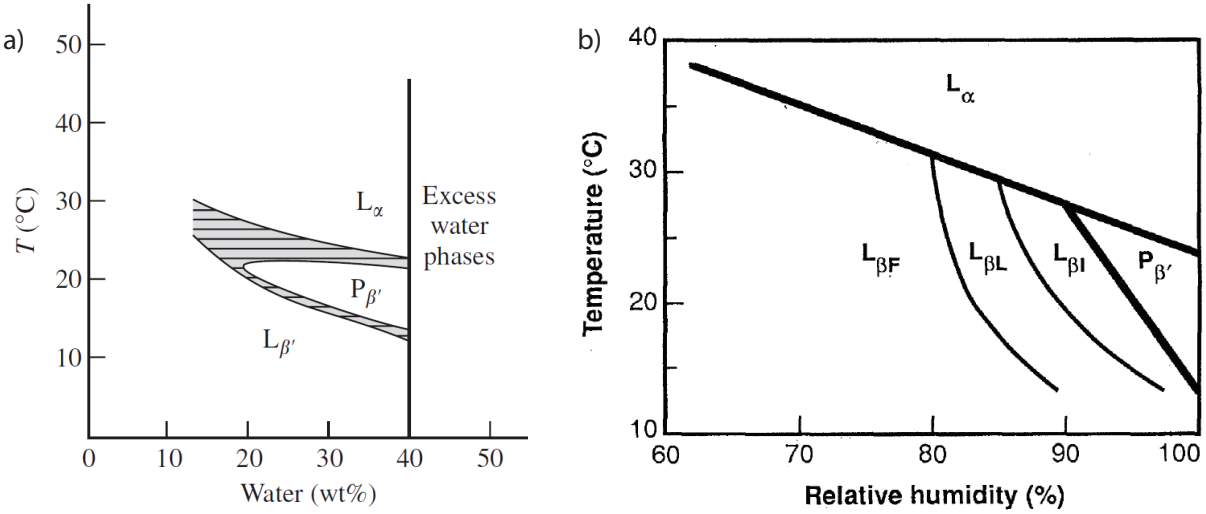

Figure 1.7: a) DMPC lamellar phases as a function of water content and temperature [14]. Hash marks indicate transition regions. b) DMPC lamellar phases in more detail as a function of relative humidity. The three subphases of $L_{\beta'}$ shown differ only in tail tilt angle.

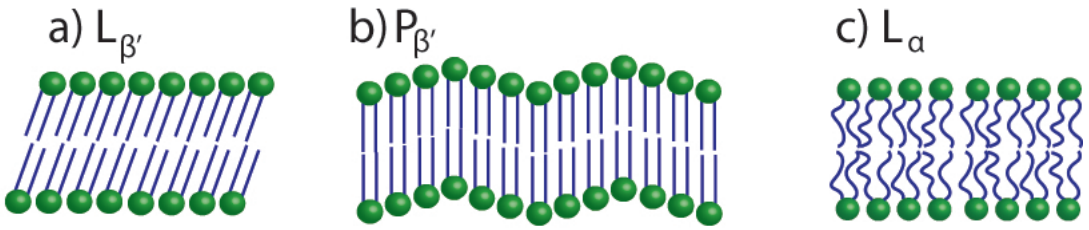

Figure 1.8: Bilayer structures for lamellar phases: $L_{\beta'}$ (gel), $P_{\beta'}$ (ripple) and L_{α} (fluid).

water does not increase the bilayer thickness (d_z), indicating an excess water phase [10, 23].

Structural dimensions of lipid bilayers							
Lipid	Temperature (K)	A_L (Å^2)	d_z (Å)	D_B (Å)	D_C (Å)	D_{HH} (Å)	D_W (Å)
DPPC	323	64	67	28.5	28.5	38.3	28.5
DMPC	303	60.6	62.6	36.3	25.4	35.3	36.9*
DOPC	303	72.5	63.1	35.9	27.1	36.9	27.2
DLPE	308	51.2	45.8	35.4	25.8	35.6	10.4

Table 1.3: Structural dimensions of lipid bilayers in the L_{α} phase. Parameters were calculated from analysis of x-ray scattering length density curves [10, 22]. D_W values reported are calculated by subtracting D_B from d_z according to [24]. DMPC parameters were taken from [10] with the exception of the water thickness (D_W) which was taken from [22] for consistency. Note that DLPE is a short chain saturated lipid (12:0).

Fluid phase lipid bilayers are very dynamic. We classify lipid dynamics as single-lipid motions or collective motions. Single lipid dynamics may include rotations, vibrations or diffusions, where collective motions may consist of long-range undulations or coherent fluctuations [2]. Collective lipid bilayer dynamics are driven by thermal motions, and cover lengthscales from μm to Å [25]. Collective lipid fluctuations may also influence membrane properties such as permeability or elasticity [25, 26]. Coherent collective fluctuations create waves in the bilayer which can be characterized as phonons. We describe how the energy of these phonons changes with a reciprocal lengthscale ($\boldsymbol{q}$) in a dispersion curve. An example dispersion curve for collective lipid tail fluctuations is shown in figure 1.10a. This exhibits a linear

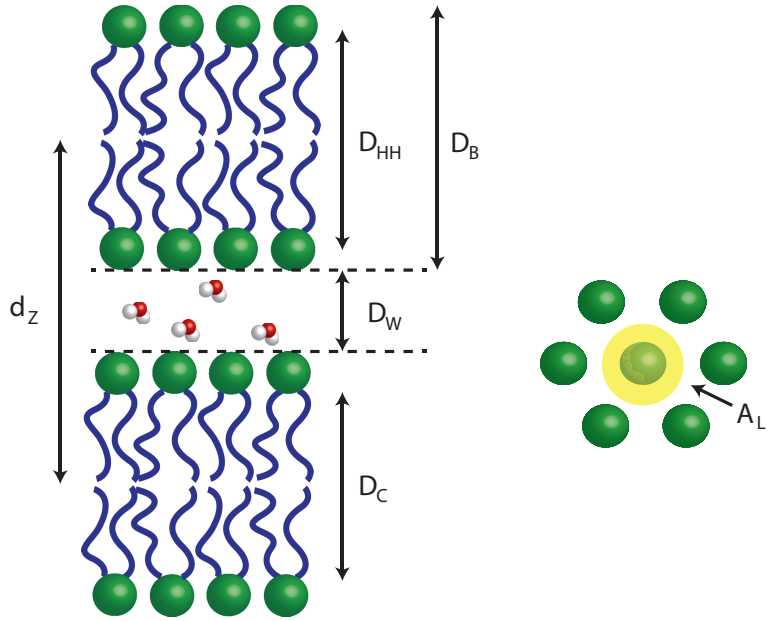

Figure 1.9: Lipid bilayer structural parameters.

region at very small $\boldsymbol{q}_{||}$ corresponding to long wavelength excitations such as sound waves and a minima at the tail-tail spacing. This demonstrates that the lipid tails preferentially fluctuate at this characteristic energy. Chen *et al.* first demonstrated that DLPC lipid tail fluctuations exist with energies ∼1 meV and wavelengths of ∼4 Å [27]. In-plane lipid tail fluctuations in DMPC occur with energies ∼2 meV (Figure 1.10b) [11, 28], fluid phase relaxation times of 9.2 ps and correlation lengths of 20 Å [11]. Surface relaxation modes in multilamellar supported bilayers were observed with relaxation times ∼100 ns [18]. These modes occur over a variety of wavelengths due to motion of the interlamellar water [29]. Analytical undulation eigenmodes for supported bilayers are shown in Figure 1.11 [30]. Corresponding undulation modes with relaxation times of ∼10 ns are observed in Neutron Spin-Echo experiments [18].

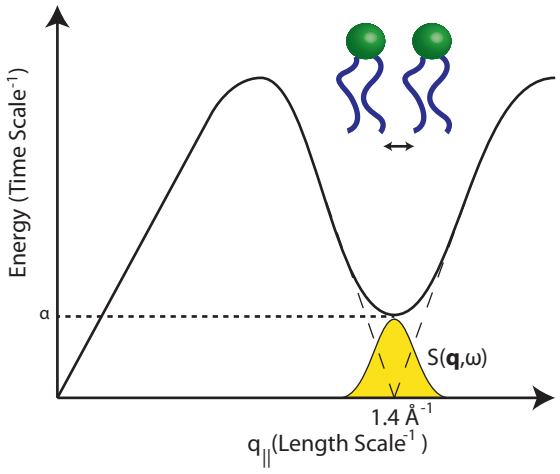

Figure 1.10: a) A schematic of the dispersion curve for lipid tail dynamics. The phonon exhibits a linear region at large lengthscales, corresponding to sound waves, and a trough at the nearest neighbour distance (in this case, that of the lipid tails). This shape is typical of acoustic phonons.

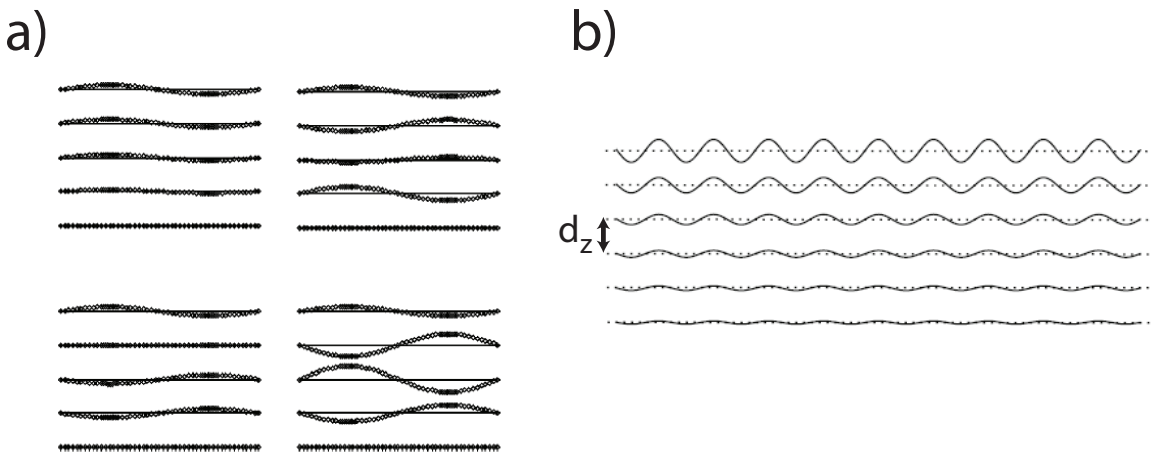

Figure 1.11: a) Theoretical undulation eigenmodes in multilamellar lipid bilayers [30]. b) Relaxing surface mode in solid supported multilamellar bilayers [29].

Chapter 2

Macromolecules and Membrane Properties

While lipid bilayers compose the backbone of the biological membrane, many other macromolecules participate. The presence of macromolecules in the membrane are known to influence its properties [31]. It is well known that proteins play a role in a variety of membrane properties [32], however smaller macromolecules such as cholesterol and short chain alcohols also influence properties such as elasticity and permeability [33, 34]. Small changes in bilayer composition can also alter the function of intrinsic proteins such as ion or water channels [33]. While molecules such as cholesterol may be incorporated into the bilayer during the preparation process, the content of short length alcohols can only be controlled in-situ by placing bilayers in an excess water-alcohol solution or the condensation of water-alcohol solutions from a surrounding vapour. Ethanol addition from the aqueous phase poses particular challenges such as enhanced background scattering, absorption and in particular thermal unbinding, which make examining more complex bilayers difficult.

2.1 Macromolecular impact

Two common macromolecules which are known to influence bilayer properties are cholesterol and short chain aclohols, such as ethanol.

2.1.1 Cholesterol

Cholesterol is a vital component in eukaryotic cells [35]. Concentrations of 20 - 50% cholesterol are observed in healthy plasma membrane tissues [36]. A cholesterol molecule is shown in Figure 2.1a. Cholesterol is composed of a hydrophilic hydroxyl group and a large hydrophobic region consisting of rigid sterol rings and a fatty acid. As a result, cholesterol participates primarily in the hydrophobic membrane core. In the presence of saturated lipids, cholesterol aligns itself with the hydroxyl head near the lipid headgroups and hydrophobic region in the centre of the bilayer ('upright' orientation) [37]. However in the presence of polyunsaturated fatty acids (PUFA), cholesterol is sequestered horizontally in the bilayer core [38]. In these orientations, cholesterol is primarily confined to the hydrophobic membrane core. Figure 2.2 shows a theoretical phase diagram of a DMPC-cholesterol system calculated by coarse grain molecular dynamics simulation [39]. A new liquid ordered phase (L_o) is observed at high temperatures and cholesterol content. The formation of cholesterol clusters in the subgel phase ($L_{C'}$) is also observed at high cholesterol content. In the gel phase, cholesterol is known to increase the area per molecule, while in the fluid phase, it decreases the area per molecule and restricts the passive transport of small molecules through the bilayer [35]. The observed decrease in permeability in the fluid phase is due to a reduction in the bilayer free volume in the region surrounding the cholesterol sterol rings [34]. The reduction in free volume has also been related to reduced in-plane diffusion observed in DPPC-cholesterol systems [36].

Cholesterol is primarily known for its effect on membrane stiffness. In its upright orientation, cholesterol increases the order of the lipid hydrocarbon chains, straightening them along the bilayer normal and increasing bilayer thickness [32, 40]. Lipid tail straightening causes increases in the bending (K_C) and compression moduli (K_A) which describe the elasticity of the bilayer [40, 41]. Chen *et. al* reported a 30% increase in the bending modulus of DOPC monolayers with the addition of 30% cholesterol [37]. Micropipet vesicle compression has also demonstrated a 3-4 fold increase in the compression modulus in SOPC bilayers with the addition of 50% cholesterol. Bending and compression moduli for pure DMPC bilayers at 303 K were reported as $K_C = 6.1 \times 10^{-20}$ J and $K_A = 2 \times 10^{15}$ J/m^3 [18]. In general bilayer bending moduli are on the order of $10k_BT$ [8]. Vesicle fluctuation and pipet pressurization

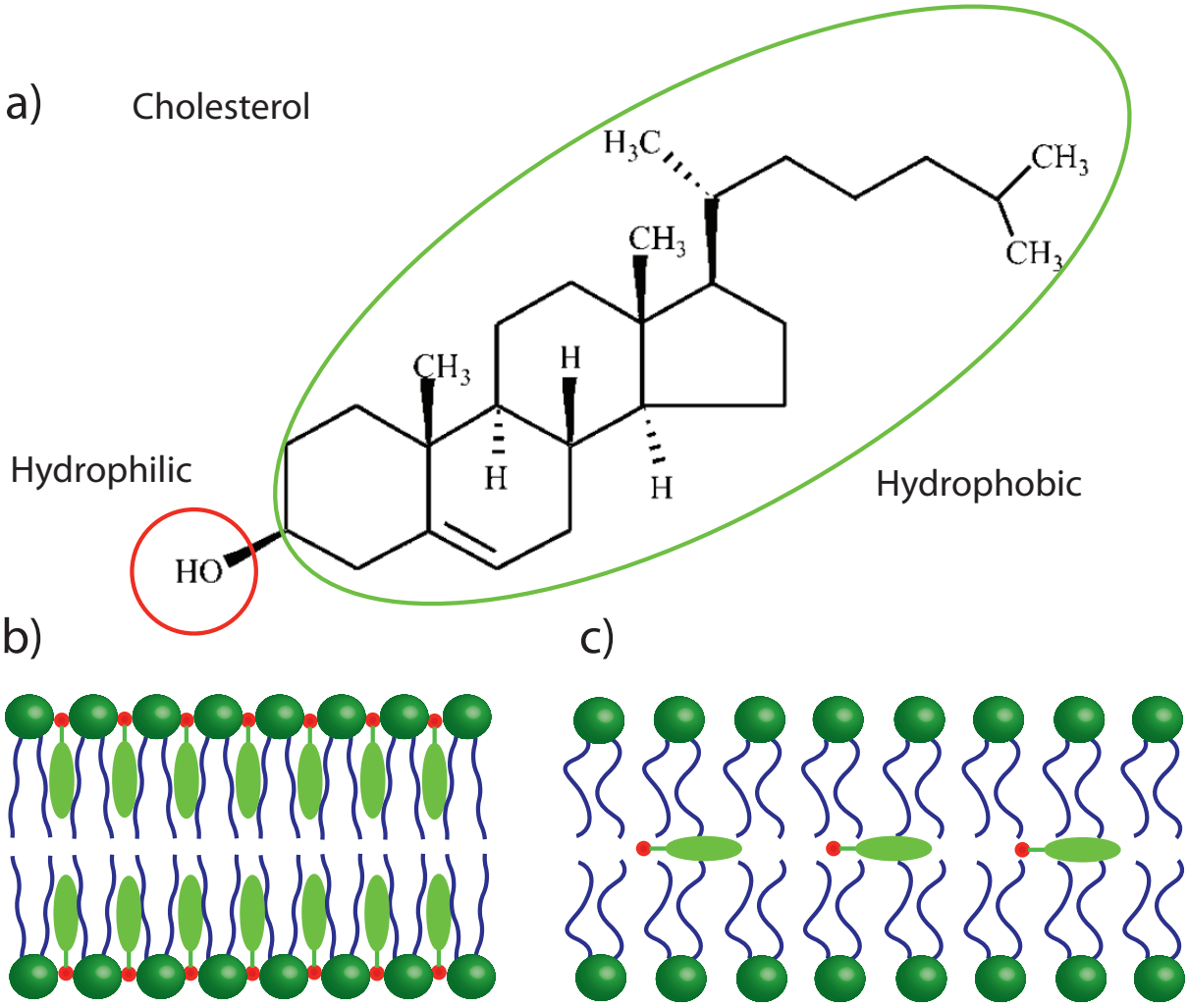

Figure 2.1: Chemical structure and orientation of cholesterol in the bilayer. a) depicts the small hydrophilic and large hydrophobic regions. b) and c) demonstrate the upright and flat cholesterol orientations. The orientation in b) is adopted in the presence of a critical concentration of unsaturated lipid tails [38].

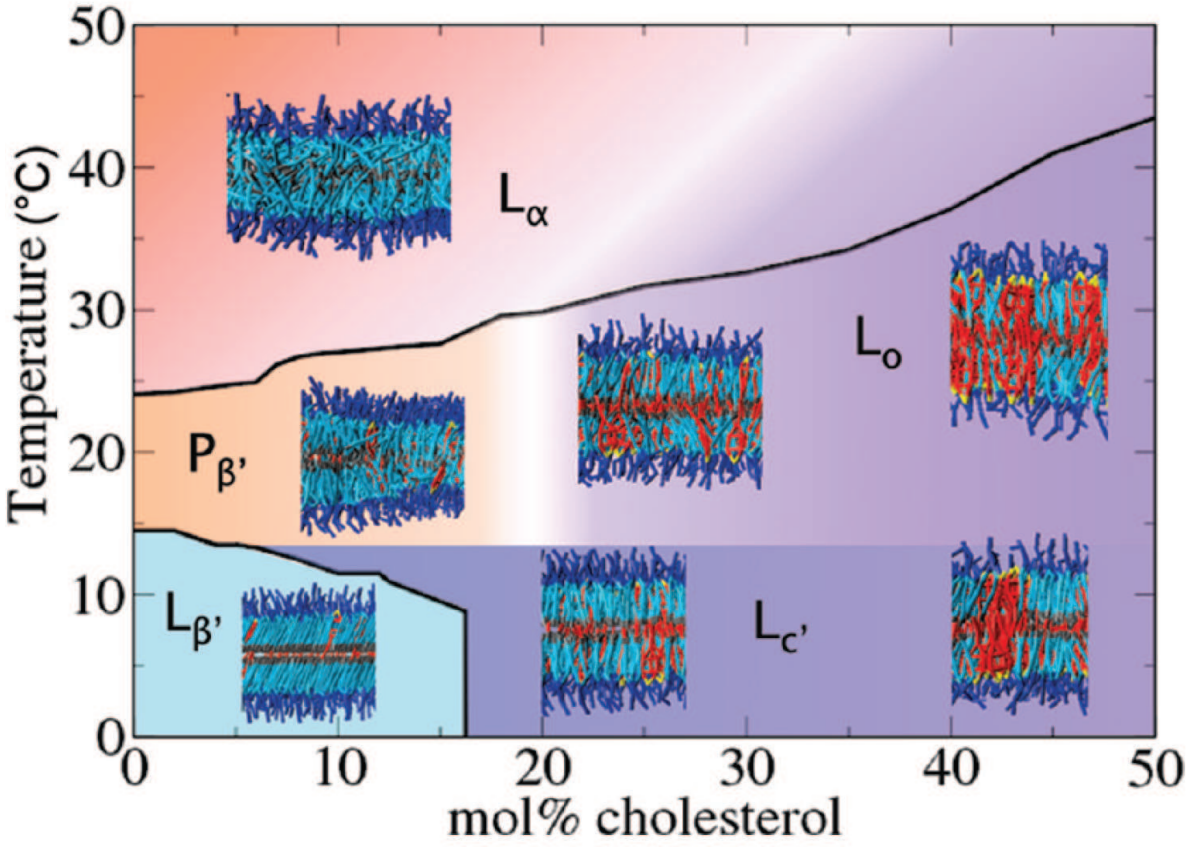

Figure 2.2: Phase diagram of DMPC-Cholesterol bilayers with temperature determined by molecular dynamics simulations. Lipid tails are depicted in light blue, headgroups in dark blue, cholesterol hydrophilic group in yellow and hydrophobic region in red. Background colours represent the different phases and the broadness of the phase transitions. The three primary lamellar phases are shown as well as the subgel (L_C) and a new cholesterol-ordered phase (L_o) [39].

experiments of DMPC demonstrate 2-5 fold increase in K_C and 2.5 fold increase in K_A at 30% molar cholesterol [39]. Cholesterol is also speculated to be involved in the formation of cholesterol rich domains in the bilayer known as lipid rafts, which are believed to act as microenvironments for integral proteins and other large molecules [40].

2.1.2 Ethanol

Ethanol is a short-chain alcohol with a hydroxyl group and two-carbon hydrophobic hydrocarbon chain. Ethanol preferably Hydrogen bonds to hydrophilic phosphates in the headgroups of phospholipid bilayers. The carbon chain is slightly hydrophobic, which allows ethanol to also pass through the membrane core with timescales of ∼200 ns [33]. However, the free energy of ethanol increases exponentially as it approaches the membrane core so it is 1000 times more likely to find ethanol at the lipid-water interface [42]. The free energy of ethanol in the vicinity of the phosphate group is equivalent to its free energy in water [42]. Ethanol penetrates deeper into the bilayer than water and aggregates near the depth of the glycerol group [33, 42]. Ethanol Hydrogen bonds with the ester oxygens in the phosphate or carbonyl (double bonded C-O) groups with its hydrocarbon chain intercalated among the lipid tails [43]. Figure 2.3a shows x-ray scattering length density profiles for water, ethanol and the lipid phosphate and carbonyl group, which indicate relative concentrations at a particular bilayer depth z. The ethanol concentration maximum occurs 17.5 Å from the bilayer core, which lies between the phosphate and carbonyl groups. Figure 2.3b demonstrates two possible ethanol-lipid bonding configuratons. Only 1 in 7 ethanol molecules is not bound in this fashion. Bonding lifetimes are on the order of 1 ns, which is much longer than the picosecond dynamics exhibited by lipid tails. Bonding times at the hydrophobic-hydrophilic interface are also found to be longer than those nearer the water layer. Unlike cholesterol, ethanol prefers the aqueous phase so it is not permanently bound to the bilayer. Ethanol is known to influence membrane properties. The presence of ethanol alters lipid headgroup ordering. This effect is indicated by increases in the area per lipid (A_L) by ∼6% for one and ∼18% for two ethanol molecules per lipid [43]. The increase in area per lipid also results in an increase in lipid tail disorder [33, 42, 43]. However the

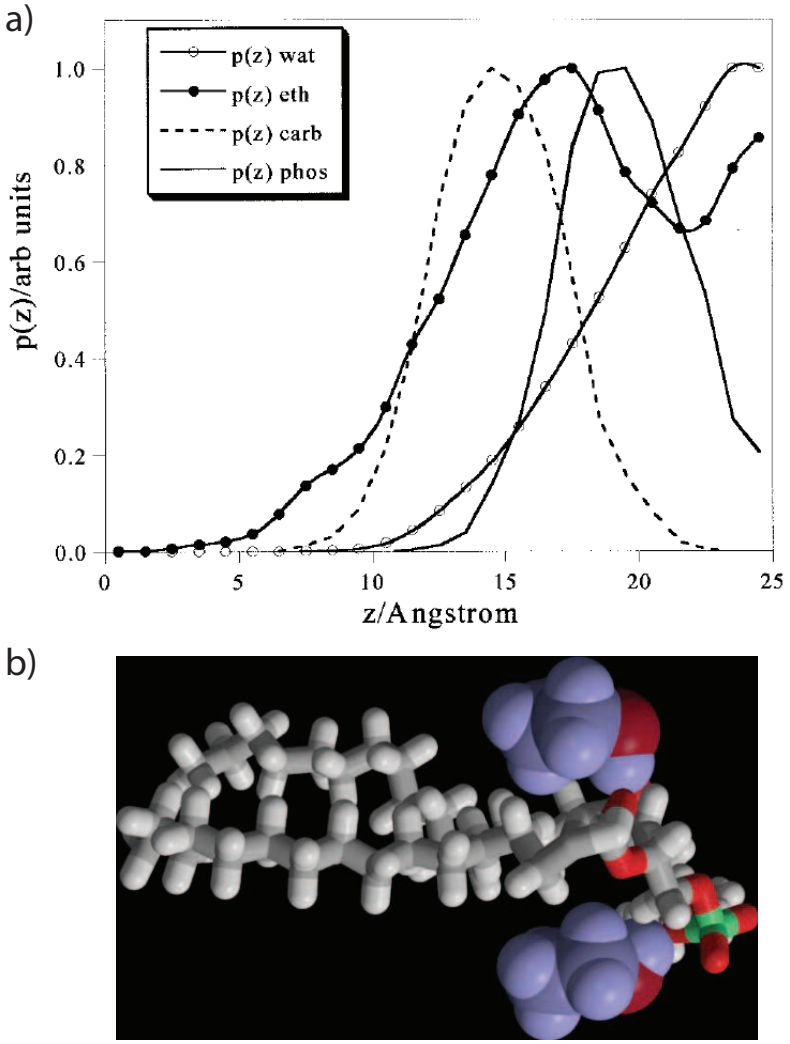

Figure 2.3: a) Density profiles for ethanol and intra-lipid chemical groups as a function of distance from the bilayer core. Perpendicular (z) distance is shown on the x-axis, where x = 0 represents the bilayer centre. Note how ethanol resides between the phosphate and carbonyl groups [42]. b) A schematic of the position of ethanol relative to a lipid (DPPC). Ethanol is shown in blue.

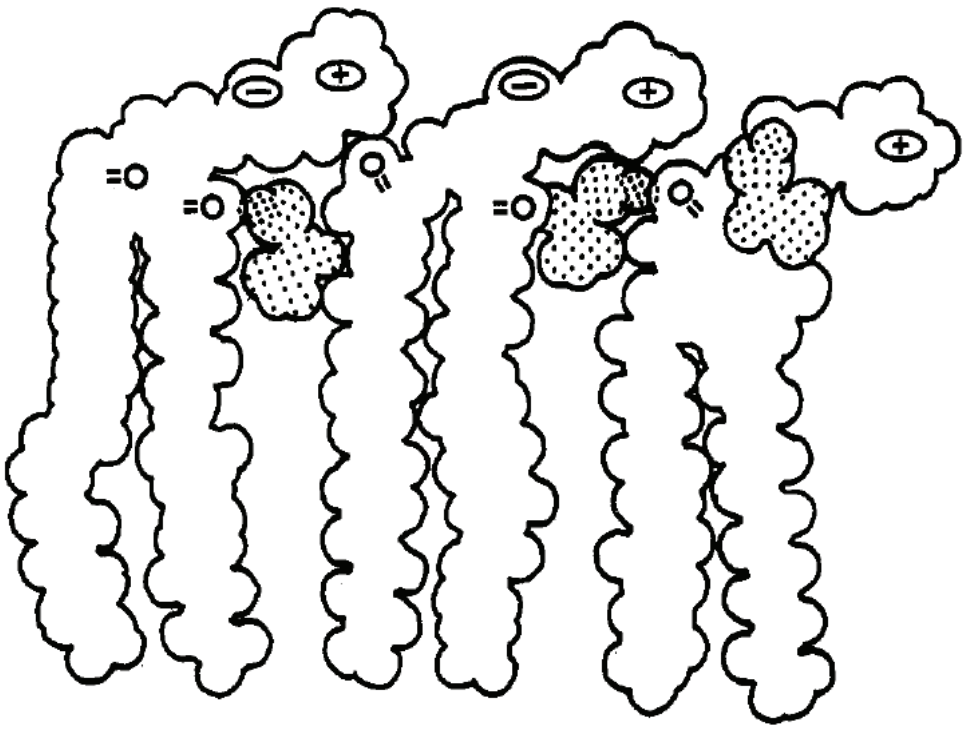

Figure 2.4: Lipid orientation when bound to ethanol. The outline of three lipids are shown with the position of ethanol grayed out.

molecular packing near the glycerol group of ethanol-bound lipids is tightest [43]. An increase in bilayer fluidity and disorder is also observed, particularly in lipids not bound to ethanol [33]. The lipid phosphate and choline groups, as well as the lipid centre of mass for ethanol-bound lipids were found to be shifted 2 Å closer to the bilayer core, which is indicative of ethanol-bound headgroup ordering shown in Figure 2.4. Ethanol is also known to increase the fluid lamellar to inverse-hexagonal ($L_\alpha \rightarrow H_{||}$) phase transition temperature [43] and to decrease the gel to fluid ($L_{\beta'} \rightarrow L_\alpha$) phase transition temperature [44]. The surface tension of the bilayer is also reduced in the presence of ethanol [44]. Ethanol is known primarily for enhancing bilayer permeability, however the mechanism behind this effect is unknown [33, 44, 45]. Active transport of ions or molecules through the membrane is often performed by integral proteins such as water or ion channels. Passive trans-membrane transport of small molecules such as water is traditionally described by the solubility diffusion model [26]. The solubility diffusion model treats the membrane as a thin hydrophobic

barrier in an aqueous environment. Particles crossing the membrane must dissolve in the hydrophobic region, diffuse across it, and redissolve in the opposite aqueous environment [26]. Permeability coefficients are described by the solubility diffusion model as $P = \frac{D_m K}{D_C}$, where K is the rate at which particles are incorporated into the bilayer (the partition constant), D_m is the diffusion constant of the permeant in the bilayer core and D_C is the core thickness [46]. However this model does not account for permeant size, and significant deviations from predicted permeability coefficients have been observed [46]. Increasing evidence suggests that bilayer thermal fluctuations may also contribute to passive permeability [26, 47, 48]. Partitioning in the bilayer may be achieved by the formation of transient pore defects in the bilayer [26]. Träuble also proposed that lipid tail fluctuations may play a role in diffusion throught the bilayer core. Thermal motion of lipid tails results in the formation of kinks in the tail structure which create small transient voids. The diffusion of these voids through the hydrophobic bilayer core may lead to transport [47]. Figure 2.5a and b depict transient pore formation by density fluctuations and lipid tail voids respectively. Fluctuating pores are thought to be the dominant mechanism for passive transport of ions through thin membranes, however, the mechanism of passage of neutral molecules is still not well understood [26]. Ethanol permeability coefficients for SOPC bilayers have been reported as 3.8×10^{-5} cm/s and are larger than other alcohols [44]. The permeation of calcein dye through DPPC vesicles with 25% cholesterol in a 1.0 M ethanol solution was found to be 8 times faster than in pure vesicles in water [45]. The increase in area per lipid is believed to increase permeability by simplifying partitioning into the membrane core [33, 46]. Ethanol is also reported to decrease the thermal activation energy of water permeation through the bilayer headgroup region, facilitating access to the membrane core [49].

2.2 Thermal Unbinding

While cholesterol can be incorporated directly into a lipid bilayer, the effects of ethanol on lipid bilayers may only be observed in situ. As a result ethanol must be added to the bilayer from the liquid or vapour phase. Lipid bilayer preparation in excess solution present particular difficulties. Bilayers in solution decay over time and at high

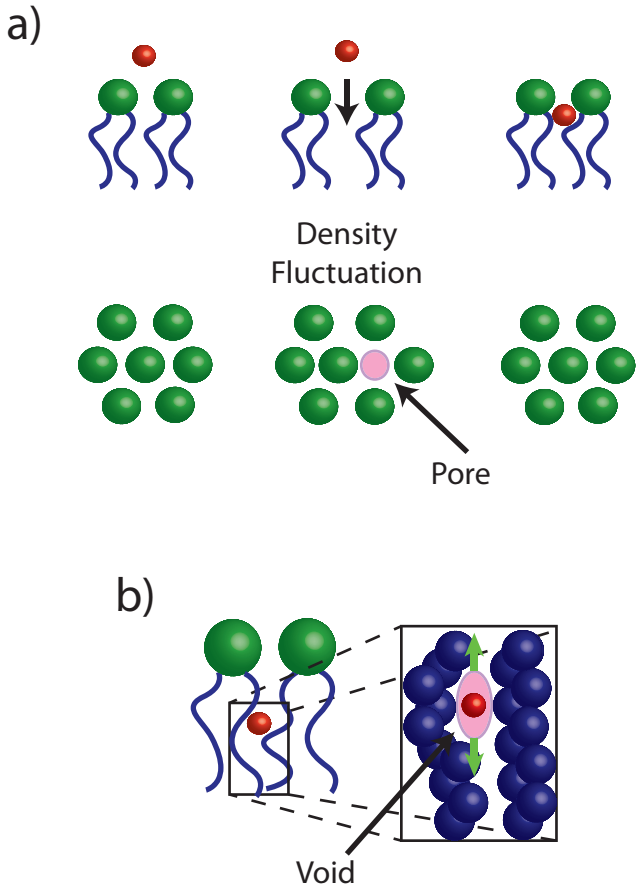

Figure 2.5: The formation of transient pore defects in the headgroup region by lateral density fluctuations is shown in a). b) depicts the transport of small molecules by means of voids in the lipid tails formed by thermal disorder.

temperatures due to thermal unbinding. Thermal unbinding describes the spontaneous decay of a solid supported multilamellar membrane stacks in excess solution to a single solid supported bilayer. This decay is characterized by a gradual decay with increasing temperature and a transition to a single bilayer at temperature T_u [50]. This transition temperature is dependent on lipid type and rate of heating, but is independent of substrate type [50]. The rate of unbinding is also inversely dependent on the number of layers N or bilayer thickness d_z in multilamellar membranes [50]. A theoretical analysis of the undulations in two-bilayer systems suggests a continuous transition from a stacked system to free membranes in solution [51, 52]. Figure 2.6 shows x-ray reflectivity curves for multilamellar POPC bilayers at different temperatures [52]. The reciprocal perpendicular lengthscale q_z is shown on the horizontal axis. The repeating peak structure represents the Bragg periodicity of the stacked system, and the intensity and width of these peaks is indicative of the perpendicular order. The intensity decrease observed particularly in the rightmost peaks indicates gradual increase in disorder. The curve at $T_u = 80^o$C describes a single bilayer on the substrate and demonstrates a discontinuous transition [52]. The transition to a single-bilayer was observed at $T_u = 95^o$C in solid supported multilamellar DMPC [52]. Confocal fluorescence and polarized optical microscropy suggest the unbinding process shown in Figure 2.7. Below the transition temperature, multilamellar 'blisters' initially form on the surface of the bilayer stack (Figure 2.7a and b). These blisters grow with increasing temperature to form multilamellar vesicles which eventually detatch from the surface. Polarized optical microscopy reveals that these multilamellar vesicles remain partially tethered to the bilayer stack (Figure 2.7c) [50]. Other unbinding catalysts have been observed, such as the addition of pentanol, a 5 carbon alcohol, to excess water surrounding a multilamellar DMPC stack, which caused decay within one hour [50]. Thermal unbinding presented a challenge for the neutron ethanol experiments. To counteract this we added 2% polyethyleneglycol (PEG) to the 5% ethanol/water solution. The PEG in solution exherts an osmotic pressure on the surface of the membrane stack which inhibits unbinding [53]. Osmotic pressure is produced by the differential in the concentration of PEG between the stacked bilayers and in the excess water solution. The presence of an osmotic pressure leads to a decrease in the bilayer spacing d_z. X-ray reflectivity investigations of 12-layer DMPC

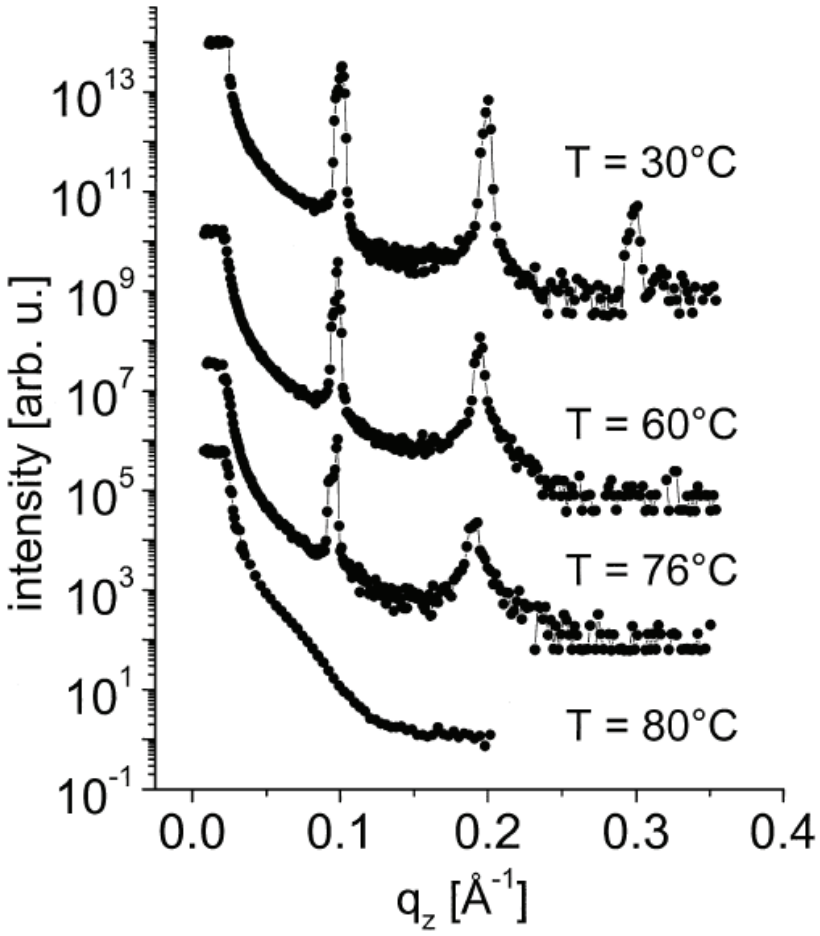

Figure 2.6: X-ray reflectivity curves for solid supported multilamellar POPC immersed in excess water at different temperatures are shown. A vertical shift has been applied for simplicity. The intensity of the three Bragg peaks decreases gradually with temperature followed by a dramatic transition at $T_u = 80^oC$. The 80^oC curve is indicative of a single bilayer remaining on the substrate [52].

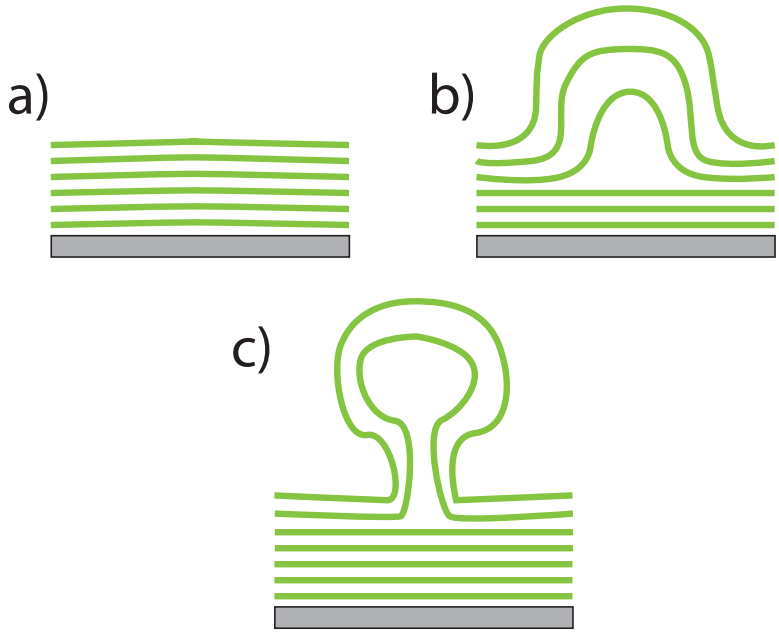

Figure 2.7: Schematic of the process of thermal unbinding as observed by optical and confocal microscopy. The multilamellar bilayer stack initially forms 'blisters' (a) and b) on the surface. These blisters grow with temperature to form multilamellar vesicles which eventually detatch from the membrane surface. Detached vesicles remain attached to the bilayer stack by a tether as shown in c) [50].

bilayers immersed in free PEG solution demonstrated a decrease in d_z of $\sim$7 Å [53]. Reflectivities of bilayers immersed in PEG and pure water solutions were measured simultaneously over a period of 8.5 h at 43^{o}C. Samples immersed in PEG retained all 12 layers for the duration of the experiment, while water-immersed samples demonstrated unbinding behaviour [53]. PEG is also known not to participate in thin films of multilamellar DMPC except to increase the time to achieve critical film thickness, which is consistent with a surrounding osmotic pressure. This effect increases with PEG concentration and molecular weight [54].

Chapter 3

Sample Preparation

Many lipid systems are employed to model lipid bilayers including vesicles, tethered vesicles, free suspended bilayers, tethered bilayers and solid supported bilayers [55]. Highly oriented solid supported bilayers provide advantages over vesicles and other model systems. Solid supported lipid bilayers are more robust than free bilayers suspended over a trough, and allow in-plane and perpendicular structure and dynamics to be distinguished. Supported bilayers also allow the application of surface-sensitive techniques such as ellipsometry, Fourier transform infrared spectroscopy and neutron and x-ray reflectivity [56].

3.1 Solid Supported Bilayers

Solid supported bilayers are commonly prepared by two methods: the Langmuir-Blodgett technique and vesicle spreading. The Langmuir-Blodgett technique involves the transfer of a lipid monolayer floated on a water layer onto the substrate, followed by dipping this same substrate onto another floated monolayer as shown in Figure 3.1a). However, the complexity of the thermodynamics and kinetics of the transfer processes involved in this technique make it challenging for phospholipids [58]. In addition, the preparation of multilamellar solid supported bilayers with this technique is difficult. Alternatively the vesicle spreading technique may result in both single and highly oriented multilamellar solid supported bilayers. Vesicle spreading (or vesicle fusion) involves suspending lipids in an aqueous solution, and spreading this

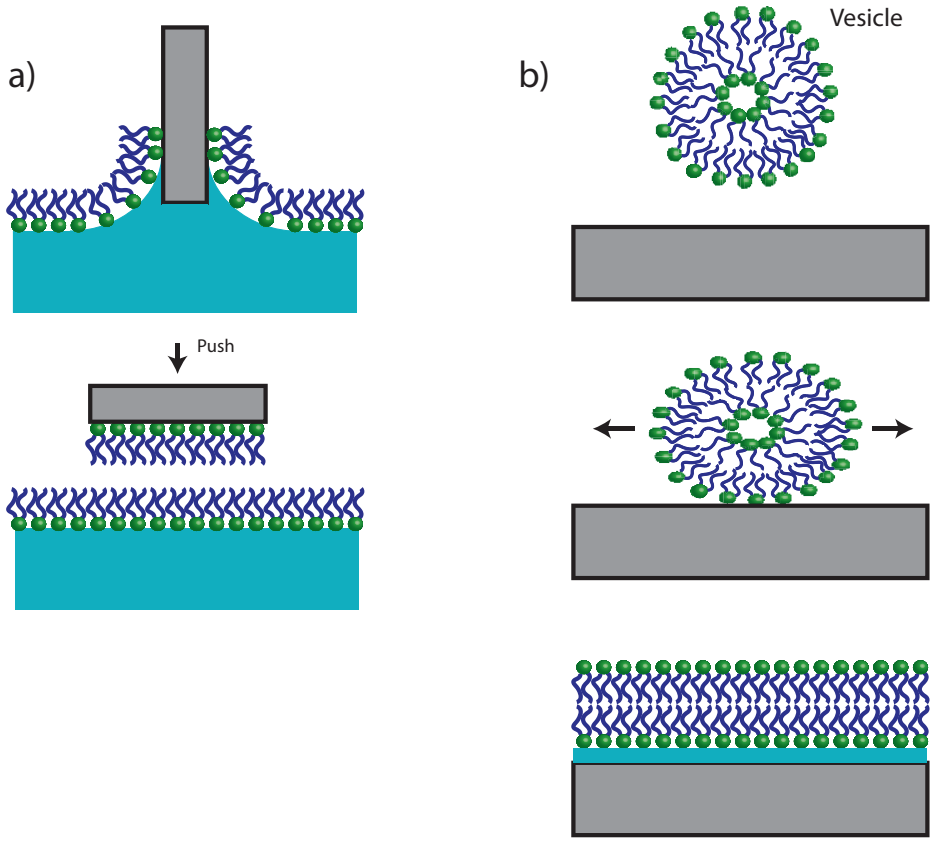

Figure 3.1: The Langmuir-Blodgett technique is shown in a). Lipid monolayers are floated on a water layer and an attractive substrate is drawn through them, adhering the bottom leaflet of a bilayer to the substrate. The top leaflet is attached by dipping the substrate in another floated monolayer. b) Demonstrates the basic vesicle spreading technique. Vesicles suspended in solution adhere to a hydrophilic substrate, spread out and eventually rupture to form a highly oriented bilayer. (For more detail see Figure 3.2 and [57]).

over an attractive substrate. The process of bilayer deposition by vesicle spreading is shown in Figure 3.2 [57]. Disolved lipids self-assemble into Giant Multilamellar Vesicles (GMVs). To obtain single bilayers, Single Unilamellar Vesicles (SUVs) must be produced either by extruding GMVs through porous membranes at high pressure, or sonicating the GMV solution [59]. The lipid solution is deposited on a hydrophilic substrate, which attracts the vesicle headgroups. The vesicles begin to elongate as more headgroups are adsorbed on the substrate, until the bilayer curvature becomes too great, and the vesicles either rupture, or fuse with other nearby vesicles. Ruptured vesicles continue to spread until uniform bilayers are formed on the substrate after 25 - 30 minutes [60].

3.2 Single Solid Supported Bilayers

Single solid supported bilayers have been demonstrated to retain the thermodynamic and structural characteristics of a free bilayer, and are an ideal model system for biological membranes. [56, 59]. The preparation of single solid supported bilayers by vesicle spreading results in bilayers separated from the substrate by 10 - 20 Å water cushions such as in Figure 3.3. The formation of this water layer depends on the smoothness of the substrate. Common substrates include borosilicate glass, mica and oxidized Silicon [59]. Silicon was selected for all experiments due to the availability of high quality polished and oriented substrates from the semiconductor industry.

3.2.1 Diffusion Experiment Sample Preparation

Single solid supported DMPC bilayers were prepared on double-side polished Silicon wafers for the neutron diffusion experiments. 100 50 mm Silicon (100) wafers obtained from Montoco Silicon Technologies were immersed in 30% H_2O_2, 70% H_2SO_4 (v:v) acid solution and heated at 383 K for 30 minutes. The surfaces of the Silicon wafers are protected by an oxide layer. This acid solution (called a *piranha* solution) removes all organic contaminants and binds more hydroxyl groups to the wafer surface, rendering the surface more hydrophilic without changing the surface topography [61]. Hydrophilic wafers were carefully rinsed in Milli-Q ultrapure water (18.2 MΩ·cm at 298 K) to remove leftover acid. Rinsing was performed by circulating water over the

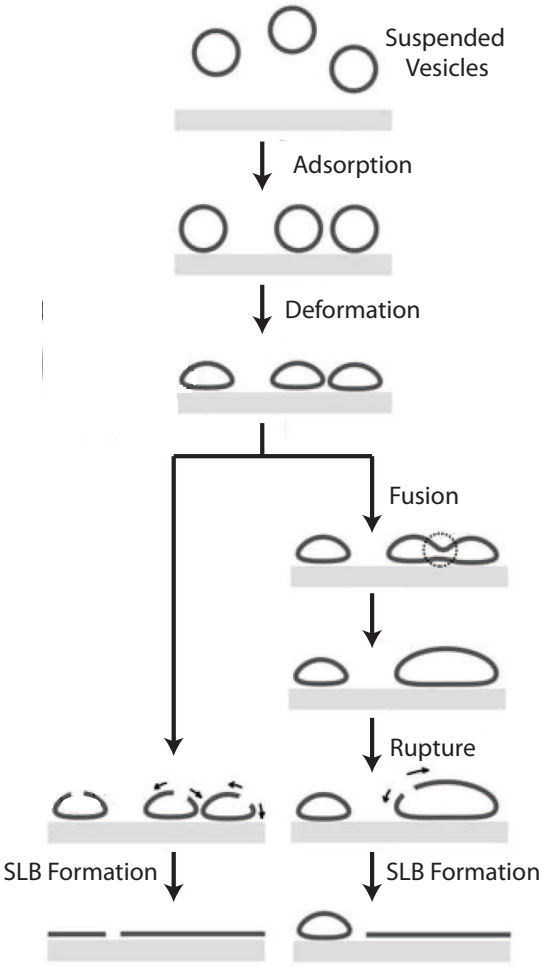

Figure 3.2: Pathways to bilayer formation by vesicle rupture and fusion as described by Hamai *et al.* [57].

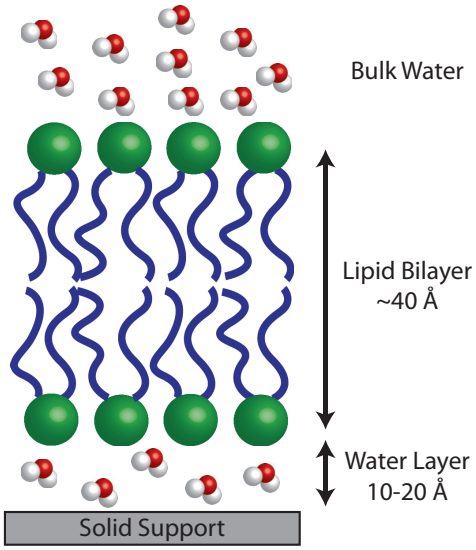

Figure 3.3: Schematic of a solid supported bilayer depicting the presence of a 10-20 Å water layer.

wafers and repeated with fresh water. Wafers were stored under ultrapure water until lipid deposition to limit contamination. A 200 mL buffer solution of 5×10^{-3}mol/L HEPES, 5×10^{-3}mol/L $MgCl_2$ and 100×10^{-3} KCl was prepared and heated to 328 K. DMPC obtained from Avanti Polar Lipids was added to the buffer at a concentration of 1.5 mg/mL. The lipid solution was sonicated for 15 hours at 328 K to produce small unilamellar vesicles. The cleaned wafers were immersed in this lipid solution for 1 hour at 328 K. This temperature (328 K) was chosen to be high enough to ensure bilayers were in the fluid (L_α) phase, yet low enough to prevent thermal decomposition. Wafers were then removed from the lipid solution and thoroughly rinsed with $\sim$2 L ultrapure water to remove any vesciles remaining on the bilayer surface. Rinsed wafers were annealed for 72 h at 328 K. The resulting bilayers were rehydrated with D_2O during the experiment.

3.2.2 Sample Environment for Diffusion Experiments

Annealed wafers were stacked in an Aluminium sample can as shown in Figure 3.4. No spacers were used between the wafers in the stack, however surface roughness and sample irregularities lead to μm scale wafer separations. The sample can cavity was

51.2 mm in diameter and 39.25 mm deep, which enforced a tight wafer stack. A ring of Indium wire was used to create a vacuum seal between the cover flange and the container flange. Indium is an ideal vacuum seal because it can adhere strongly ('cold weld') to various materials under pressure at room temperature. Indium also remains malleable at temperatures well below room temperature which allows it to accomodate any differences in thermal expansion of the sealed container. The flanges on the cover and container top were threaded for twelve screws to ensure the even pressure distribution required for a strong seal [62]. Aluminium spacers were employed to separate the stacked wafers from a round piece of filter paper placed on top of the wafer stack. The D_2O used for rehydration was absorbed by this filter paper before sealing the Aluminium can. In thermal equilibrium, a relative humidity of 100% developed inside the sample can which lead to full hydration of the bilayers. Neutron absorbing Cadmium and Borated Aluminium shields were employed to shield the parts of the sample can not containing sample. An unshielded area of 2.5 cm was sufficient such that neutrons scattering from any part of the sample could be detected, but scattering from other parts of the sample environment were minimized. An identical Aluminium sample can was prepared along with two cylindrical Silicon blocks (diameter 50 mm, similar to the wafers). These blocks were placed inside the second sample can and used as a lipid-free control sample. Wafer separation was much larger than the wavelength ($\sim$6 Å) of incident radiation, which allows wafer stack intereference effects to be discounted. As a result similarly sized silicon blocks were an effective a control. Wafers are also separated purely by lipids and water, so any signal arising from scattering in these areas was not considered background. A liquid Helium cryostat was employed to maintain a temperature tolerance of 1.0 K with a temperature range from 4 K to 300 K, however only temperatures between 240 K and 303 K were employed in this experiment. The cryostat flange (brown) was attached directly to the top of the sample can to ensure an even temperature distribution.

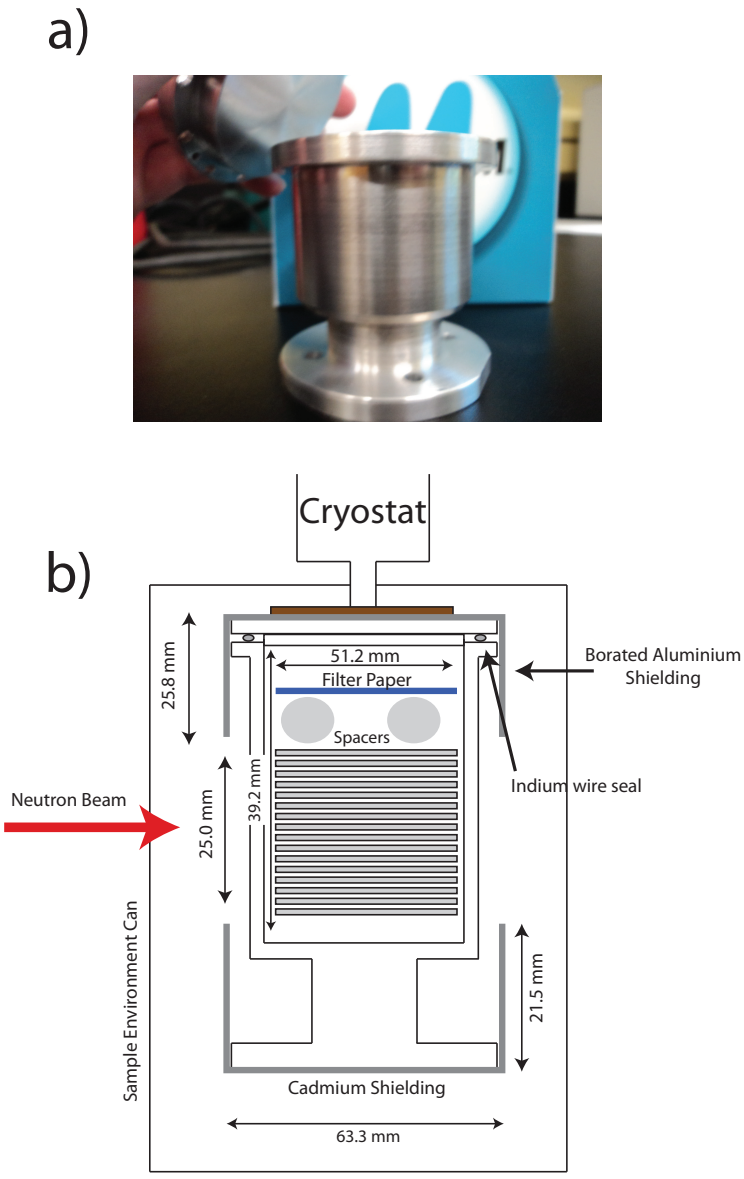

Figure 3.4: The bare Aluminium sample cell used in the single bilayer experiments is shown in a). Experimental setup of the sample can is depicted in b). The wafers were tightly stacked in the can cavity and separated from the hydrated filter paper by Aluminium spacers. No spacers were used between the individual wafers in the stack, however sample and substrate irregularities allowed hydration water to diffuse between wafers. The Aluminium can was sealed with Indium, attached to a cryostat and placed inside a larger Aluminium sample environment can. The areas of the sample can not containing sample were shielded with Cadmium and borated Aluminium as shown.

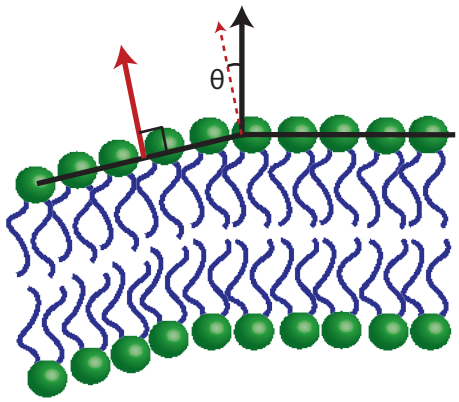

Figure 3.5: Two sections of membrane with different vertical orientations are shown. The angle θ between the bilayer normals represents the difference in their orientations. The average angle for an entire solid supported bilayer is its mosaicity.

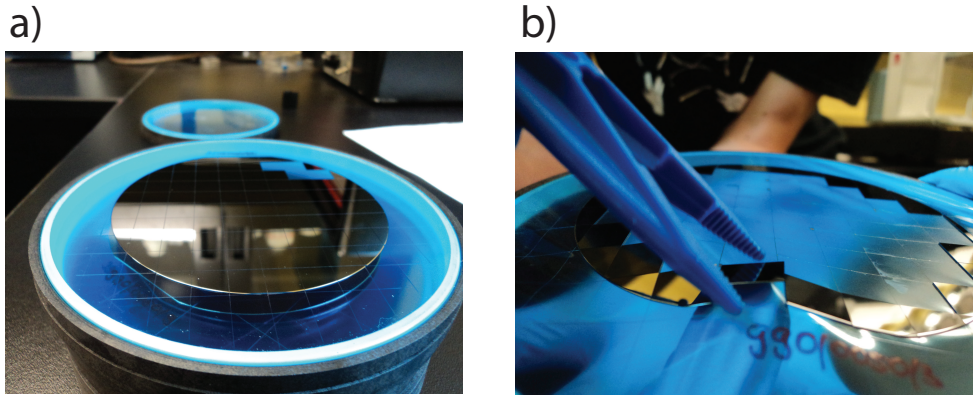

Figure 3.6: Silicon wafer container is shown in a). The blue material is the adhesive plastic layer. b) Demonstrates the removal procedure which minimizes contact with the adhesive.

3.3 Multilamellar Solid Supported Bilayers

Multilamellar solid supported bilayers prepared with vesicle spreading are highly oriented. The average of the distribution of the bilayer normal vector called the *mosaicity* (see Figure 3.5) is reported on the order of 0.01^o [63]. Highly oriented multilamellar solid supported bilayers were prepared by vesicle spreading for the x-ray and neutron ethanol experiments. The preparation of x-ray samples is described below. The neutron ethanol samples were prepared similarly by employing the ultrasonic preparation on 2" Silicon wafers, which is discussed in detail in chapter 7.

3.3.1 Wafer Preparation

Highly oriented multilamellar solid supported bilayers were prepared on single-side polished Silicon wafers. Pre-cut 100 mm diameter, 300 μm thick Silicon (100) disks obtained from SilChem were pre-cut into 1×1 cm^2 wafers. Disks were delivered on an adhesive plastic layer with the polished side up as seen in Figure 3.6. Care was taken to remove the wafers from the adhesive layer without adhesive contamination. All wafers were inspected for adhesive residue before use. Wafers were isolated by pushing upwards on the plastic under the wafer and removed with plastic tweezers to prevent scratching the wafer surface (Figure 3.6b). All tweezers were cleaned with methanol and dried in nitrogen before use.

Lipids must be dissolved in a solvent for deposition on the wafers, however lipid solubility varies with lipid type as shown in Table 3.1 [63]. These solvents differ in their hydrophobicity, so wafers were prepared differently to allow the lipid solution to spread.

Lipid Solubility					
Solvent	DLPC	DMPC	DOPC	DPPC	DMPE
2-propanol	Y	Y	Y	Y	–
2,2,2-trifluoroethanol (TFE)	Y	Y	–	Y	N
chloroform	Y	Y	–	Y	Y
1:1 chloroform/methanol	–	Y	–	–	–
1:1 TFE/ethanol	–	Y	–	–	–

Table 3.1: Solubility of different lipids in different organic solvents. 'Y' indicates soluble and 'N' indicates not soluble. Table adapted from [63].

3.3.2 Ultrasonic Preparation

Before removing the wafers from the adhesive layer, a bath sonicator was heated to 313 K, and the water degassed for 5 minutes. Wafers were then placed in beakers of methanol such that they were completely submerged, but did not overlap. The wafers in the beaker were submerged in the bath sonicator and sonicated for 10 minutes. The wafers were then moved to a beaker of ultrapure water (resistivity 18.2 MΩ-cm at 298 K) and sonicated for an additional 10 minutes. This process was repeated for a total of two 10 minute water and methanol sonications each. The final sonication was conducted in methanol. Wafers were then rinsed thoroughly with methanol and allowed to dry before lipid deposition. This cleaning method provides a slightly hydrophobic surface.

3.3.3 APTES Preparation

For the x-ray experiments, we found that untreated and ultrasonically prepared pre-cut wafers wafers did not allow proper lipid solution spreading. Chloroform/2,2,2-trifluoroethanol (TFE) (1:1) solutions containing DMPC dewetted in less than 30 minutes, preventing uniform bilayer formation. This was potentially a result adhesive con-

tamination of the wafer surface. As a result, a monolayer of 3-Aminopropyltriethyloxysilane (APTES) was applied to each wafer to ensure a uniform surface for lipid deposition. Figure 3.7 shows reflectivity curves for an untreated (blue) and APTES prepared (red) wafers. Interference fringes due to the presence of a thin APTES film are observed in the red curve. The chemical structure of APTES is shown in Figure 3.8a. When in contact with the wafer surface, the APTES ethoxy group is exchanged with hydroxyl groups on the surface. These hydroxyl groups bond with other surface hydroxyl groups, producing structures shown in Figure 3.8b. Note that the cross-links shown in Figure 3.8b form only after exposures longer than 2 hours. After annealing the wafers for 12 hours at 388 K the APTES layer is covalently bonded to the wafer surface and may have polimerized (Figure 3.8c) [64]. This process is known as silanization. The amine (NH_2) group is generally found farther from the surface [65]. The nitrogen in the amine group has a greater electronegativity (3.04) than its Hydrogens (2.20), giving the Hydrogens a partial positive charge. This allows the Hydrogens to Hydrogen bond with surrounding fluid, and makes the surface more hydrophilic. In this way the APTES monolayer produces a surface of *medium* hydrophobicity with water advancing and receding contact angles of 50^o and 45^o respectively [64].

A piranha acid solution was prepared with 98% concentrated H_2SO_4 and 30% concentrated H_2O_2 at a ratio of 3:1 by volume. 70% H_2O_2 was diluted and added first to avoid dangerous exothermic reactions. 20 mL was sufficient to clean 10 1 $\times$ 1 cm^2 wafers simultaneously. Wafers were placed in this solution, covered with parafilm and heated to 298 K for at least 30 minutes. A 1% solution of APTES and 99% ethanol was prepared. A 1 mL syringe was filled with 0.2 mL of dry nitrogen. This nitrogen was ejected into 99% APTES purchased from Sigma-Aldrich, and 0.2 mL of APTES is drawn into the syringe. This syringe is then submerged in 19.8 mL of ethanol before ejecting the APTES. This 20 mL APTES solution is sufficient to cover 10 wafers in an APTES monolayer. A separate pair of clean plastic tweezers were used to immerse the wafers in the APTES solution. The APTES solution was covered with parafilm, heated to 298 K and placed on the tilting incubator (20 speed, 3 tilt) for 12-24 hours (see Figure 3.9). The tilting incubator creates a circular flow in the beaker to ensure an even APTES distribution and prevent buildup on the surface of the wafers. The wafers were then placed in a clean pyrex dish and annealed in

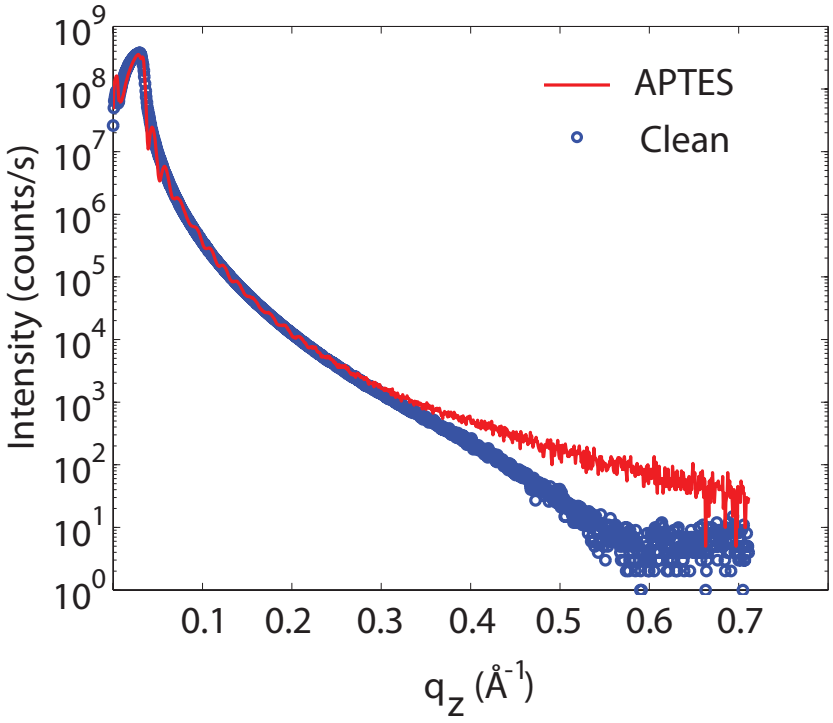

Figure 3.7: Reflectivity curves of a clean wafer (blue) and a wafer coated in APTES (red).

a vacuum at 388 K for 3 hours. Annealed wafers were rinsed in methanol, covered in parafilm and stored under methanol if not used immediately. At this point the APTES layer on the wafer surface should appear as in Figure 3.8c and the wafers are ready for lipid deposition.

Thorough rinsing was performed after removal of the wafers from both the acid and APTES solutions. Each wafer was removed from the acid (APTES) using ethanol (methanol) cleaned plastic tweezers and rinsed three times each with 20-50 mL of ultrapure water and ethanol (methanol). After APTES deposition an additional rinsing was performed using a methanol filter and new methanol to avoid any possible contaminants in the spray bottle.

We found that for DMPC disolved in 1:1 chloroform:trifluoroethanol the hydrophilic substrate provided by the APTES preparation demonstrated optimal solvent spreading.

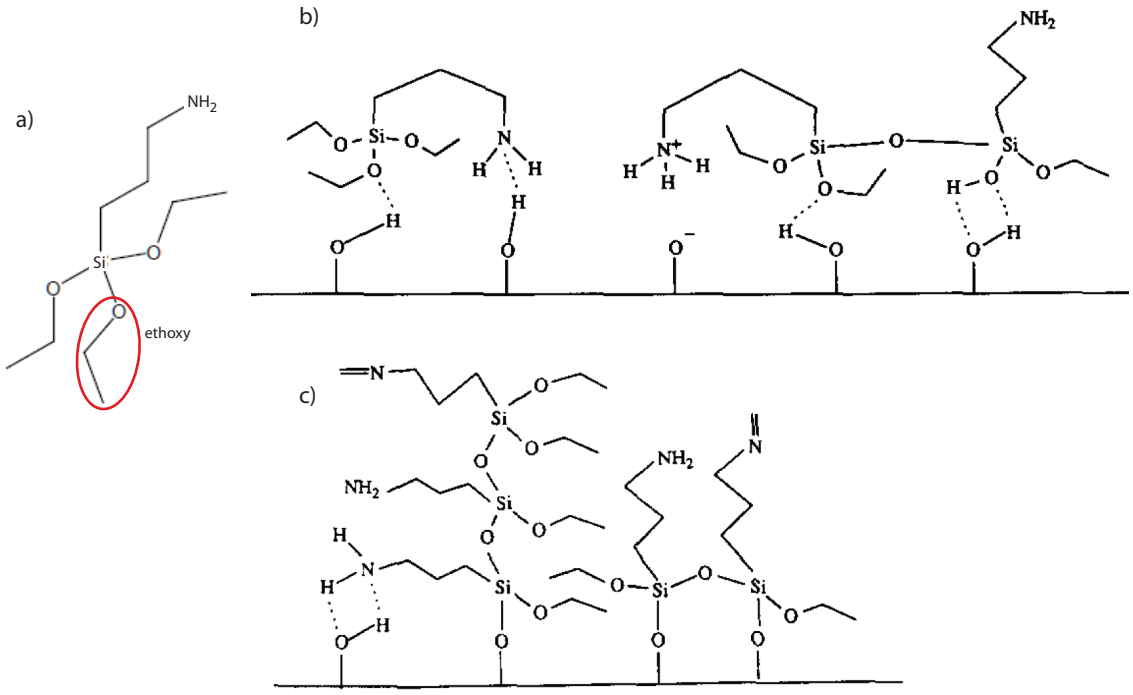

Figure 3.8: a) Chemical structure of APTES. The ethoxyl group is shown in red and exchanged with hydroxyl groups on the wafer surface. b) APTES structures after deposition on Silicon-oxide surface. c) APTES structures after annealing for 12 hours.

Figure 3.9: The VWR tilting incubator is shown here with wafers in APTES. The rate and angle of tilt can be controlled, as well as the temperature inside the enclosure.

3.3.4 Lipid Deposition

DMPC was purchased from Avanti Polar Lipids. 15-30 mg of DMPC was weighed and disolved in 1-2 mL 2,2,2-trifluoroethanol (TFE):chloroform (1:1 by volume) with final concentration 15 mg/mL. This lipid solution was mixed with the analog vortex mixer before use. If the lipid solution was not used immediately it was stored at 277 K and re-vortexed before use. The tilting incubator was heated to 313 K and the lipid solution was placed inside to equilibrate. Labelled plastic petri dishes and methanol-cleaned metal pedestals were also placed inside the incubator. Metal pedestals were placed inside each petri dish, and the tilting incubator was started at tilt 1, speed 15. The pedestals helped to prevent wicking of lipid solution to the wafer underside. Cleaned wafers were individually selected for deposition with plastic tweezers or teflon tweezers wrapped in Aluminium foil. The selected wafer was rinsed in methanol and carefully dried with compressed nitrogen. The wafer was also dabbed on the unpolished side with Kimtech precision wipes to prevent future wicking of the lipid solution onto the bottom of the wafer (see Figure 3.10a). The wafer was then placed on the metal pedestal in a petri dish on the tilting incubator, and the petri dish covered. The solution was removed from the osillator and a 50 μL pipette was prepared by placing the pipette tip near the surface of the lipid solution and ejecting rapidly $\sim$10 times. This provides a positive vapour pressure in the pipette tip preventing pressure mismatches during pipetting, which cause solution leakage. 50 μL of lipid solution was carefully pipetted onto the wafer, and the petri dish covered. After all wafers were deposited, they were tilted for at least 30 minutes or until the lipid solution had evaporated. The petri dishes with pedestals and wafers were placed in the vacuum oven at 313 K for 12-24 hours to remove any trace of solvent.

3.3.5 Hydration

Annealed bilayers were rehydrated before use. Annealed wafers placed in petri dishes and a beaker of saturated K_2SO_4 solution were placed and sealed in a glass hydration container with parafilm. The hydration container was allowed to equilibrate at 293 K in an incubator. The temperature of the incubator was increased as gradually as possible from 293 K to 303 K over a period of at least 3 hours. During this time the evaporating K_2SO_4 solution created an environment with relative humidity between

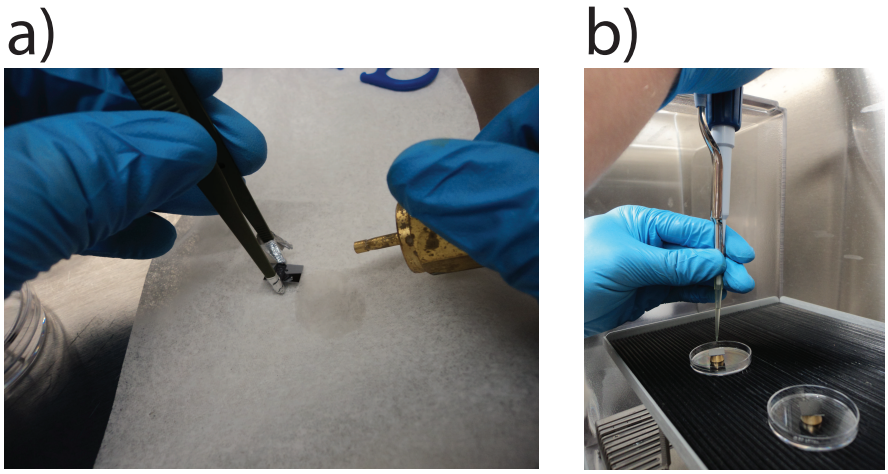

Figure 3.10: After cleaning with methanol, wafers were dried in nitrogen and their unpolished sides dabbed to remove methanol on the wafer underside (a). Pipetting technique is shown in b). The tilting incubator was tilting the wafers constantly during this process, so great care was taken to steady the pipette and deposit the solution in the centre of the wafer.

97 and 98% [66]. Table 3.2 illustrates the relative humidity change with temperature in saturated salt solutions. Altering temperature or relative humidity (by changing salts) too quickly produced bilayers with irregular spheres on the surface as shown in Figure 3.11a. Separate hydration steps with KCl (85 - 83% relative humidity) from 293 K to 303 K followed by K_2SO_4 (98 - 97% relative humidity) from 293 K to 303 K also produced the spherical defects. The only solution was to increase the temperature as slowly as possible at a relatively constant humidity. Any hydration faster than 3 hours produced defects as well.

3.3.6 Sample Environment for X-ray Experiments

Hydrated samples were placed on the Aluminium pillar at the centre of the vapour chamber shown in Figure 3.12 for examination with x-rays. The 51.18 mm diameter central pillar may accomodate 1 $\times$ 1 cm^2, 2 $\times$ 2 cm^2 square and 2 inch diameter circular sample sizes. The trough shown in blue is 7.76 mm deep and 11.21 mm wide with total volume 31.0 mL and was used to hydrate the bilayers from the vapour phase during the experiment. 5 mL ultrapure water and water-ethanol mixtures were

Salt Solution Relative Humidity (RH%)		
Temperature (^{o}C)	KCl	K_2SO_4
0	88.61 ± 0.53	98.77 ± 1.1
5	87.67 ± 0.45	98.48 ± 0.91
10	86.77 ± 0.39	98.18 ± 0.76
15	85.92 ± 0.33	97.89 ± 0.63
20	85.11 ± 0.29	97.59 ± 0.53
25	84.34 ± 0.26	97.30 ± 0.45
30	83.62 ± 0.25	97.00 ± 0.40
35	82.95 ± 0.25	96.71 ± 0.38
40	82.32 ± 0.25	96.41 ± 0.38
45	81.74 ± 0.28	96.12 ± 0.40
45	81.20 ± 0.31	95.82 ± 0.45

Table 3.2: Relative humidities of saturated salt solutions at temperatures between 0^oC and 50^oC [66].

sufficient to maintain hydration for 18 hour scans. Double layer 13 μm thick Kapton windows are shown in yellow. Kapton is a polyimide (PI) which is nearly transparent to x-rays and experiences minimal radiation damage. These windows maintain vapour pressure while allowing x-rays through the chamber.

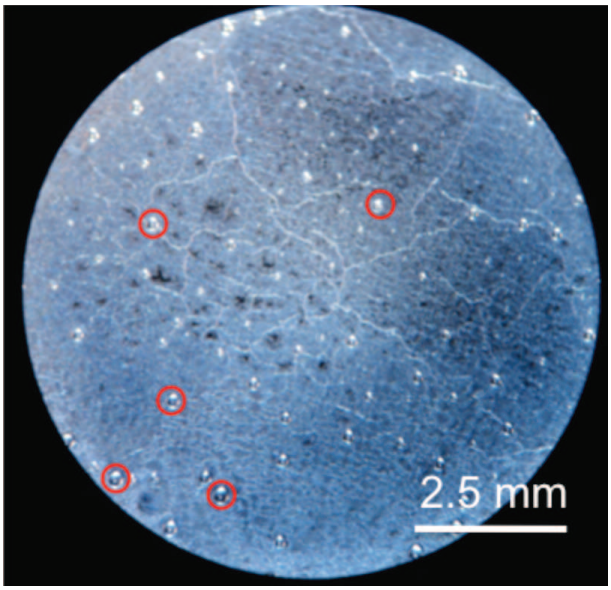

Figure 3.11: Optical microscope image of multilamellar DMPC sample. Bubble structures produced by fast hydration are shown in red.

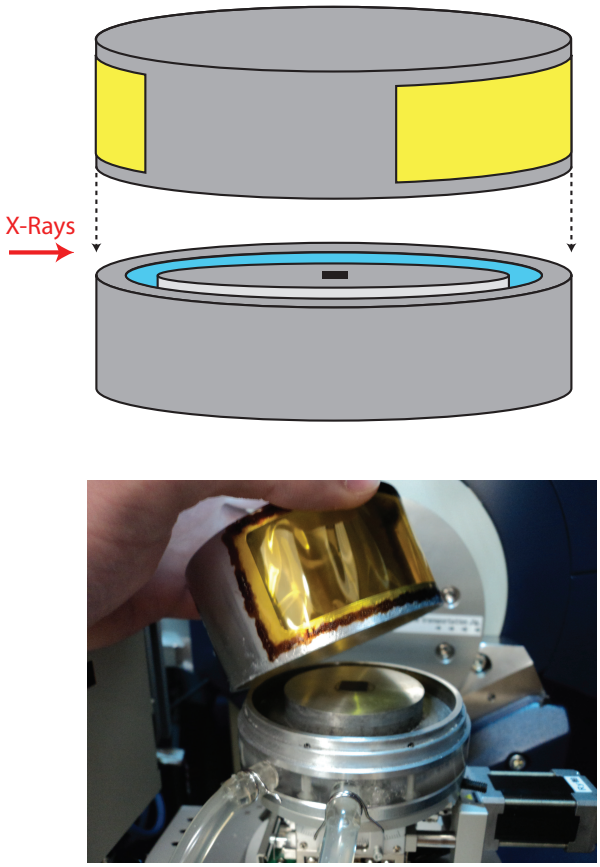

Figure 3.12: Schematic of x-ray vapour chamber. The solution is placed in the trough (in blue) surrounding the central pillar on which the sample (in black) is mounted. We are able to maintain a pressurized environment by using carefully placed Kapton windows (yellow), which are nearly transparent to x-rays.

Chapter 4

Scattering

Scattering techniques are ideal for the study of lipid bilayers. Radiation such as neutrons or x-rays provide non-invasive, non-destructive probes of bilayer structure and dynamics from mesoscopic to microscopic lengthscales. Figure 4.1 illustrates the range of biological dynamics accessible to scattering techniques. Scattering techniques allow the energy and momentum transfer between incident radiation and lipid bilayer samples to be observed. This information is interpreted with scattering theory to obtain information about the structure and dynamics of the bilayer.

4.1 Scattering Theory

The wavelength of the incident and scattered radiation describes the *wavevectors* $\boldsymbol{k}_i$ and $\boldsymbol{k}_f$ where $k = \frac{2\pi}{\lambda}$. The wavevector is related to the radiation momentum by $\boldsymbol{\rho} = \hbar\boldsymbol{k}$. The energy of the radiation can be defined in terms of incident and scattered wavevectors according to:

$$E_{particle} = \frac{\hbar^2 k^2}{2m} \tag{4.1}$$

$$E_{wave} = \frac{hc}{\lambda} = \hbar k c \tag{4.2}$$

where $E_{particle}$ and E_{wave} represent the energy of particle (neutron) and wave (x-ray) radiation respectively. The energy exchange between the radiation and the sample

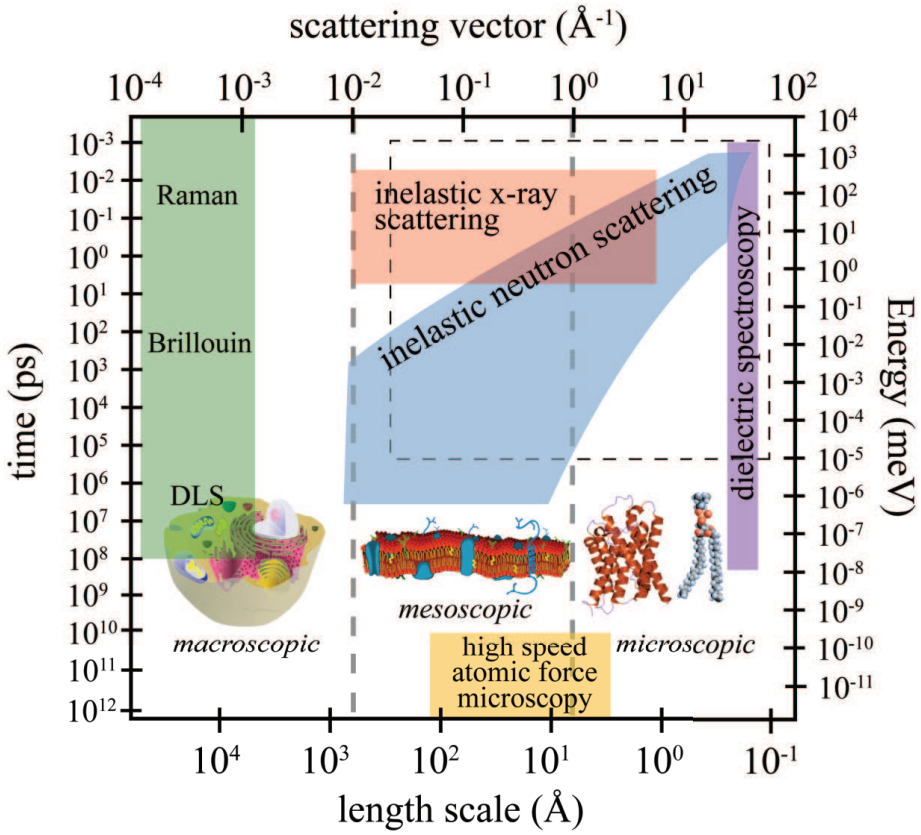

Figure 4.1: Accessible range and timescales of various scattering techniques including neutron, light and x-ray scattering. The dashed rectangle indicates the range accessible by current high performance computer simulations [3].

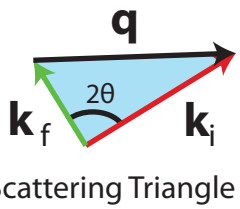

Figure 4.2: The scattering triangle with $\boldsymbol{k}_i$, $\boldsymbol{k}_f$ and $\boldsymbol{q}$.

is called the *energy transfer* $\hbar\omega$ and is defined by the difference in magnitude of the wavevectors according to equations 4.1 and 4.2. For zero and nonzero energy transfer, radiation undergoes elastic and inelastic scattering respectively. To produce elastic scattering, $\boldsymbol{k}_i$ must equal $\boldsymbol{k}_f$, where the wavevectors are described by Braggs law:

$$2dsin\theta = \lambda, \tag{4.3}$$

where d is the lattice spacing perpendicular to the surface and θ is the angle between the surface normal and the incident radiation. We define the *scattering vector* or *momentum transfer* as the vector difference between the initial and scattered wavevectors.

$$\boldsymbol{q} = \boldsymbol{k_i} - \boldsymbol{k_f} \tag{4.4}$$

The *scattering triangle* is formed by $\boldsymbol{k}_i$, $\boldsymbol{k_f}$ and $\boldsymbol{q}$ as shown in Figure 4.2.

The reciprocal space of a regular bravais lattice is defined as the set of all wavevectors $\boldsymbol{k}$ which lead to constructive interference when scattered from a this lattice. Each point on the reciprocal lattice defined by reciprocal lattice vectors h, k, and l corresponds to a wavelength where elastic scattering may occur. The magnitude of the scattering vector can also be defined by the scattering triangle and cosine law.

$$|\boldsymbol{q}| = \frac{4\pi sin\theta}{\lambda} = \frac{2\pi}{d} \tag{4.5}$$

Since the scattering vector is a difference of wavevectors, it can also be related to a real-space lengthscale d. The flexibility of many scattering techniques arises from the ability to change the energy and momentum transfer independently.

The probability that incident radiation will interact with the sample is given by

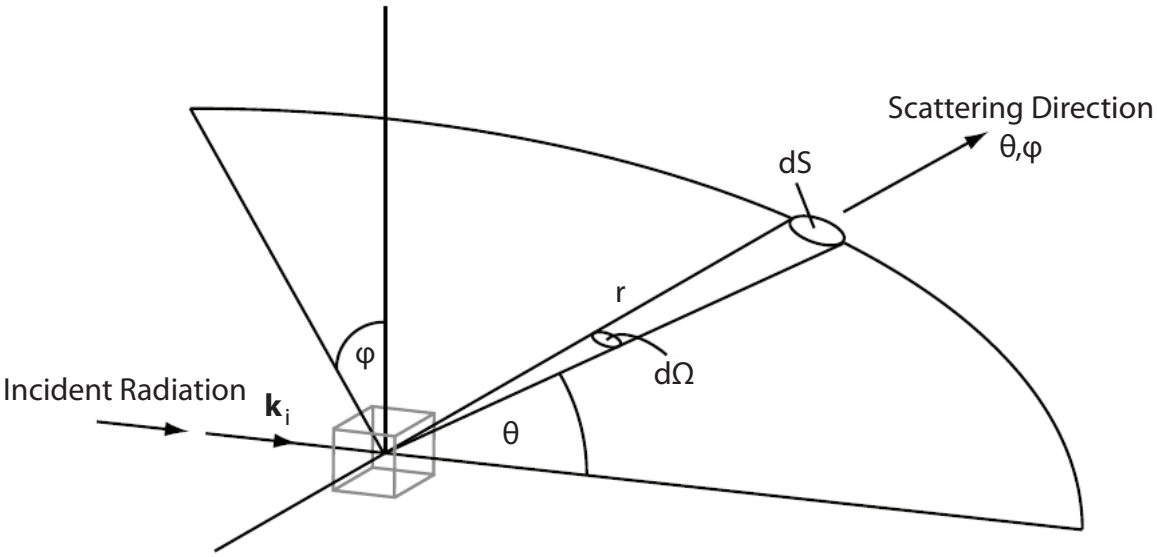

Figure 4.3: The differential cross section as defined by the scattering angles (θ, ϕ), and area dS a distance r from the scattering centre [67].

the scattering cross section. Scattering cross sections are defined by the scattering geometry as shown in Figure 4.3. The scattered intensity can be expressed in terms of the *double differential cross section* $\frac{d\sigma^2}{d\Omega dE_f}$ which is the probability of radiation being scattered per second through a small solid angle $d\Omega$ in the final energy range dE_f normalized by the flux of incident radiation. For incident flux Φ_i and n particles scattered in $d\Omega$ and dE_f, the double differential cross section, *differential cross section* $\frac{d\sigma}{d\Omega}$ and *total cross section* σ are described as follows:

$$\frac{d\sigma^2}{d\Omega dE_f} = \frac{n}{\Phi_i d\Omega dE_f} \tag{4.6}$$

$$\frac{d\sigma}{d\Omega} = \int_0^\infty \frac{d^2\sigma}{d\Omega E_f} dE_f \tag{4.7}$$

$$\sigma = \int_0^{4\pi} \frac{d\sigma}{d\Omega} d\Omega \tag{4.8}$$

The total cross section σ is a measure of the total scattering probability which

is independent of the energy and scattering angle. The number of the scattering events detected is directly proportional to these cross sections and the incident flux: $N_{detector} = \Phi_i d\sigma = \Phi_i \frac{d\sigma}{d\Omega} d\Omega$. A summary of total neutron and x-ray scattering cross sections is shown in Figure 4.4. The scattered intensity through a cross section is dependent on the nature of the incident radiation and sample structure. The sample structure is described by the form factor and structure factor. The geometrical structure factor of a n-atom crystal lattice denoted by vectors $\boldsymbol{R}$ describes the amplitude of the Bragg interference structure of the scattered radiation.

$$S(\boldsymbol{q}) = \sum_{j=0}^{n} f_j(\boldsymbol{r}) e^{i\boldsymbol{q}\cdot\boldsymbol{R}_j} \tag{4.9}$$

The atomic form factor $f_j(\boldsymbol{q})$ is defined as the normalized amplitude of scattering from within the jth scattering particle or unit cell:

$$f_j(\boldsymbol{q}) = \int \rho(\boldsymbol{r}) e^{i\boldsymbol{q}\cdot\boldsymbol{r}} d^3\boldsymbol{r} \tag{4.10}$$

where $\boldsymbol{r}$ is the vector describing the displacement of the scattering from the particle centre of mass, and $\rho(\boldsymbol{r})$ is the spatial density of the scatterer about the centre of mass. For x-rays $\rho(\boldsymbol{r})$ describes the density of the electron cloud. We can define the differential cross section for x-ray scattering from a crystal lattice as follows:

$$\frac{d\sigma}{d\Omega}_{xray} = b^2 P |f(\boldsymbol{q})|^2 |S(\boldsymbol{q})|^2 \tag{4.11}$$

The b^2P term is a result of Thompson scattering from a single electron, where b is the *scattering length* which describes the strength of the interaction between radiation and scattering centre, and P is the polarization of the x-ray source. For the unpolarized beam in an x-ray diffractometer, $P = \frac{1}{2}(1 + cos^2\theta)$, where θ is the angle between the horizontal and scattered beam. The magnitude of the three dimensional x-ray structure factor is given as $|S(\boldsymbol{q})|^2 = Nv\delta(\boldsymbol{q})$ where N is the number of unit cells, v is the volume of the unit cell and the delta function describes the Bragg condition.

For neutrons, the density $\rho(\boldsymbol{r})$ is a delta function centered at the nucleus, which interacts with incident neutrons with experimentally determined scattering length b. This allows $\rho(\boldsymbol{r})$ to be replaced by an effective potential $V(\boldsymbol{r})$ which is a discrete sum

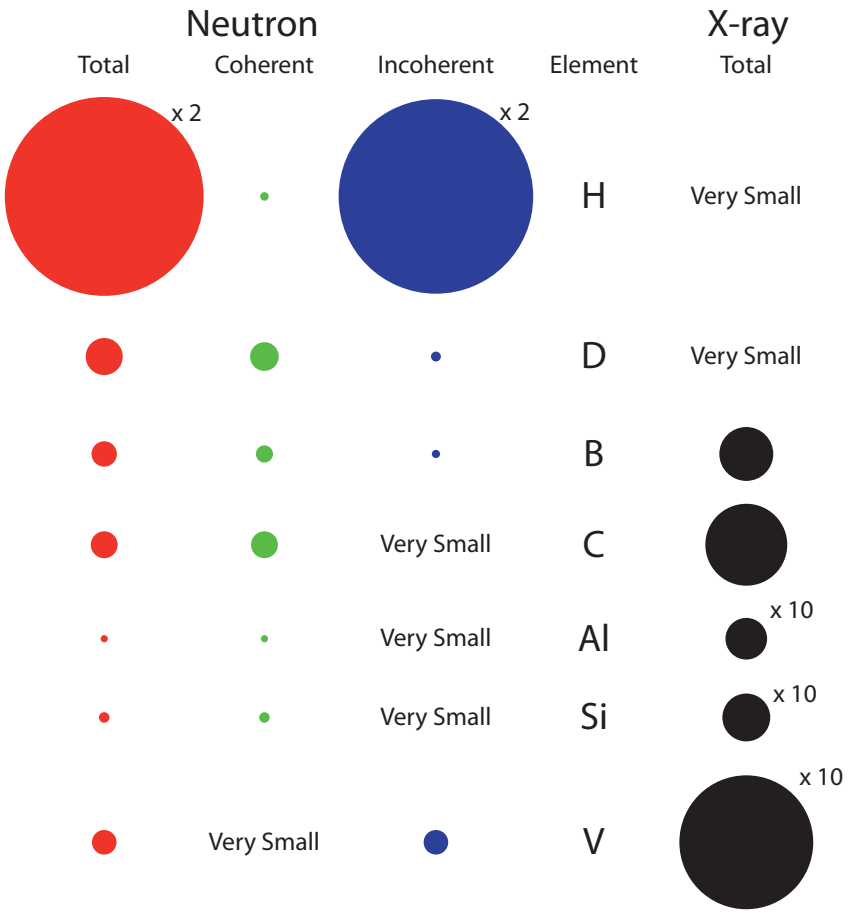

Figure 4.4: Comparison of neutron and x-ray cross sections for a selection fo elements. The area of the circles represents the scattering cross section and are to scale unless otherwise indicated. Neutron cross sections were taken from [67], and X-ray cross sections were obtained from mass attenuation values in the National Institute for Standards and Technology (NIST) physical reference data database (http://www.nist.gov/pml/data/).

over the scattering lengths of all scattering particles.

$$V(\boldsymbol{r}) = \sum_j b_j \delta(\boldsymbol{r} - \boldsymbol{R_j}) \tag{4.12}$$

This potential is weak enough that we neglect all but first order scattering. The neutron differential cross section may then be defined as the magnitude of the sum over all these interactions as shown in equation 4.13.

$$\frac{d\sigma}{d\Omega}_{neutron} = \left| \int e^{i\boldsymbol{q}\cdot\boldsymbol{r}} V(\boldsymbol{r}) d\boldsymbol{r^3} \right|^2 = \left| \sum_j b_j e^{i\boldsymbol{q}\cdot\boldsymbol{R_j}} \right|^2 = \sum_{j,k} b_j b_k e^{-i(\boldsymbol{R_k}-\boldsymbol{R_j})\cdot\boldsymbol{q}} \tag{4.13}$$

In its penultimate form, the neutron differential cross section appears as simply the magnitude of the structure factor with form factor b_j. The scattered intensity through a cross section is therefore $\propto |S(\boldsymbol{q})|^2$ for both x-rays and neutrons.

The geometrical structure factor tells us only about elastic processes. To explain inelastic intensities, the double differential cross section must be developed. The energy and time distribution of the scattered radiation must be taken into account. Conservation of energy allows the energies of the scattered radiation to be represented as a delta function:

$$\delta(dE_{system} + \hbar\omega) = \frac{1}{2\pi\hbar} \int_{-\infty}^{\infty} e^{-it\frac{dE_{system}}{\hbar}} e^{i\omega t} \delta t \tag{4.14}$$

The time dependence of scattered radiation is taken into account by averaging particle separations over a time t. Combining these two effects with the differential cross section for neutrons above produces the double differential cross section.

$$\frac{d^2\sigma}{d\Omega dE_f}_{neutrons} = \frac{k_f}{2k_i\pi\hbar} \sum_{j,k} b_j b_k \int_{-\infty}^{\infty} \langle e^{-i\boldsymbol{q}\cdot[\boldsymbol{R_k}(0)-\boldsymbol{R_j}(t)]} \rangle e^{i\omega t} \delta t = N \frac{k_f}{k_i} S(\boldsymbol{q},\omega)_{neutrons} \tag{4.15}$$

where $S(\boldsymbol{q},\omega)$ is the *dynamical structure factor* or scattering law for a series of N scattering centers. A similar development for x-rays leads to the following scattering law [68].

$$\frac{d^2\sigma}{d\Omega dE_f}_{xray} = \frac{k_f}{k_i}\left(\frac{e^2}{mc^2}\right)^2 |p_\alpha^* \cdot p_\beta| S(\boldsymbol{q},\omega)_{xray} \tag{4.16}$$

where p_α and p_β are the initial and final x-ray polarization states respectively.

For neutrons, the scattering law (equation 4.15) is dependent on the scattering lengths b of the scattering nuclei. The total cross section of a nucleus is given as $\sigma = 4\pi b^2$ corresponding to the surface of a sphere of radius b. However since the strength of the interaction between neutron and nucleus (given by b) depends on the nuclear structure of the scattering nuclei, b changes significantly between elements, isotopes and nuclear spin states. A neutron interacting with a series of nuclei will experience a range of cross sections depending on the atomic purity of the sample. This gives rise to *coherent* and *incoherent* scattering. To account for this effect, we divide equation 4.15 into components dependent on coherent and incoherent cross sections defined in terms of the mean and variance of the scattering lengths: $\sigma_{coh} = 4\pi\langle b\rangle^2$ and $\sigma_{inc} = 4\pi[\langle b^2\rangle - \langle b\rangle^2]$ as demonstrated in Figure 4.5. Coherent scattering corresponds to the scattering that would occur if all nuclei had the average scattering length. Coherent scattering varies strongly with scattering angle (θ) and demonstrates constructive interference. Incoherent scattering corresponds to the isotropic scattering from randomly distributed defects and depends only on the number of nuclei N.

We now have four types of scattering: elastic coherent scattering, elastic incoherent scattering, inelastic coherent scattering and inelastic incoherent scattering. Elastic coherent scattering is useful for probing the equilibrium structure, while inelastic coherent scattering probes collective dynamics. Elastic and inelastic incoherent scattering are related to single-particle structure or dynamics such as diffusion. The term *quasi-elastic* is used to describe processes which are not elastic, but do not demonstrate a well defined frequency. This type of scattering results in primarily incoherent scattering distributed about $\omega = 0$ and is related to single particle dynamics and local relaxation processes. Figure 4.6 shows a typical excitation spectrum. While relaxational processes lead to a quasi-elastic broadening of the central energy resolution, collective fluctuations lead to inelastic excitations with well defined frequencies.

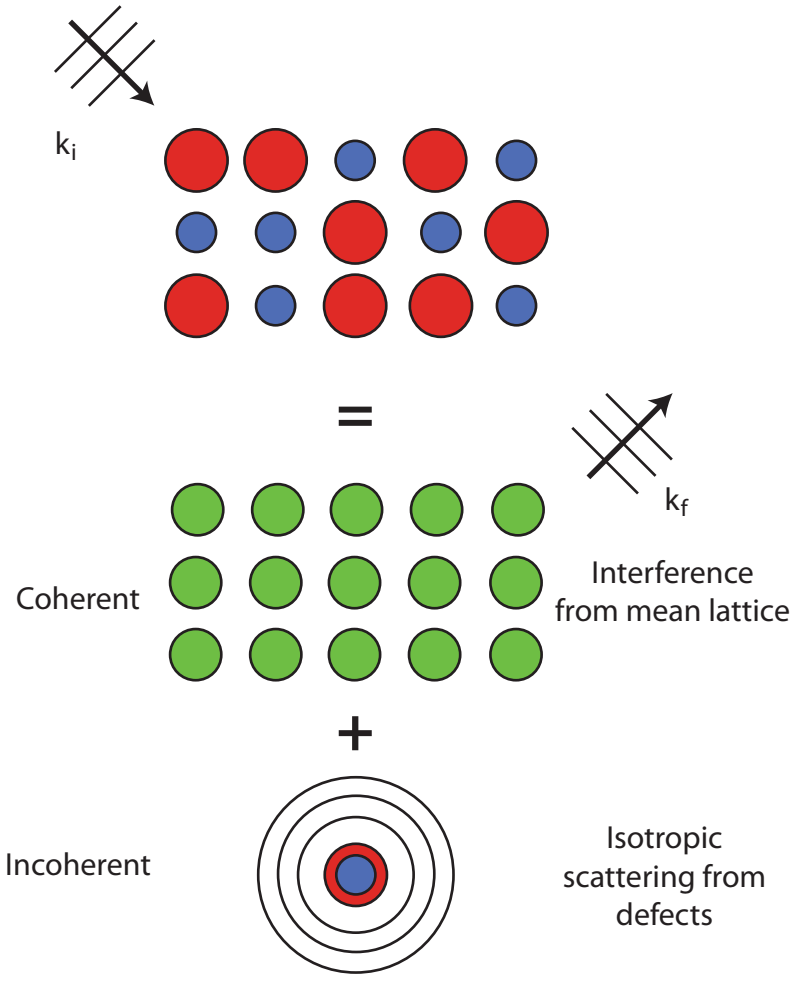

Figure 4.5: Coherent and incoherent scattering [8].

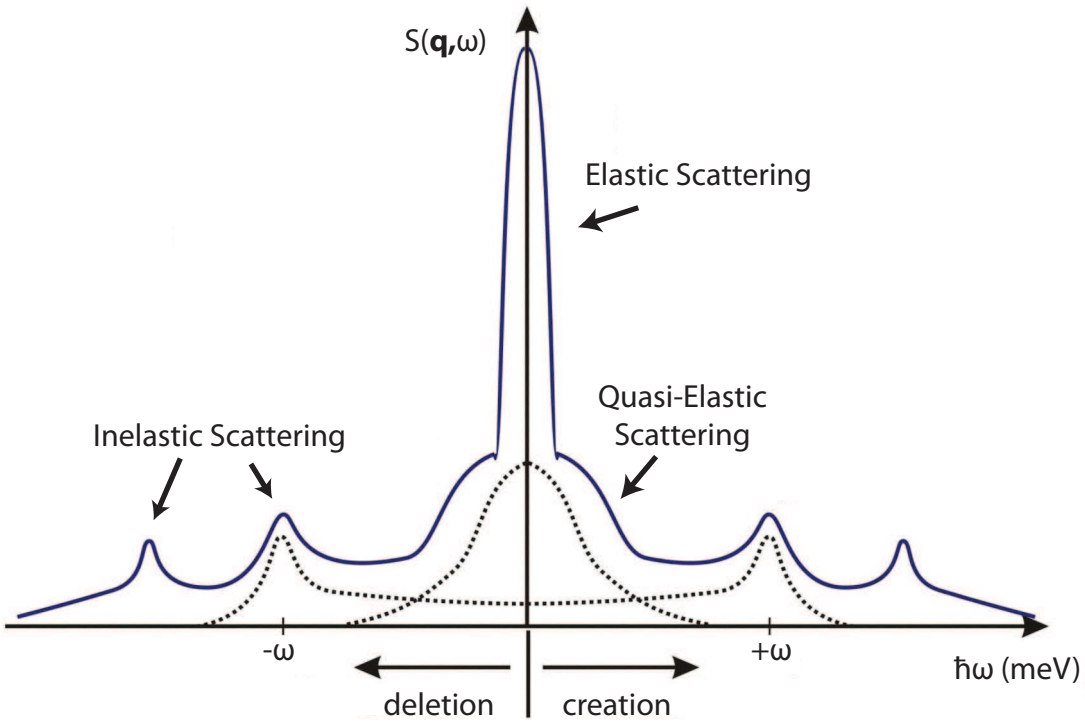

Figure 4.6: A profile of how the different types of scattering appear in the dynamical structure factor as a function of ω.

4.2 Properties of Neutrons and X-rays

Neutrons and x-rays are ideal probes for soft condensed matter. Table 4.1 contains a summary of neutron and x-ray properties. Neutrons are uncharged nuclear particles with mass 1.68×10^{-27} kg and spin $\frac{1}{2}$. Neutron energies vary between eV to MeV, however a room temperature, or 'thermal', neutron travels at ∼2200 m/s, with energies of ∼25 meV and wavelengths ∼0.2 nm. Due to their uncharged nature, neutrons penetrate the electron cloud and interact weakly with atomic nuclei. Thermal neutron wavelengths are much larger than the nuclei which leads to isotropic scattering. Neutrons generally penetrate deeper into materials at lower energies than other probes, which is advantageous for examining biological materials. The presence of nuclear spin which interacts with unpaired spins in magnetic materials may expose magnetic ordering and substructure. Neutrons also survive 885 seconds before undergoing β decay, which leaves plenty of time for experimentation. Variability in the scattering length allows distinction of light elements (such as Hydrogen) in the presence of heavier elements. Differences in the scattering length between isotopes allows the distinction of particular signals by selective labelling or contrast matching. In particular the difference in the coherent scattering cross sections of Hydrogen and Deuterium (^{2}H, or D) allows labelling structures in biological systems.

X-ray and neutron properties		
–	X-rays	Neutrons
Nature	Wave	Particle
Mass	0	1.68×10^{-27}
Velocity	c	2200 m/s (Thermal)
Momentum	$\frac{\hbar}{\lambda}$	mv
Charge	–	–
Spin	–	$\frac{1}{2}$

Table 4.1: X-ray and neutron properties.

In contrast, x-rays are a form of electromagnetic radiation with wavelengths from 0.01 to 10 nm. X-rays are uncharged, massless, spinless and travel at the speed of light. X-ray photons also interact with the the electron cloud surrounding the nucleus. As a result, x-ray scattering cross sections depend on the number of electrons and increase with atomic number. Increased scattering from larger elements makes observations

of light elements difficult. Cross section contrast between neighbouring elements is also small, which makes them difficult to distinguish. X-rays do not interact with the nucleus or spin states which means all atoms of the same element scatter identically. As a result, x-rays do not exhibit incoherent scattering.

Chapter 5

Instrumentation

5.1 Neutron Instrumentation

5.1.1 Neutron Sources

Neutrons may be produced by alpha particle bombardment, deuterium-tritium fusion, electron Bremsstrahlung gamma irradiation, nuclear fission and spallation [67]. However only nuclear fission and spallation yield sufficient neutrons for experimental scattering [67, 69]. Neutrons produced by fission require a nuclear reactor core and yield ∼1 experimental neutron per fission [67]. Fission depends on the instability of large nuclei such as Uranium-235. Proton coulomb repulsion competes with the attractive short range strong nuclear force which keeps nuclei together. The basic fission reaction for ^{235}U is shown in equation 5.1.

$$n_{thermal} + ^{235}U \rightarrow 2 fission fragments + 2.5 n_{fast} + 180 MeV \tag{5.1}$$

Low energy (∼1 meV) neutrons are absorbed by the ^{235}U nucleus which forms the unstable ^{236}U nucleus. ^{236}U decays into Barium and Krypton fragments and an average of 2.5 neutrons with energies between 1 and 2 MeV [67, 69]. The rate of reaction is controlled by raising or lowering neutron absorbing Boron control rods. A schematic of a nuclear reactor core is shown in Figure 5.1.

A 10 MW reactor produces 8.5×10^{17} neutrons per second in the entire reactor volume with energies distributed as in Figure 5.2 [67]. Neutrons produced can be

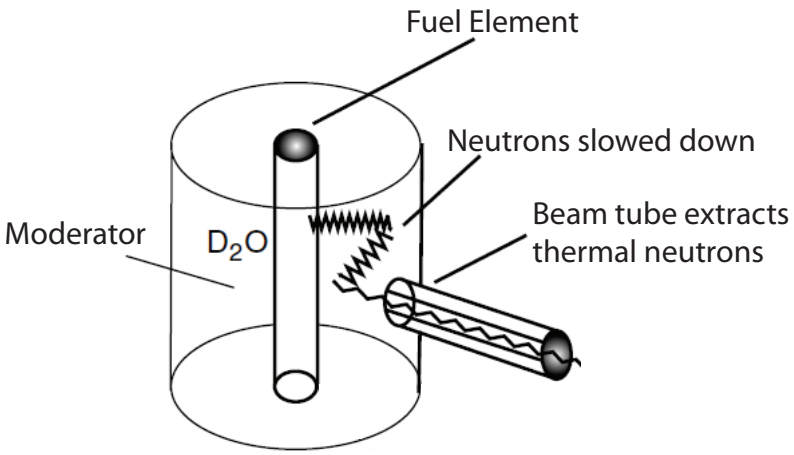

Figure 5.1: A schematic of the nuclear reactor core in the High Flux Reactor at the Institut Laue Langevin is shown. Neutrons generated by reaction in the core are slowed down by the moderator before either reacting again, or escaping through a beam tube [67].

Neutron Classification	
cold	$<$ 10 meV
thermal	10 - 100 meV Å
hot	100 - 500 meV
epithermal	500 meV - 1 MeV
fast	$>$ 1 MeV

Table 5.1: Neutron energy classifications.

classified as in Table 5.1. The fast neutrons produced are too high energy to continue the chain reaction, so the neutrons are slowed down by repeated collision with a liquid moderator until they are in equilibrium. Neutron interactions with moderator molecules such as D_2O and H_2O involve rotations about the molecular centre of mass, so small molecules with light atoms such as H or ^{2}H (D) are preferred to reduce the number of required collisions [69]. For D_2O, 25 collisions are required before neutrons equilibrate near 1 meV [69]. Moderated neutrons sustain the chain reaction, and by allowing some to escape through beam tubes, experimental neutrons are obtained. A good moderator slows the neutrons quickly, but also provides a peak flux of thermal

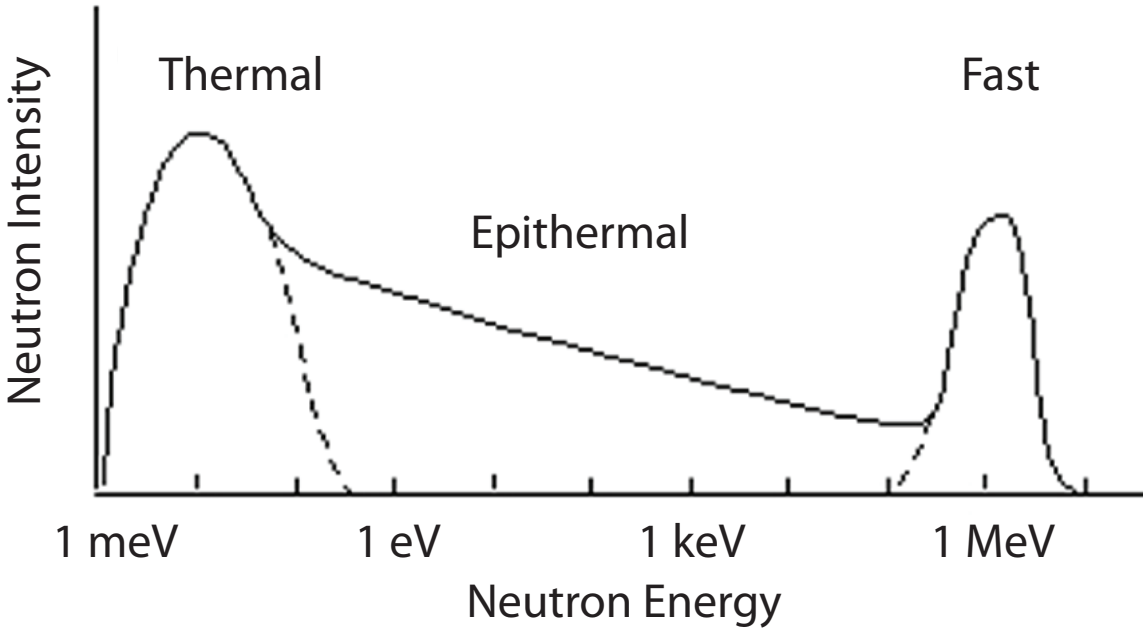

Figure 5.2: Nuclear reactor neutron energy spectrum. Intensities are not drawn to scale. Neutrons are classified as thermal, epithermal or fast, depending on their energy as shown in Table 5.1 [67].

neutrons a short distance (thermal diffusion length) from the core, where they are easily accessible to inserted beam tubes. The thermal diffusion length of thermal neutrons in D_2O is 1 m, where only 10 cm is required for moderation, which makes it an excellent moderator [69]. While modern spallation sources boast two orders of magnitude more flux, reactor sources provide a broader neutron energy distribution (particularly more cold neutrons) which provides more experimental flexibility.

A schematic of the High Flux Reactor core at the Institut Laue Langevin is shown in Figure 5.1. A power of 58 MW is generated from a single fuel element composed of 93% enriched ^{235}U vanes with a total mass of 8.57 kg. The reactor core is 40 cm in diameter and is surrounded by a 2.5 m diameter D_2O moderator tank which achieves peak neutron flux 35 cm from the centre of the reactor core [67]. A water tank and concrete shield surround the core and moderator. Cooling is achieved by cycling D_2O through the fuel vanes and the reaction is controlled by a single central Boron control rod. This apparatus provides a spectrum of thermal neutrons with peak a peak flux of $1.5 \times 10^{15}\ \frac{n}{cm^2 s}$. In addition, multiple localized moderators in the D_2O moderator

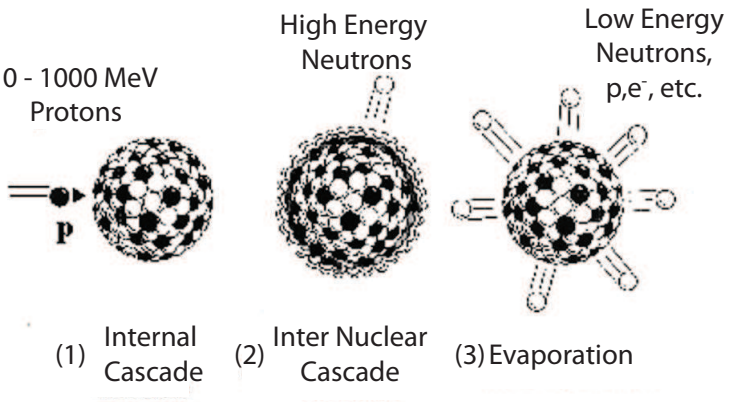

Figure 5.3: A schematic of the spallation process. The high energy proton first causes a rescattering of high energy neutrons, followed by a period of nuclear decay or 'evaporation', where the bulk of the neutrons are emitted at a lower energy along with photons, neutrinos and other nucleons [67].

tank provide peak neutron flux in the 200 meV (hot), 5 meV (cold) and 8×10^{-5} meV (ultracold) range. This reactor houses 16 beam tubes which provide neutrons to 40 instruments.

Spallation sources produce neutrons by bombarding a heavy metal target with high energy protons produced by an accelerator. Protons are accelerated to energies of 10 MeV to 1 Gev, and collided with targets of Uranium, Tantalum, Tungsten, Lead or Mercury. A schematic of the spallation process is shown in Figure 5.3. The proton collision produces a cascade of nucleons which ejects neutrons of similar energy and direction to the incident proton. Nuclei return to the unexcited state by 'evaporating' several lower energy neutrons, photons, neutrinos and other nucleons isotropically [67, 70]. The bulk of neutrons are produced by evaporation with energies of $\sim$2 MeV for 250 MeV protons [69]. This reaction produces 20 - 30 neutrons per proton collision and releases 3 times less energy than fission [67, 69]. Reactor sources produce a continuous flux of neutrons, however with spallation it is possible and advantageous to produce pulses of neutrons. Pulsed spallation sources may achieve higher instantenous neutron flux by decreasing the pulse length. Neutron background is also lower because the source is not producing neutrons the majority of the time [67, 70]. Thermal neutron fluxes up to 1×10^{17} $\frac{n}{cm^2 s}$ are produced by moderation

in H_2O baths at ambient temperatures placed in the path of the beam. Accelerated protons are aggregated in an accumulator ring to form tight bunches, which are released as pulses microseconds in duration [69]. Figure 5.4a shows the pulse geometry for the Spallation Neutron Source (SNS) at Oak Ridge National Labs in Oak Ridge Tennessee.

Neutron energies are determined by measuring their time of flight. An example instrument layout for a pulsed spallation source is shown in Figure 5.4. Energies are determined by selecting velocities with choppers (discussed below) based on known distances and travel times. The pulse frequency is limited such that pulses do not overlap to allow time of flight measurement. The pulse length defines the flux and initial energy distribution of the neutrons produced. The pulse frequency determines minimum neutron velocities. A ratio of pulse length to pulse periodicity of 2 - 3%, called the *duty cycle*, is preferred to balance pulse intensity and energy resolution [69].

The Spallation Neutron Source (SNS) operates at peak power of 1.4 MW. An overview of the facility is shown in Figure 5.5a. The SNS is the most intense neutron source in the world and provides a peak neutron flux of 1×10^{17} $\frac{n}{cm^2 s}$. Protons are created and accelerated from 2.5 MeV to 1 GeV in a linear accelerator. Accelerated protons are compressed by a factor of 1000 in an accumulator ring and released after 1200 turns for 1 μs pulses at a frequency of 60 Hz. This represents a duty cycle of 2%. The target is a liquid Mercury box surrounded on the top and bottom by ambient temperature H_2O and 20 K Hydrogen moderators which provide thermal and cold neutrons respectively (Figure 5.5b). The target operates between 60 and 90^o C at 2 MW beam power. Target Mercury flows convectively through the 70 $\times$ 200 mm proton beam spot to prevent overheating. This target currently provides neutrons for 12 beamlines and 14 instruments.

5.1.2 Neutron Instruments

The goal of neutron instrumentation is to precisely define the state (energy, momentum, spin, intensity, direction) of the incident neutron beam and to examine the resulting scattering pattern. Neutron velocities (energies) can be determined by measuring their wavelength (Bragg scattering), determining their time of flight or observ-

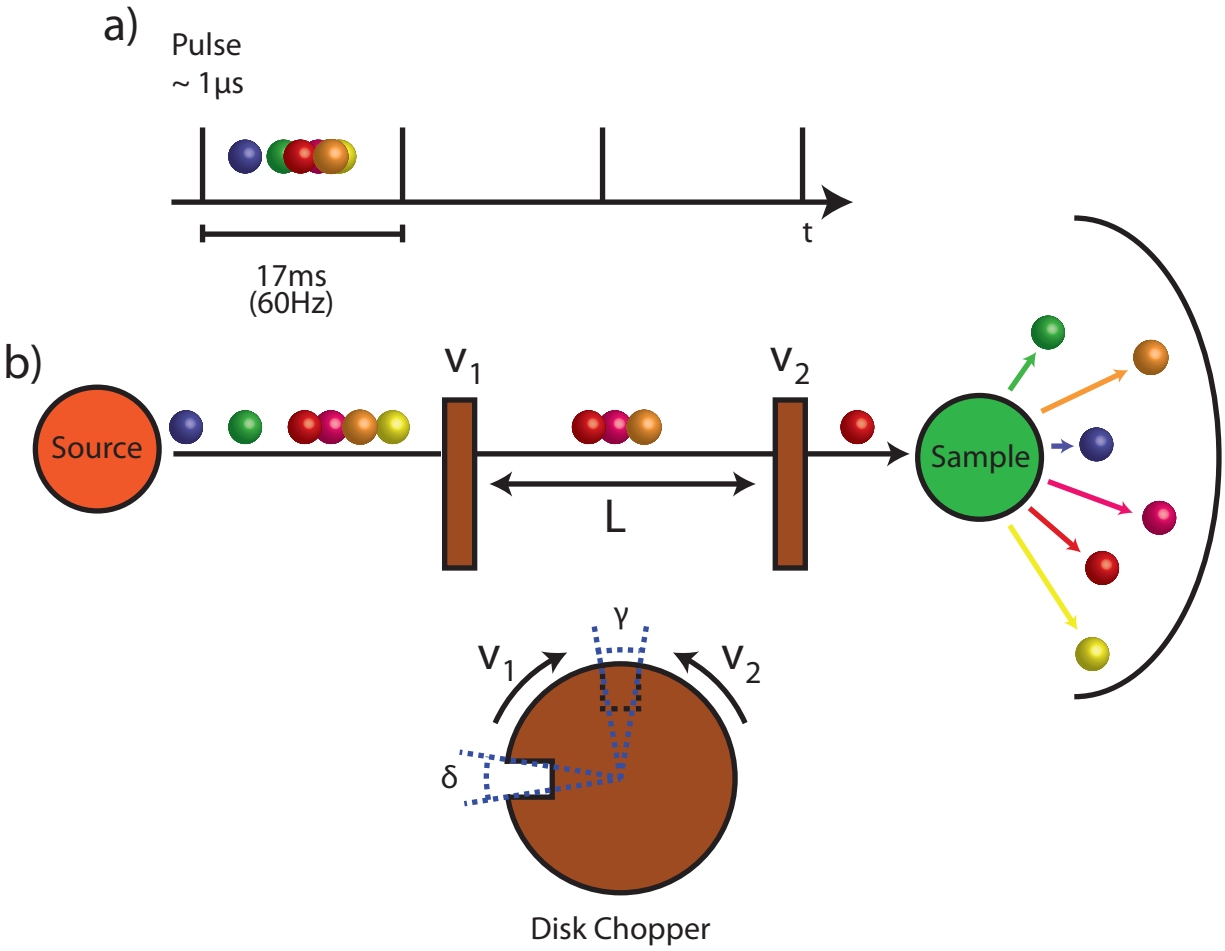

Figure 5.4: Spallation Neutron Source pulse geometry is shown in a). Different colours represent neutrons of different velocities. The SNS operates at a duty cycle of 2% with pulses of 1 μs every 1.7 ms. b) depicts a typical pulsed source instrument. Neutron energy is selected by disk choppers. By changing the velocity and relative phase of these choppers, the velocity of incoming neutrons can be precisely defined. The pulse width defined by a chopper depends on its angular aperture size δ and the aperture size of the beam opening γ.

a)

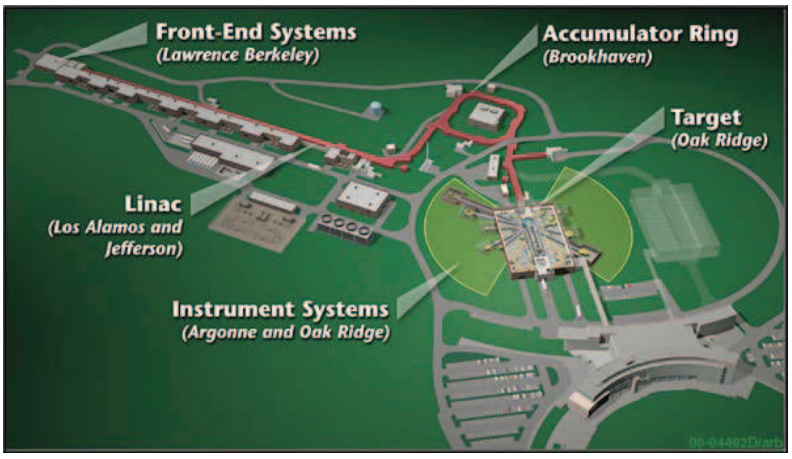

b)

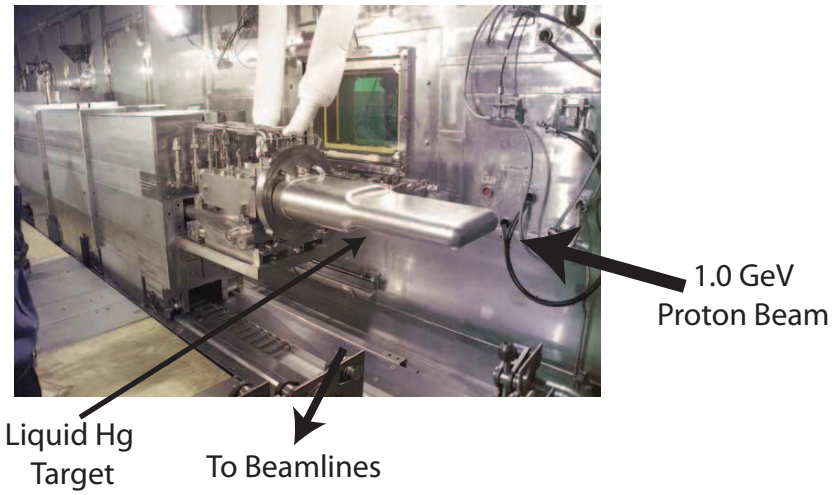

Figure 5.5: An overview of the Spallation Neutron Source facility is shown in a). b) depicts the liquid Mercury proton target. Images obtained from the Spallation Seutron Source website (http://neutrons.ornl.gov/facilities/SNS/works.shtml).

ing the precession of neutron spin in an external magnetic field. Neutron instruments such as backscattering spectrometers, spin echo spectrometers, reflectometers, time of flight spectrometers and triple axis spectrometers achieve this in different ways and as a result extract different information. Neutron optics such as monochromators, choppers and collimators are used to define beam characteristics.

Monochromators are single crystals or arrays of crystals with well defined lattice planes. Neutron wave properties dictate that reflections from a crystal lattice are defined by Bragg scattering (equation 4.3). By adjusting angle of incidence of the neutron beam, a particular wavelength (or energy) of neutrons may be selected. Ideal monochromator material must have a large scattering length density, low absorption and low incoherent and inelastic scattering cross sections. Crystals such as pyrolytic graphite, Silicon, Germanium or Copper with mosaicities between 0.3 and 0.5^o are preferred [67]. Mosaic crystals composed of arrays of smaller crystals may be arranged as shown in Figure 5.6 to form *focussing monocromators* which increase neutron flux on a smaller sample area. However the broader distribution of lattice spacings in mosaic crystal monochromators broadens the selected wavelength resolution and beam divergence. Mosaic crystals are also used to compensate for large incident beam divergence by broadening the distribution of possible reflection angles. The wavelength resolution of a crystal monochromator depends on the incoming and outgoing beam divergence α_0 and α_1 and monochromator mosaicity η_M according to equation 5.2.

$$\frac{\Delta\lambda}{\lambda} = \cot\theta_m \left(\frac{\alpha_0^2\eta_M^2 + \alpha_1^2\eta_M^2 + \alpha_0^2\alpha_1^2}{\alpha_0^2 + \alpha_1^2 + 4\eta_M^2} \right)^{1/2} \tag{5.2}$$

For a perfect single crystal ($\eta_M = 0$) reflecting a beam with 1^o incident divergence at $2\theta_m = 90^o$, a typical relative resolution of $\sim$1% is obtained [69]. Crystal monochromators based on Bragg scattering also reflect higher order wavelengths λ/n. These must be filtered out by using crystals such as pyrolytic graphite, which eliminates second order reflections for $\lambda = 1.53$ Å and 2.36 Å for thermal neutrons, or using filters such as polycrystalline Beryllium, which transmits only neutrons over 4 Å [67].

Monochromators are often complemented by collimators which define the direction and divergence of the neutron beam. To define the divergence of a beam in one dimension in a distance L, tubes divided by neutron absorbing blades (Cd or metal coated in Gd), called Soller collimators, are used. A Soller collimator is shown in

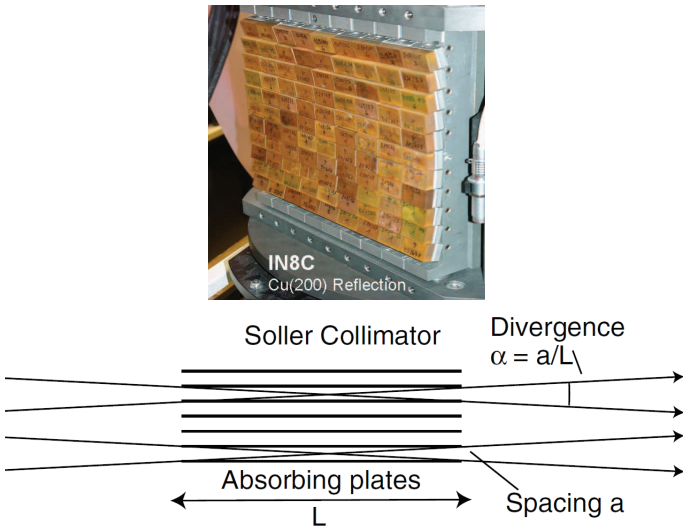

Figure 5.6: Vertically focussing monochromator and soller collimator schematic [69].

Figure 5.6. The length L and blade spacing a define the collimation divergence $\alpha = \frac{a}{L}$ of neutrons which are not absorbed. The collimation is measured in minutes (') which are defined as $\frac{1}{60}^{th}$ of a degree. Collimator transmission τ depends on the thickness t of the blades according to $\tau = \frac{a}{a+t}$, where a is the blade spacing. At a collimation of 10', 96% of this theoretical transmission can be obtained [67].

Choppers restrict neutron energy by time of flight. A simple disk chopper is shown in Figure 5.6b. Disk choppers consist of a disk with one or more slits which rotates with its axis parallel to the neutron beam. The chopper is made of, or coated in neutron absorbing material such that only neutrons passing through the chopper opening while it is lined up with the beam path may pass. Two choppers placed a distance L apart are used to define a wavelength band $\Delta\lambda$. For neutrons with $\lambda =$ 4 Å and chopper speeds up to 20 000 rpm, neutron energy can be determined in only a few meters. The first chopper defines a pulse with full width half maximum $\beta = \frac{\delta+\gamma}{2\omega}$, where δ is the angular opening in the chopper, γ is the angular opening in the beam path and ω is the chopper frequency. The second chopper (or *monochromating chopper*) is rotated in the opposite direction to the first to select a narrow velocity distribution. The relative wavelength resolution is defined by the pulse width and time of flight $t = \frac{m_n \lambda L}{h}$ as $\frac{\Delta\lambda}{\lambda} = \frac{\beta}{t}$, where h is Planck's constant. Multiple choppers are employed at pulsed sources to further define pulse shape and eliminate pulse

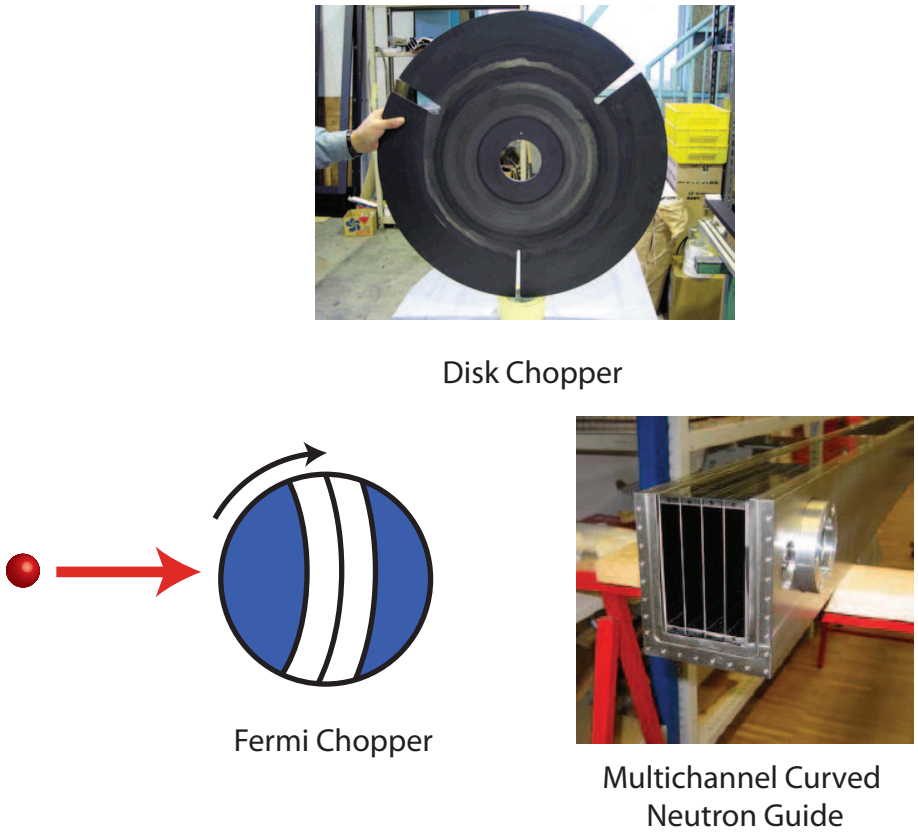

Figure 5.7: Disk Chopper, Fermi Chopper and Neutron Guide. Disk chopper image obtained from the Neutron Science Research Centre at the Tokai Research Establishment (http://www.jaea.go.jp/jaeri/english/ff/news62/rd1.html). The neutron guide shown was fabricated by Swiss Neutronics and is in use at the Institut Laue Langevin. Image obtained from Schott glass manufacturers (http://www.us.schott.com/advanced_optics/english/projects/neutron_science.html).

overlap. A Fermi chopper consists of a set of curved collimator blades which rotate with their long axis parallel to the beam path (see Figure 5.7). Fermi choppers simultaneously pulse and monochromate the neutron beam. Curved blades provide straight collimation from the point of view of the neutron [67].

Neutron guides transport neutron beams from the source to the instruments and also contribute to beam characteristics. Transporting neutron beams away from the source ensures lower backgrounds and allows neutron pulses to spread out, enhancing velocity selection. Neutron guides are rectangular tubes enclosed in Boron and coated with highly reflective material, such as Nickel. Reflectivities up to 99% are achieved

and guides are usually evacuated to elminate air scattering or absorption. Neutron guides are usually evacuated to avoid air scattering or absorption. Curved guides are employed to eliminate high energy neutrons and are often divided to decrease divergence and allow sharper curves without loss of flux [67]. A multichannel curved neutron guide is shown in Figure 5.7.

Two important neutron instrument types are triple axis and backscattering spectrometers. Triple axis spectrometers leverage the flexibility of the scattering triangle to measure the intensity of scattered neutrons with a particular energy and momentum transfer. A schematic of a triple axis spectrometer is shown in Figure 5.8a. Three rotatable axis are indicated in red. The initial neutron energy is selected by a monochromator in a rotatable shielded drum (axis 1). The incident angle of the beam on the monochromator defines the invident wavevector $\boldsymbol{k}_i$, and may be altered by rotating the monochromator and drum opening. The beam then interacts with the sample, which may rotate with the analyzer drum (axis 2) to define the scattering angle 2θ and $\boldsymbol{q}$. A final neutron energy is selected by the analyzer (another monochromating crystal) which may be rotated independently of its containing shielded drum (axis 3), before striking the detector. The angle of incidence of the beam on the analyzer defines the final wavevector $\boldsymbol{k}_f$. Horizontal beam divergence is described by Soller collimators present in the neutron guide, after the monochromator, after the sample and after the analyzer. Slits are also used to limit the beam to the sample and analyzer area and provide vertical collimation. Low efficiency ($\sim 10^{-5}$ - 10^{-4}) detectors called monitors are placed in the beam path to monitor monochromated and scattered neutron flux [67]. A schematic of a triple axis spectrometer in W-configuration is shown in Figure 5.8b.

Defining $\boldsymbol{k_i}$, $\boldsymbol{k_f}$ and $\boldsymbol{q}$ with the monochromator, analyzer and sample axis allows examination of one point in $(\boldsymbol{q}, \omega)$ space. Rotating the monochromator and analyzer with a constant scattering angle allows scanning through the intensity at different energies for a single $\boldsymbol{q}$ value. Constant $\boldsymbol{q}$ scans can also be performed with either $\boldsymbol{k}_i$ or $\boldsymbol{k}_f$ fixed and varying the scattering angle. Rotating the monochromator and analyzer such that the magnitude of $\boldsymbol{k_i}$ and $\boldsymbol{k_f}$ are constant changes the scattering angle and scans through $\boldsymbol{q}$ values at a constant energy. The resolution of the instrument in both $\boldsymbol{q}$ and ω depends on the collimation and the mosaicity of the monochromator

and analyzer crystals. Horizontal beam divergences between 0.5 - 2 degrees typically lead to a relative $\boldsymbol{q}$ resolution of $\sim$1% and energy resolutions of 5-10% for thermal neutrons [67]. The resolution is flux limited because for a given neutron source, there will be less neutrons in a smaller λ range. Excitations with energies from 50μeV to 200 meV may be examined using a triple axis spectrometer depending on the energy range (cold, thermal, hot) of the neutron source. The accessible $\boldsymbol{q}$ and energy range of triple axis spectrometers are limited by physical rotation constraints and momentum conservation (closing the scattering triangle). Triple axis spectrometers are also limited because they can only examine one point in $(\boldsymbol{q}, \omega)$ space at a time, which is excellent for precise measurements of excitations at known $(\boldsymbol{q}, \omega)$ values, but is limiting for new discoveries.

A schematic of the IN12 cold triple axis spectrometer at the High Flux Reactor of the Institut Laue-Langevin is shown in Figure 5.8a. A summary of instrumental characteristics is shown in Table 5.2. Situated 108 metres from the reactor core, IN12 provides a 12 $\times$ 3 cm^2 cold neutron beam with low background. IN12 employs an adjustable 12 $\times$ 8 cm^2 vertically focussing pyrolytic graphite (002) monochromator with lattice spacing 3.355 Å which can produce energies between between 2.3 and 14 meV. A nitrogen cooled Berylium filter 10 cm long is used to filter higher order monochromator reflections. Maximum neutron flux is 1.0 $\times$ 10^7 $\frac{n}{cm^2 s}$ for energies of 4 meV and 60' collimation. An adjustable horizontally focussing 12.2 $\times$ 11.8 cm^2 pyrolytic graphite (002) analyzer allows energy resolutions up to 22 μeV at 2.3 meV and 30' collimation. Gadolinium coated Soller collimators of 10 - 60' can be placed after the monochromator, sample and analyzer. Accessible monochromator angles are between 7.5^o and 45^o and sample and analyzer may rotate through ranges of 120^o and 140^o respectively.

Backscattering spectrometers are another type of neutron scattering instrument which attempts to maximize energy resolution. As mentioned above, the difficulty in achieving maximum resolution is that it typically involves discarding neutrons outside the desired energy range, which results in a loss of flux. Backscattering spectrometers de-couple the resolution from the flux by taking advantage of the dependence of monochromator $\Delta\lambda$ on the angle of incidence θ_m. As θ_m approaches 90^o, taylor expansion of equation 5.2 demonstrates that the wavelength depends on the incident

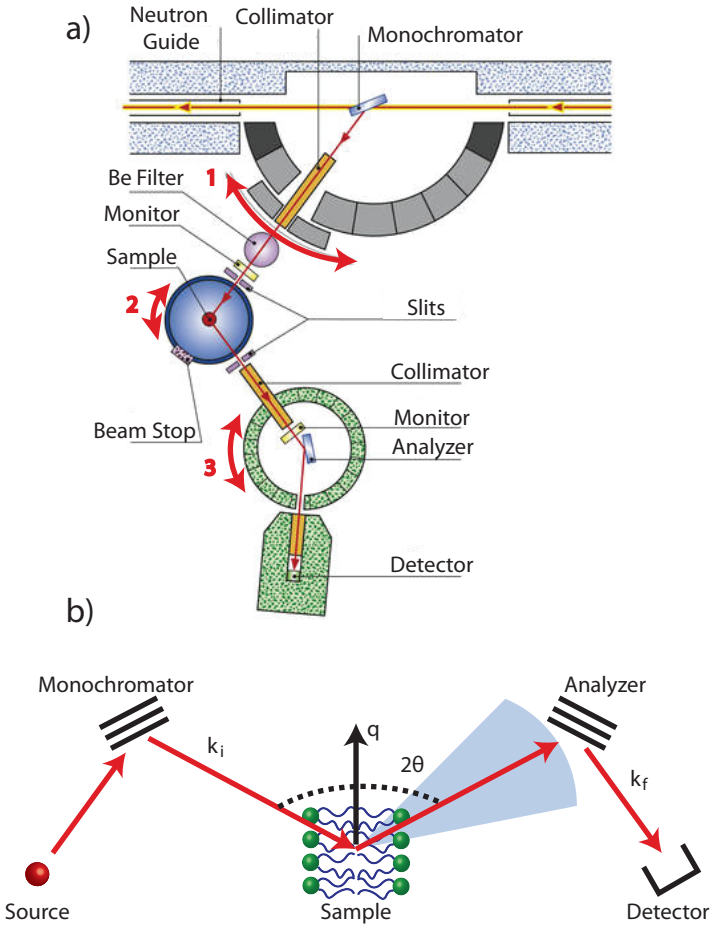

Figure 5.8: a) A schematic of the IN12 cold triple axis spectrometer. b) A generalized triple axis spectrometer in W-configuration.

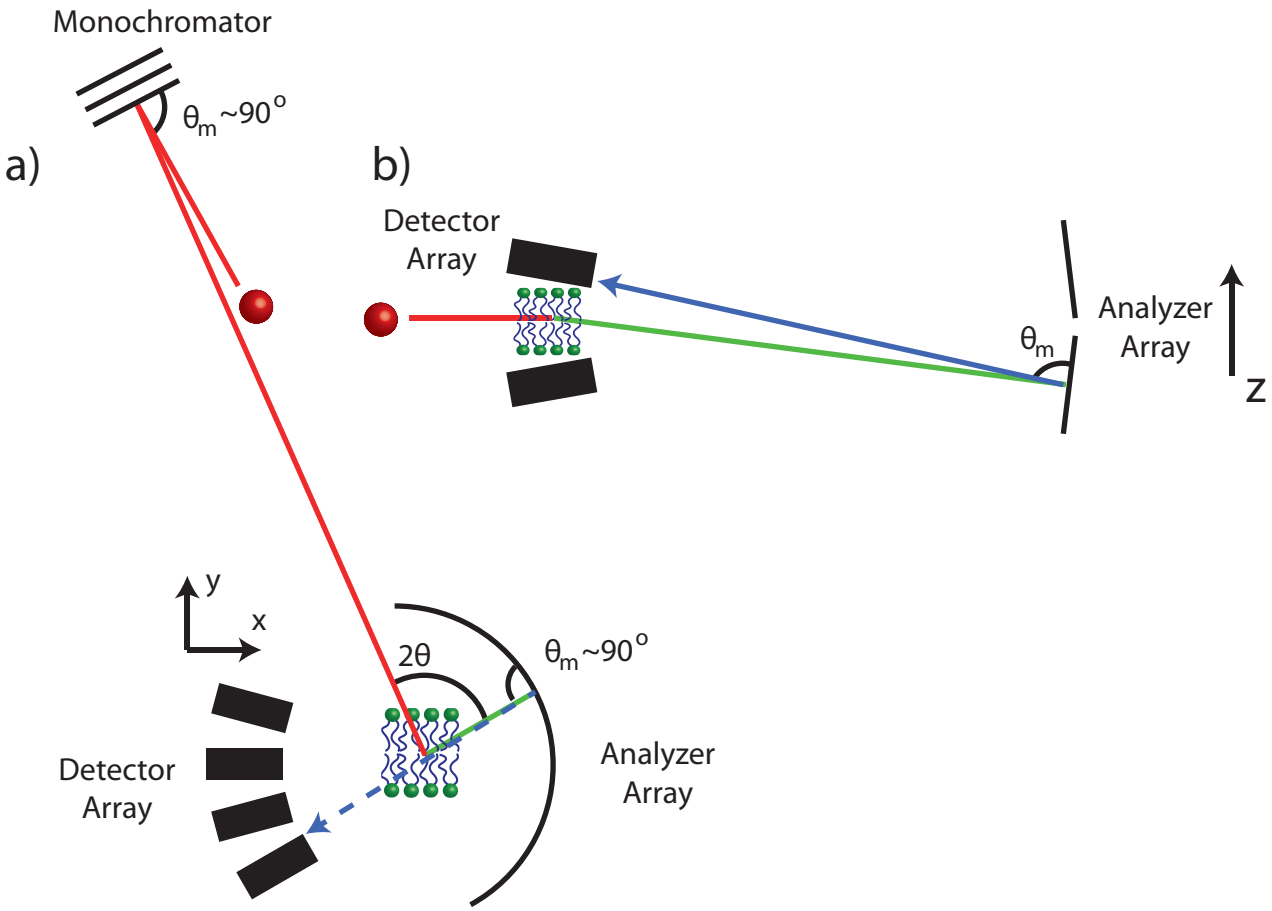

Figure 5.9: A schematic of an ideal backscattering apparatus. a) The horizontal plane is shown. The neutron beam is monochromated, scatters from the sample, and is reflected by an array of analyzers to detectors arranged slightly above and below the sample. The vertical plane is shown in b). θ_m should be nearly 90^o.

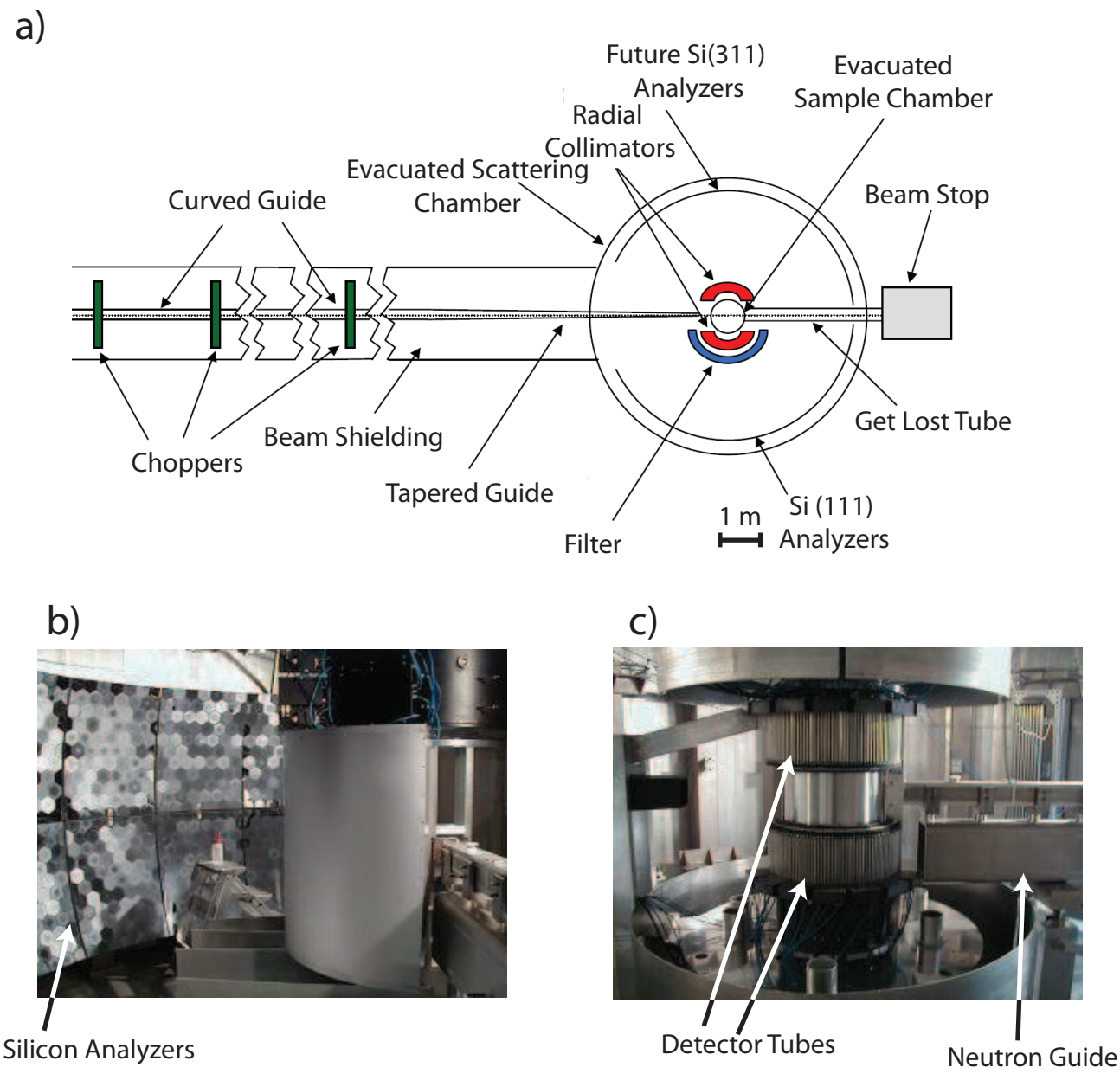

Figure 5.10: A schematic of the backscattering spectrometer at the Spallation Neutron Source (BASIS). In a), the beam enters on the left through a series of choppers which tune the incoming wavelength. The beam is then scattered by the sample passed through radial collimators, and reflected by Silicon (111) analyzers to detectors above and below the incident beam. b) Shows the setup inside the evacuated detection drum. c) and d) show the crystal analyzer array and detector tubes inside the evacuated drum. Images obtained from the instrument website (http://neutrons.ornl.gov/instruments/SNS/BASIS/).

IN12 Triple Axis Spectrometer Characteristics	
Neutron Source	Reactor
Energy range	2.3 - 14 meV
λ range	2.3 - 6.0 Å
Peak Flux	$1.0 \times 10^7 \frac{n}{cm^2 s}$
Maximum Energy Resolution	22 μeV
Monochromator	Pyrolytic Graphite (002)
Analyzer	Pyrolytic Graphite (002)

Table 5.2: IN12 instrument characteristics. Peak flux is measured at 4 meV with 60' collimation. Maximum energy resolution occurs at an incident energy of 2.3 meV.

beam divergence to the second order. The λ resolution of a monochromator will therefore be maximum in the case of backscattering: where $\theta_m = 90^o$ and $\cot\theta_m$ approaches zero [71]. By employing backscattering on both the incident and scattered beams with perfect Si (111) monochromators, energy resolutions up to 0.3 μeV can be achieved [71]. A schematic of an ideal backscattering spectrometer is shown in figure 5.9. The incident neutron energy is selected in backscattering geometry, which then interacts with the sample. The scattered neutrons (green) are reflected (blue) back from an array of focused analyzers onto a nearby array of detectors. For a pulsed source, incident energy is defined by choppers acting over a long neutron guide. Longer guides allow increased pulse spreading which increases chopper wavelength resolution. A high-speed chopper close to the moderator is often used to sharpen the source pulse to further increase resolution [71]. Backscattering geometry is ideal for elastic scattering, but inelastic examinations are restricted by the backscattering condition. Fixed analyzers, providing a fixed $\boldsymbol{k}_f$, means $\boldsymbol{k}_i$ must be modulated to change the observed energy transfer. For a pulsed source this is achieved by adjusting the wavelength selected by the choppers, which can provide energy transfers of up to $\pm 120\mu$eV. Continuous source backscattering instruments which use a monochromator to define $\boldsymbol{k}_i$ rely on neutron Doppler shifting from moving monochromators or thermally expanding crystals such as CaF_2 [71]. Energy transfers of $\sim$30 μeV are possible with Doppler velocities of 5 m/s, where thermal expansion of CaF_2 from 77 to 700 K provides only a $\sim$3% relative energy change [69]. The high energy resolution of backscattering spectrometers is ideal for examining low energy signals corresponding to slow nano-picosecond dynamics.

A schematic of the backscattering spectrometer at the Spallation Neutron Source (BASIS) is shown in Figure 5.10 and uses backscattering geometry only for the analyzers. A summary of BASIS parameters is shown in Table 5.3. A 60 μs pulse and three choppers operating at 60 Hz define the incident beam wavelength as 6.4 Å over an 84 m 10 $\times$ 12 cm^2 neutron guide. The neutron guide illuminates a solid angle of 1.2 steradians in a 5 m diameter evacuated drum which houses the sample chamber, Si (111) analyzers and detectors. An array of 2 mm thick hexagonal Silicon crystals with lattice spacing 3.14 Å are arranged in a spherical pattern to span 180^o around the sample chamber and reflect neutrons at $\theta_m = 87.93^o$ to detectors placed above and below the incident beam path (see Figure 5.10c and d). Radial horizontal collimators surround the sample chamber to ensure near backscattering. The detector and analyzer array provides a two dimensional intensity map between $\boldsymbol{q}_{||}$ = 0.6 - 2.0 Å^{-1} and $\boldsymbol{q}_z$ = -0.67 - 0.67. The elastic energy defined by the analyzer array is 2.08 meV with a resolution of 3 μeV. The sample chamber is a 1 m diameter hole in the centre of the evacuated detector drum. The sample can placed in the sample chamber may be evacuated by an external vacuum pump and its temperature controlled by a cryostat within a tolerance of 1.0 K. The energetic range available is $\pm$120 μeV, however asymmetrical background effects limited the usable range to $\pm$80 μeV. Chopper frequency, incident wavelength and sample temperature are controlled from a computer system on top of the detector drum. Intensity data is collected in binary format and reduced to two dimensional $\boldsymbol{q}$ maps by a central server. Intensity maps may be filtered by applying custom masks which eliminate unwanted or background data. Data may then be divided by $\boldsymbol{q}$ and preliminary data analysis may performed at the instrument with Data Analysis and Visualization Environment (DAVE) software.

5.2 X-ray instrumentation

5.2.1 X-ray generation

X-rays are produced by converting electron kinetic energy into electromagnetic radiation. Electrons are accelerated to velocities nearly 50% the speed of light and collided with a metal target such as Copper, Tungsten, Iron, Cobalt, Molybdenum or Silver [72]. Electrons with energies from 1 - 100 keV are obtained by applying a

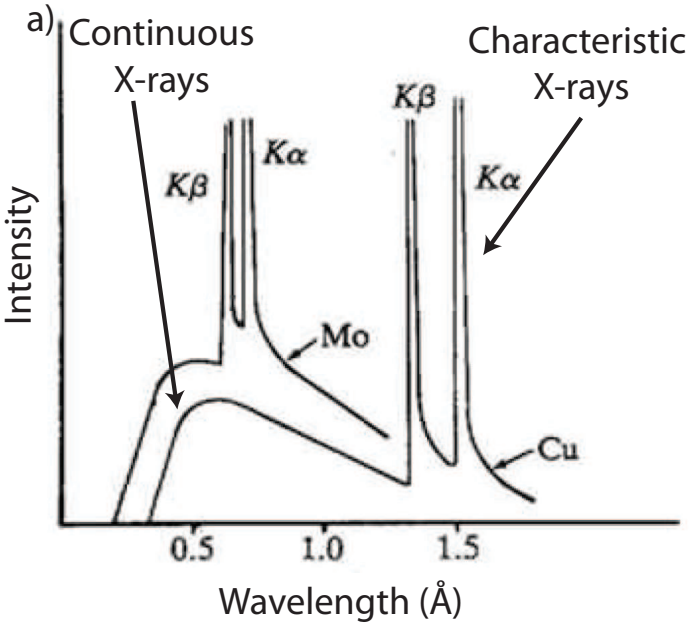

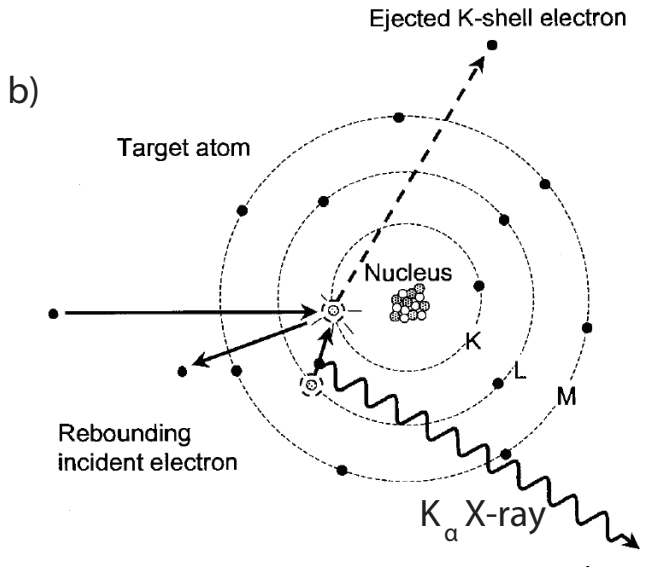

Figure 5.11: a) The x-ray spectrum produced by electronic collision with a copper and molybdenum target. Intensities are not to scale [72]. b) The production of characteristic x-rays. An incident electron knocks a target electron out of its orbital, higher energy electrons decay to take its place and emit an x-ray photon in the process [73].

BASIS Backscattering Spectrometer Characteristics	
Neutron source	Pulsed Spallation
Elastic energy	2.08 meV
Energy range	$\pm$120 μeV
Q range	0.6 to 2.0 Å^{-1}
Maximum Energy Resolution	3 μeV
Chopper Speed	60 Hz
Analyzer	Si (111)
Bragg angle	87.93

Table 5.3: BASIS backscattering spectrometer characteristics.

voltage across an evacuated tube containing a positively charged target anode and negatively charged cathode. The cathode consists of a heated tungsten wire or coil which produces electrons by thermionic emission. Electron current measured in mA (1 mA = 6.24×10^{15} electrons/second) is limited by the heat produced upon collision with the target which may cause target damage. For a Tungsten target and 100 keV electrons, the only $\sim$1% of electron kinetic energy is converted to x-rays [73]. A rotating disk anode, which spreads electron thermal energy over the larger area and mass of the anode disk is often employed to achieve higher electron current. Interactions with the target nuclei and electron cloud produce photons with wavelengths $\sim 10^{-10}$ m corresponding to x-rays. The spectrum of x-rays produced by Molybdenum and Copper is shown in Figure 5.11a and exhibits a continuous and characteristic region. Braking radiation (bremsstrahlung) x-rays are produced by rare ($\sim$0.5%) interactions with the nucleus, and exhibit a continuous low intensity distribution focussed at high energies. Characteristic x-rays are produced when incident electrons eject target electrons from an atomic orbital. As a result, higher orbital electrons decay, emitting x-ray photons exhibiting distinct energies defined by the electron energy loss as shown in Figure 5.11b [72]. High incident electron energies are required to ensure target electrons are ejected. The two primary peaks of characteristic x-rays are the K_α and K_β lines, which indicate that the electron decayed to the K shell from an adjacent (L), and non-adjacent orbital respectively. The wavelength of K_α and K_β lines fall between 0.2 and 2.0 Å and depend on the target material. Modern x-ray instruments employ only one characteristic x-ray line (usually K_α) and others are filtered out with sub-millimetre thin metal sheets (lead, rhodium, nickel are good

K_β filters) or by monochromating the beam. Two distinct peaks K_{α_1} and K_{α_2} are present in the K_α band at very similar energies. Improved x-ray energy resolution can be achieved by selecting only K_{α_1} using Germanium or Silicon monochromators or a focussing multilayer mirror.

5.2.2 Biological Large Angle Diffraction Experiment

The Biological Large Angle Diffraction Experiment (BLADE) is the Rigaku Smartlab Automated Multi-Purpose x-ray diffractometer at the McMaster Laboratory for Membrane and Protein Dynamics. Simple x-ray diffractometers consist of an x-ray source, a monochromator, a series of slits for collimation, a sample stage and a detector. The initial and final wavevectors are defined both by the selected wavelength and the incident ($\boldsymbol{k}_i$) and scattered ($\boldsymbol{k}_f$) angles with respect to the sample. The detector measures the elastic scattered intensity of the sample at the lengthscale defined by these wavevectors. BLADE provides a high intensity beam, with adjustable resolution and adjustable wavevectors by means of rotating source and detector arms. A picture of BLADE is shown in Figure 5.12, and a summary of instrumental characteristics is given in Table 5.4. X-rays are generated by a water cooled 9 kW rotating copper anode with maximum voltage of 45 kV. A maximum electron current of 200 mA produces x-ray intensities up to 10^{10} counts per second. The copper target produces K_{α_1}, K_{α_2} and K_β x-rays at wavelengths of 1.544, 1.541 and 1.392 Å respectively. For examining thin films, the K_{α_1} wavelength is selected by a monochromating multilayer mirror. A series of swappable 2, 5 or 10 mm height limiting slits and 0.5 - 15 mm width limiting slits allow adjustment for sample sizes and $\boldsymbol{q}$ resolution (see Figure 5.12b). Soller collimators with horizontal divergence 0.15, 0.5, 1.0, 2.5 and 5^o may also be placed in the beam path before and after the sample. The sample stage shown in Figure 5.12c may rotate up to 95^o in the vertically and 720^o horizontally. Sample alignment can be performed automatically by specifying sample dimensions and measuring the scattering profile at different orientations. The x-ray hydration chamber (without cover) is shown mounted on the sample stage in Figure 5.12c. Sample temperature is controlled through a water bath pumped directly under the hydration chamber. The detector arm may rotate in the plane (θ) of the sample stage with variable resolution, providing a $\boldsymbol{q}_{||}$ range of -0.3 to 3 $Å^{-1}$. The source (θ_s) and detector (θ_d) arms may

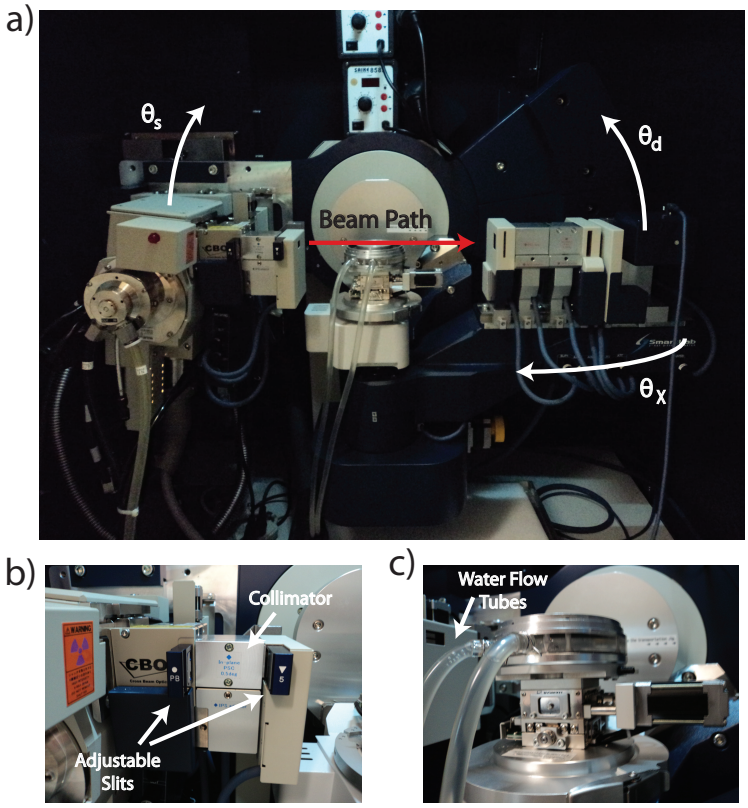

Figure 5.12: The entire instrument is shown in a). The detector arm may rotate both parallel and perpendicular to the sample stage, and the source arm may rotate perpendicularly. The incident optics are shown in b). The sample stage and water flow tubes are shown in c).

rotate perpendicular to the sample plane to provide a $\boldsymbol{q}_z$ range from 0 to 1.4 Å^{-1}. Raster scanning the detector arm through θ_χ and θ_d maps the scattered intensity in the two dimensional $\boldsymbol{q}$ range, producing a *2D in-plane scan*. BLADE produces 2D in-plane scans with 0.02 Å^{-1} $\boldsymbol{q}_z$ resolution in ∼18 hours. Sample perpendicular structure may be explored by moving the detector arm through θ_d to perform reflectivity. Collimation and slits in the beam path after the sample limit the scattered $\boldsymbol{q}$ resolution. However the lack of monochromator for precise scattered energy selection results in signal averaging over both elastically and inelastically scattered x-rays.

BLADE Characteristics	
Source	9 kW Rotating Anode
Maximum Voltage	45 kV
Maximum Current	200 mA
Wavelength	1.544 Å
$\boldsymbol{q}_{\|\|}$ range	-0.3 - 3.0 Å^{-1}
$\boldsymbol{q}_z$ range	0 - 1.4 Å^{-1}

Table 5.4: BLADE x-ray diffractometer characteristics.

Chapter 6

Paper I: Diffusion in Single Supported Lipid Bilayers Studied by Quasi-Elastic Neutron Scattering

Clare L. Armstrong, Martin D. Kaye, Michaela Zamponi, Eugene Mamontov, Madhusudan Tyagi, Timothy Jenkins and Maikel C. Rheinstädter *Diffusion in single supported lipid bilayers studied by quasi-elastic neutron scattering*, Soft Matter, **6**, 5864-5867, 2010

Preface to Paper I

In this study lipid diffusion in single solid supported bilayers was investigated with quasi-elastic neutron scattering. The study of single solid supported bilayer dynamics with neutron scattering has previously been limited by minute sample masses and insufficient neutron flux. In this paper, state of the art backscattering neutron scattering techniques were able to access nanometre length scales and pico to nanosecond timescales required to examine diffusive lipid motions for the first time. Diffusion coefficients for single bilayer systems were found to be comparable to those found for multilamellar bilayer systems with macroscopic techniques. However the nature of the observed lipid diffusion was continuous where multilamellar systems observe a flow-like ballistic motion. An enhanced diffusion was also observed over lengthscales near the lipid nearest neighbour distance. This enhanced diffusion was attributed to the highly ordered bilayer fluid phase which resulted from confinement of the bilayer to the substrate.

I was the second author on this paper. This involved learning how to prepare single solid supported bilayers, controlling and collecting data from a backscattering spectrometer and performing preliminary on-site data analysis. Sample preparation was performed by Dr. Maikel Rheinstädter, Clare Armstrong and myself. During the experiment, I was responsible for controlling the instrument and collecting the resulting data. Data produced was fit with DAVE analysis software after each scan to determine the optimum use of beamtime. I was also involved in discussions of the final data analysis to a lesser degree. Clare Armstrong was the primary investigator for this paper and she contributed to the sample preparation, instrumental control and performed the final data analysis. Dr. Maikel Rheinstädter also contributed to all aspects of this paper.

View Online

Diffusion in single supported lipid bilayers studied by quasi-elastic neutron scattering†

Clare L. Armstrong,*[a] Martin D. Kaye,[a] Michaela Zamponi,[bc] Eugene Mamontov,[b] Madhusudan Tyagi,[d] Timothy Jenkins[d] and Maikel C. Rheinstädter[ae]

Received 6th July 2010, Accepted 17th September 2010
DOI: 10.1039/c0sm00637h

Published on 12 October 2010 on http://pubs.rsc.org | doi:10.1039/C0SM00637H
Downloaded by McMaster University on 20 June 2011

It seems to be increasingly accepted that the diversity and composition of lipids play an important role in the function of biological membranes. A prime example of this is the case of lipid rafts; regions enriched with certain types of lipids which are speculated to be relevant to the proper functioning of membrane embedded proteins. Although the dynamics of membrane systems have been studied for decades, the microscopic dynamics of lipid molecules, even in simple model systems, is still an active topic of debate. Neutron scattering has proven to be an important tool for accessing the relevant nanometre length scale and nano to picosecond time scales, thus providing complimentary information to macroscopic techniques. Despite their potential relevance for the development of functionalized surfaces and biosensors, the study of single supported membranes using neutron scattering poses the challenge of obtaining relevant dynamic information from a sample with minimal material. Using state of the art neutron instrumentation we were, for the first time, able to model lipid diffusion in single supported lipid bilayers. We find that the diffusion coefficient for the single bilayer system is comparable to the multi-lamellar lipid system. More importantly, the molecular mechanism for lipid motion in the single bilayer was found to be a continuous diffusion, rather than the flow-like ballistic motion reported in the stacked membrane system. We observed an enhanced diffusion at the nearest neighbour distance of the lipid molecules. The enhancement and change of character of the diffusion can most likely be attributed to the effect the supporting substrate has on the lipid organization.

Although phospholipid membranes have been studied for decades[1] there is still no consistent picture of lipid dynamics, even in simple model systems. While techniques such as fluorescence recovery after photobleaching (FRAP) and fluorescence correlation spectroscopy (FCS) are capable of measuring the diffusion of lipid molecules on micrometre length scales, quasi-elastic neutron scattering (QENS) has proven to be an important tool to study nanoscale dynamics and diffusion on a nanometre length scale. In their seminal 1989 paper, Pfeiffer *et al.*[2] studied the local dynamics of lipid molecules in stacked fluid lipid membranes using incoherent neutron scattering techniques. Here a detailed model of lipid dynamics, including rotations, librations and diffusion, was proposed. More recently, this topic was revisited by Busch *et al.*[3] using state of the art neutron scattering techniques. Their primary finding was that the molecular mechanism for long range lipid diffusion in stacked membranes is a flow-like motion rather than the traditional diffusive motion. Ballistic motion was speculated to be a more efficient search strategy as compared to a Brownian motion.[4,5]

Despite their potential relevance to bioengineering applications, such as biosensors and surface functionalization[6,7] dynamical neutron scattering experiments in single supported bilayers have been limited in the past, as the minimal amount of sample material in a single bilayer results in a low scattering signal. Recent developments in neutron scattering instruments, and increasingly powerful neutron sources, now make it possible to observe dynamics in single bilayers. How the interaction between membrane and substrate affects lipid organization and dynamics, as compared to multi-lamellar or free-standing membranes, is a fundamental question.

We have studied the nanosecond lipid diffusion in a single phospholipid bilayer supported on a silicon wafer. From quasi-elastic neutron scattering, acquired using a backscattering spectrometer, the mechanism of the lipid diffusive motion could be modeled. While flow-like motion was reported in stacked bilayer systems,[3] we find evidence for a continuous diffusion with an enhanced diffusion at the nearest neighbor distance.

Single-supported bilayers of the model system 1,2-dimyristoyl-sn-*glycero*-3-phoshatidylcholine (DMPC) were prepared by vesicle fusion and hydrated by heavy water (D_2O).[8] 100 double-side polished, 2″, 300 μm thick, Si(100)-wafers were cleaned by immersion in an $H_2O_2^+$ sulfuric acid mixture (volume fraction of 70%

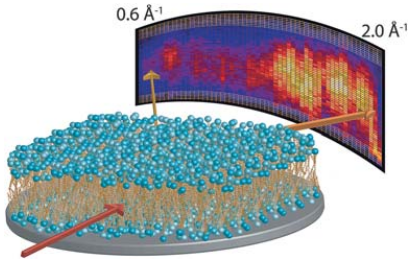

Fig. 1 A sketch of the experimental setup. Each solid supported single bilayer is aligned such that the plane of the membrane is in the scattering plane. In-plane q between 0.6 and 2.0 Å^{-1} are then measured simultaneously.

[a]*Department of Physics and Astronomy, McMaster University, Hamilton, ON, Canada. E-mail: armstc5@mcmaster.ca; Fax: (+905) 546-1252; Tel: (+905)525-9140 x26376*
[b]*Spallation Neutron Source, ORNL, Oak Ridge, TN, USA*
[c]*Jülich Center for Neutron Science, FZ Jülich, Jülich, Germany*
[d]*NIST Center for Neutron Research, NIST, Gaithersburg, MD, USA*
[e]*Canadian Neutron Beam Center, NRC, Chalk River, ON, Canada*
† Electronic supplementary information (ESI) available: Details regarding the data analysis. See DOI: 10.1039/c0sm00637h

 This journal is © The Royal Society of Chemistry 2010

View Online

Published on 12 October 2010 on http://pubs.rsc.org | doi:10.1039/C0SM00637H
Downloaded by McMaster University on 20 June 2011

concentrated H_2SO_4, 30%H_2O_2 at 90 °C for 30 min). This strongly oxidizing combination removes all organic contaminants on the surface, but does not disturb the native silicon oxide layer. The wafers were then rinsed and stored under distilled water before use. 200 ml of a 5×10^{-3} mol L^{-1} Hepes, 5×10^{-3} mol L^{-1} $MgCl_2$, and 100×10^{-3} mol L^{-1} KCl buffer solution was prepared and heated to 55 °C. DMPC was added to the buffer solution up to a concentration of 1.5 mg ml^{-1}. The milky solution, which initially contained giant multi-lamellar vesicles, was sonicated (50% duty cycle, power level 4) for 15 h until the solution became transparent and small uni-lamellar vesicles formed. The hydrophilic Si wafers were then completely immersed in the solution for 1 h. The lipid solution was kept at 55 °C during the whole process to keep the bilayers in their fluid phase. After 1 h the wafers were thoroughly rinsed with ~2 L of distilled water to remove excess vesicles from the surface. Through this procedure, small bilayer patches initially develop on the substrate, which eventually undergo a transition into a large uniform single bilayer after approximately 20–25 min.[8] The substrates were then annealed for 72 h at 55 °C in an oven in air before mounting in an aluminium sample can, and rehydrated.

Because the sample was hydrated with D_2O, the incoherent neutron scattering experiment is sensitive to local dynamics of the (protonated) lipid molecules. About 75% of the scattering comes from hydrogen atoms attached to the lipid acyl chains in the hydrophobic membrane core, and about 25% from hydrogen atoms located in the head group region. To increase the scattering signal, 100 wafers (resulting in 200 single bilayers) were mounted horizontally into the spectrometer, such that the neutron beam was always in the plane of the membrane ($q_{\|}$). In contrast to previous studies, this type of sample orientation probes $q_{\|}$ values between 0.6 and 2.0 $Å^{-1}$ simultaneously, corresponding to lateral length scales of 3 Å to 10 Å. The experimental setup is shown in Fig. 1. The sample was sealed in an aluminium sample can and placed inside a closed-cycle refrigerator (CCR) during the experiment. A sufficient amount of D_2O was added before closing to ensure full hydration of the bilayers (26 water molecules per lipid molecule), approximately 100 μL.

Elastic incoherent neutron scattering experiments were carried out using the high flux neutron backscattering spectrometer HFBS at the NIST Center for Neutron Research (NCNR), Gaithersburg, in its standard setup with Si (111) monochromator and analyzer crystals corresponding to an incident and analyzed neutron energy of 2.08 meV ($\lambda = 6.27$ Å). At the ~0.8 μeV resolution used, only hydrogen movements with characteristic times slower than 1 ns are monitored. The hydrogen atoms reflect the movements of larger groups to which they are attached, such as lipid head groups and carbon tails. Freezing and melting of molecular degrees of freedom can easily be identified, as they lead to jumps or kinks in the recorded intensity. Because the elastic intensity is related to the molecular mean-square thermal fluctuations $\langle \delta u^2 \rangle$, $S_{inc}^{el}(Q) \propto \exp\left(-\left\langle \frac{\delta u^2(T)}{6} \right\rangle Q^2 \right)$, each point on an elastic scan provides a value for the mean-square displacement (MSD) at a particular temperature.[9] The MSD was calculated and is shown in Fig. 2 over a temperature range of 240–355 K. Data were taken while heating the sample at a rate of 0.08 K min^{-1}. The inset in Fig. 2 depicts a sketch of a hydrated single supported bilayer as suggested by Nováková *et al.* from X-ray reflectivity. Each lipid molecule was found to be associated with 26 water molecules. Eight water molecules per lipid were found to be located within the head group region, while 18 water molecules per lipid form a hydration layer on the surface of the bilayer. There was also evidence of the presence of water molecules between the substrate and the lower leaflet.[10]

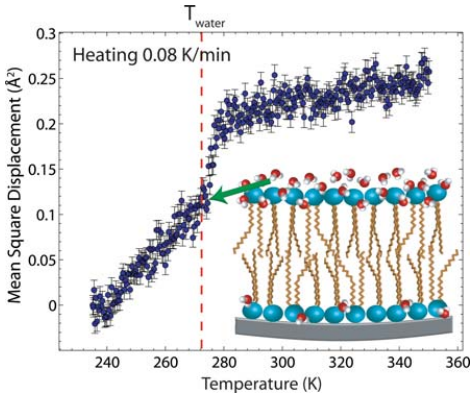

Fig. 2 The MSD of the lipid molecules over a temperature range of 240 to 355 K. The error bars shown are the result of statistical uncertainty. Melting of the hydration water was observed at approximately 273 K. No additional phase transition was observed at higher temperatures.

A melting transition at about $T_{water} = 273$ K was observed (see Fig. 2), which can most likely be assigned to the melting of the membrane hydration water. In multi-lamellar DMPC systems the transition from the gel into the fluid phase occurs at $T_m = 23.4$ °C = 296.6 K in fully hydrated bilayers and appears as a pronounced step in the MSD.[11,12] No such transition was observed. It was reported that the transition temperature may shift up to 318 K for nanometre sized patches of single supported bilayers.[13,14] The transition from the gel into the fluid phase involves a drastic increase in volume and area of the lipid molecules. For patches, the volume and area difference of the lipid molecules between the two phases can most likely relax over defects in the bilayer coverage.[13] In our samples, the transition was possibly suppressed due to large uniform and defect free single bilayers. While we cannot exclude the possibility that the upper and lower leaflets have different transition temperatures, the technique used should be sensitive enough to detect a transition in the individual leaflets. The diffusion constant that we determined is an order of magnitude faster than diffusion reported in the gel phase of multi-lamellar systems[2] and corresponds well with the diffusion constants reported in fluid multi-lamellar membranes, as discussed below. At 303 K, the single DMPC bilayers can, therefore, tentatively be characterized to be in a fluid state with an enhanced structural order; however, further structural investigations are required to unambiguously determine the structural state of the bilayer.

To measure the slow nanosecond dynamics, μeV energy resolved spectra were measured on the BASIS backscattering spectrometer at the Spallation Neutron Source, at Oak Ridge National Laboratory. The experiments were performed using a 60 Hz chopper setting with the incident wavelength bandwidth centered at of 6.4 Å. The Si (111) crystal analyzers provide an energy resolution of ~3 μeV, FWHM of the elastic peak, and a Q-range of 0.6 to 2.0 $Å^{-1}$. The dynamic range used was −80 to 80 μeV. Typical counting times were ~24 h.

Different diffusion models have been proposed. For a continuous diffusion, the quasi-elastic broadening is described by a Lorentzian

peak shape, with a full width at half maximum (FWHM) that shows a $q_{\|}^2$ dependence,

$$FWHM_L(q_{\|}) = 2\hbar D q_{\|}^2 \quad (1)$$

where D is the diffusion constant.[15]

A flow motion, as suggested in ref. 3,4 is described by a Gaussian component, where the width of the function has a linear $q_{\|}$ dependence,

$$FWHM_G\left(q_{\|}\right) = 2\sqrt{2ln(2)}\hbar v_o q_{\|}. \quad (2)$$

Here v_o refers to the ballistic velocity of the lipid molecules. In an unconstrained motion, v_o would correspond to the thermal velocity, $\sqrt{2k_BT/m}$.

Fig. 3 (a) and (b) depict exemplary spectra at $q_{\|} = 0.9$ and 1.3 Å^{-1}. The total scattering can be described by a narrow central component due to instrumental resolution and a quasi-elastic broadening between ~1–24 μeV. There is also evidence for a smaller broad component, similar to what has been observed by Busch *et al.* This broad component, most likely due to vibrations and librations of the lipid molecules, has a width of ~200 μeV, but is clearly out of the dynamic range of the instrument. The narrow component was assigned to the lateral diffusion of the lipid molecules. The broadening could well be fitted using a Lorentzian function rather than a Gaussian. The data were fit with three components: an asymmetric Gaussian and a background, a narrow (1–24 μeV) Lorentzian function to describe the lipid diffusion, and a broad (~200 μeV) Lorentzian function. The instrumental resolution was determined by fitting data measured in the frozen state of the bilayers, at $T = 240$ K, using the asymmetric Gaussian function to accommodate the slight asymmetry in the resolution function of the BASIS spectrometer†. The parameters were then used to fit the quasi-elastic broadening observed at $T = 303$ K.

Fig. 4 plots the FWHM of the Lorentzian, following deconvolution with the instrumental resolution, as a function of $q_{\|}^2$. The data can well be fit by a straight line, making it possible to determine the diffusion constant using eqn (1), $D = 60 \pm 10 \times 10^{-12}$ m^2 s^{-1}. The data deviate from the straight line around $q_{\|} = 1$ Å^{-1}, giving rise to faster dynamics. Diffusion seems to be enhanced at nearest neighbour distance of the lipid molecules of about 6 Å (2π/1 Å^{-1}).

When comparing to eqn (1) and (2), the most likely mechanism for diffusion in single supported bilayers seems to be continuous diffusion rather than the flow-like motion reported for multi-lamellar

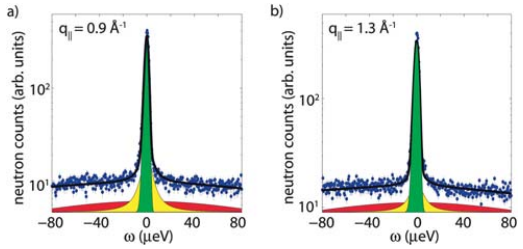

Fig. 3 Spectra for a) $q_{\|} = 0.9$ Å^{-1} and b) 1.3 Å^{-1}. The error bars shown are the result of statistical uncertainty. Data were fitted (black) with the instrumental resolution (green), a Lorentzian quasi-elastic broadening (yellow) and an additional broad Lorentzian (red).

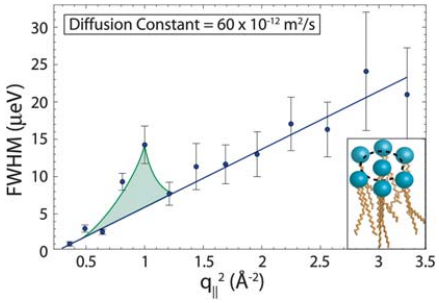

Fig. 4 FWHM of the Lorentzian as a function of $q_{\|}^2$. When excluding data points around $q_{\|} = 1$ Å^{-1}, data can be fit using a linear function. Diffusion seems to be enhanced around $q_{\|} = 1$ Å^{-1}, as indicated by the peak. Error bars correspond to a 10% confidence level in the Lorentzian fit. The inset shows a sketch of the lipid packing that might give rise to an enhanced nearest neighbour diffusion.

membranes stacks. The peak like feature around 1 Å^{-1} in Fig. 4 shows evidence for an enhanced diffusion of the lipid molecules, possibly triggered by voids in the ordered arrangement of lipids. The diffusion constant we found lies well within the range of diffusion constants of fluid phospholipid bilayers reported in the literature (18–180 × 10^{-12} m^2 s^{-1} [2,3,16,17]). However, because we cannot resolve a possible difference in the diffusion constants of the lipids in the upper and lower leaflets of the bilayer, we cannot exclude the possibility that the diffusion in the lower leaflet is suppressed by the presence of the substrate, while the diffusion in the upper leaflet may be enhanced by a highly ordered fluid phase of the lipids, thereby averaging to a diffusion constant which is comparable to multilamellar systems.

This change of character and enhanced nearest neighbour diffusion is most likely to be due to the highly ordered fluid phase of the lipids caused by the confinement of the defect free bilayer on the substrate. Note that the diffusion constants, as determined by incoherent neutron scattering, are usually an order of magnitude above the values obtained by macroscopic techniques in single[18,19] and multi-lamellar systems.[20] This may be due to coherent motion of lipid molecules, which are speculated to move as loosely bound clusters rather than individual molecules.[4,21]

This experiment has also demonstrated the feasibility of performing inelastic neutron scattering experiments on single supported bilayer systems. Complex membranes containing different membrane embedded proteins, as well as cholesterol, can be prepared. By tuning bilayer properties, such as elasticity, the impact of membrane properties on protein function may be elucidated. Inelastic neutron scattering experiments were once limited by the availability of sample material. The sample used for this study contained less than 1 mg of lipids. This opens up new opportunities for dynamical neutron scattering experiments in relevant and highly topical membrane/protein systems.

Acknowledgements

This research was supported by the Natural Sciences and Engineering Research Council of Canada (NSERC), the National Research

Published on 12 October 2010 on http://pubs.rsc.org | doi:10.1039/C0SM00637H
Downloaded by McMaster University on 20 June 2011

This journal is © The Royal Society of Chemistry 2010

View Online

Council Canada (NRC) and the Canada Foundation for Innovation (CFI). This work utilized facilities at the NIST Center for Neutron Research supported in part by the NSF under agreement No. DMR-0454672. Research at Oak Ridge National Laboratory's Spallation Neutron Source was sponsored by the Scientific User Facilities Division, Office of Basic Energy Sciences, U. S. Department of Energy.

References

1 G. Pabst, N. Kučerka, M.-P. Nieh, M. C. Rheinstädter and J. Katsaras, *Chem. Phys. Lipids*, 2010, **163**, 460–479.
2 W. Pfeiffer, T. Henkel, E. Sackmann and W. Knorr, *Europhys. Lett.*, 1989, **8**, 201–206.
3 S. Busch, C. Smuda, L. Pardo and T. Unruh, *J. Am. Chem. Soc.*, 2010, **132**, 3232–3233.
4 E. Falck, T. Róg, M. Karttunen and I. Vattulainen, *J. Am. Chem. Soc.*, 2008, **130**, 44–45.
5 A. James, M. Plank and R. Brown, *Phys. Rev. E: Stat., Nonlinear, Soft Matter Phys.*, 2008, **78**, 051128.
6 E. Sackmann, *Science*, 1996, **271**, 43–48.
7 M. Tanaka and E. Sackmann, *Nature*, 2005, **437**, 656–663.
8 R. Richter, A. Mukhopadhyay and A. Brisson, *Biophys. J.*, 2003, **85**, 3035–3047.
9 D. J. Bicout and G. Zaccai, *Biophys. J.*, 2001, **80**, 1115–1123.
10 E. Nováková, K. Giewekemeyer and T. Salditt, *Phys. Rev. E: Stat., Nonlinear, Soft Matter Phys.*, 2006, **74**, 051911.
11 M. Weik, U. Lehnert and G. Zaccai, *Biophys. J.*, 2005, **89**, 3639–3646.
12 M. C. Rheinstädter, T. Seydel, F. Demmel and T. Salditt, *Phys. Rev. E: Stat., Nonlinear, Soft Matter Phys.*, 2005, **71**, 061908.
13 A. F. Xie, R. Yamada, A. A. Gewirth and S. Granick, *Phys. Rev. Lett.*, 2002, **89**, 246103.
14 A. Charrier and F. Thibaudau, *Biophys. J.*, 2005, **89**, 1094–1101.
15 M. Bée, *Quasielastic Neutron Scattering: Principles and Applications in Solid State Chemistry, Biology and Materials Science*, Taylor & Francis, 1988.
16 A. Buchsteiner, T. Hauß, S. Dante and N. Dencher, *Biochim. Biophys. Acta, Biomembr.*, 2010, **1798**, 1969–1976.
17 S. König, W. Pfeiffer, T. Bayerl, D. Richter and E. Sackmann, *J. Phys. II*, 1992, **2**, 1589–1615.
18 M. Roark and S. E. Feller, *Langmuir*, 2008, **24**, 12469–12473.
19 C. Scomparin, S. Lecuyer, M. Ferreira, T. Charitat and B. Tinland, *Eur. Phys. J. E*, 2009, **28**, 211–220.
20 R. Merkel, E. Sackmann and E. Evans, *J. Phys.*, 1989, **50**, 1535–1555.
21 M. C. Rheinstädter, J. Das, E. J. Flenner, B. Brüning, T. Seydel and I. Kosztin, *Phys. Rev. Lett.*, 2008, **101**, 248106.

Downloaded by McMaster University on 20 June 2011
Published on 12 October 2010 on http://pubs.rsc.org | doi:10.1039/C0SM00637H

Chapter 7

Paper II: The Effect of Ethanol on the Collective Dynamics of Lipid Membranes

Martin D. Kaye, Karin Schmalzl, Valeria Conti Nibali, Mounir Tarek and Maikel Rheinstädter *Ethanol enhances collective dynamics of lipid membranes*, Physical Review E, **83**, 050907 (4 pages), 2011

Preface to Paper II

In this study the collective lipid tail dynamics of DMPC-ethanol systems were investigated with inelastic neutron scattering and all atom molecular dynamics simulations. Ethanol is known to bond to lipid headgroups and increase membrane permeability. In this paper, we present evidence that ethanol also modifies the collective lipid tail dynamics. A new low energy dynamic mode associated with lipid tail dynamics was observed in fluid phase multilamellar DMPC bilayers immersed in a 5% ethanol/water solution. This mode was observed in both inelastic neutron experiments and molecular dynamics simulations at energies of 0.8 meV and shows little dispersion. The well known acoustic phonon mode present in pure lipid systems is also observed in the DMPC-ethanol system with energies up to 4.5 meV. Both dynamic modes demonstrate both longitudinal and transverse character which may be related to molecular motions perpendicular to the bilayer. Passive membrane transport of small molecules is theorized to occur by the formation and perpendicular travel of small kink defects in the hydrophobic membrane core. This is consistent with the enhanced collective motion and enhanced permeability observed in the DMPC-ethanol system. However, further studies are required to determine the molecular origin of this mode and its relation to permeability.

I was the primary investigator in this study. This involved the analysis of both inelastic neutron scattering and molecular dynamics data. Fitting of the neutron scattering and longitudinal and transverse molecular dynamics curves was performed simultaneously to generate dispersion the displayed dispersion curves. Neutron scattering experiments were performed by Dr. Maikel Rheinstädter and all atom molecular dynamics simulations were performed by Dr. Mounir Tarek and Valeria Conti Nibali. Dr. Karin Schmalzl, Dr. Mounir Tarek and Dr. Maikel Rheinstädter contributed to the discussion of the analysis results.

PHYSICAL REVIEW E **83**, 050907(R) (2011)

Ethanol enhances collective dynamics of lipid membranes

Martin D. Kaye,[1] Karin Schmalzl,[2] Valeria Conti Nibali,[3] Mounir Tarek,[4,*] and Maikel C. Rheinstädter[1,5,†]

[1]*Department of Physics and Astronomy, McMaster University, Hamilton, Ontario, L8S 4M1 Canada*

[2]*Jülich Centre for Neutron Science, Forschungszentrum Jülich, Outstation at ILL, F-38042 Grenoble Cedex 9, France*

[3]*Dipartimento di Fisica, Università degli Studi di Messina, I-98100 Messina, Italy*

[4]*UMR 7565, Structure et Réactivité des Systèmes Moléculaires Complexes, CNRS-Nancy University, F-54506 Vandoeuvre les Nancy, France*

[5]*Canadian Neutron Beam Centre, National Research Council Canada, Chalk River, Ontario, K0J 1J0 Canada*

(Received 18 December 2010; published 25 May 2011)

From inelastic neutron-scattering experiments and all atom molecular dynamics simulations we present evidence for a low-energy dynamical mode in the fluid phase of a 1,2-dimyristoyl-sn-glycero-3-phoshatidylcholine (DMPC) bilayer immersed in a 5% water/ethanol solution. In addition to the well-known phonon that shows a liquidlike dispersion with energies up to 4.5 meV, we observe an additional mode at smaller energies of 0.8 meV, which shows little or no dispersion. Both modes show transverse properties and might be related to molecular motion perpendicular to the bilayer.

DOI: 10.1103/PhysRevE.83.050907 PACS number(s): 87.16.dj, 29.30.Hs, 87.10.Tf

Lipid bilayers have long been considered to be homogeneous, largely passive fluid barriers based on Singer and Nicholson's fluid model from 1972 [1]. However, it seems to be increasingly accepted that the diversity and composition of lipids play an important role in the function of biological membranes [2]. Bilayers regulate membrane elasticity, mediate protein-protein interactions [3], and are speculated to be important for transmembrane transport of small molecules [4–7].

Because of their ability to hydrogen bond with the head groups [Fig. 1(a)], short-chain alcohols, such as ethanol, are primarily located in the hydrophilic head group region [8–10], with bonding lifetimes of about 1 ns [10]. Ethanol has a number of effects on lipid bilayers: It decreases the gel-to-fluid transition temperature [8,11], has a weak effect on the area per lipid, and increases membrane fluidity and disorder [10]. Finally, it was found to increase membrane permeability [10,12,13].

In this Rapid Communication we present evidence that ethanol modifies collective lipid-chain fluctuations. The impact of ethanol on membrane core dynamics was quantified by determining the collective short wavelength fluctuations on the 100-ps time scale from inelastic neutron scattering experiments and all atom molecular dynamics (MD) simulations. In addition to the acoustic mode that has been reported previously in phospholipid bilayers, we find evidence for a new low-energy mode. This excitation may be related to the enhanced permeability observed in the presence of ethanol molecules.

Highly oriented multilamellar membrane stacks of several thousands of chain deuterated 1,2-dimyristoyl-sn-glycero-3-phoshatidylcholine (DMPC-d54) bilayers were prepared by spreading a solution of 25 mg/ml lipid in trifluoroethanol/chloroform (1:1) on 2-in. silicon wafers, followed by subsequent drying in vacuum. Twenty such wafers separated by small gaps were combined and aligned with respect to each other (total mosaicity about 0.5°). The deuterated samples had a total mass of about 400 mg. The stability of stacked bilayers in ethanol/water solutions with different concentrations was checked using x-ray reflectivity. Bilayers in solutions with concentrations of more than 5% ethanol could not be stabilized for more than a couple of hours because of the well-known effect of thermal unbinding [14]. Stable bilayers in water/5% ethanol could eventually be prepared by adding 2% (weight/weight) polyethylene glycol (PEG) with a molecular weight of 20 000. PEG is known to exert an osmotic pressure on the membrane stack that stabilizes the lamellar structure [15]. PEG was reported not to participate in the DMPC bilayer and, therefore, not to have a direct effect on lipid structure and dynamics [16]. A concentration of 5% ethanol (corresponding to a 1 M ethanol solution) results in a structure where, on average, one ethanol molecule is attached to each lipid molecule [17]. The sandwich sample was completely immersed in about 40 ml of a D_2O/C_2D_5OD/PEG solution to ensure a defined alcohol concentration in the

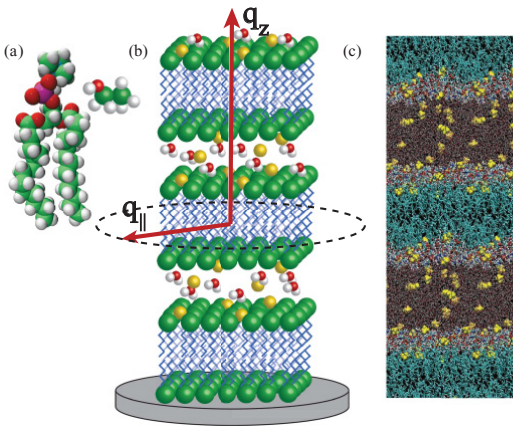

FIG. 1. (Color online) (a) Lipid (DMPC) and ethanol molecule. (b) Sketch of the supported multilamellar membrane stacks used in the neutron scattering experiment. (c) Snapshot of an all atom molecular dynamics simulation of DMPC/1M ethanol. Water molecules are depicted in red and white; ethanol molecules are depicted in yellow.

*Mounir.Tarek@srsmc.uhp-nancy.fr
†rheinstadter@mcmaster.ca

 ©2011 American Physical Society

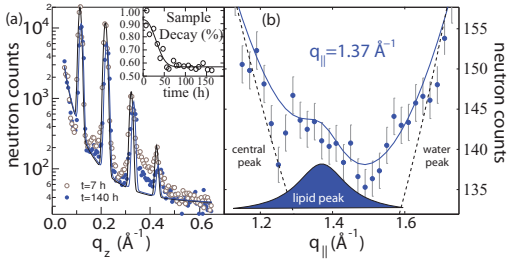

FIG. 2. (Color online) (a) Neutron reflectivity curves. (Inset) Decay of the integrated intensity of the first Bragg peak, normalized to the initial intensity. The solid line is a fit after a single exponential decay. (b) In-plane neutron diffraction of the DMPC/ethanol system. The lipid acyl chain correlation peak was observed at $q_{||} = 1.37$ Å^{-1}.

bilayers, and mounted in a hermetically sealed aluminium container within a cryostat. Figure 1(b) shows a sketch of the supported multilamellar membrane stacks used in the neutron scattering experiment. Temperature was kept constant at $T = 303$ K during the experiment, in the fluid phase of the bilayers.[1] The experiment was performed on the IN12 cold triple-axis spectrometer at the high flux reactor of the Institut Laue-Langevin, Grenoble, France. IN12 was equipped with vertically focusing monochromator and analyzer and the beam was collimated to 40′-monochromator-30′-sample-30′-analyzer-60′-detector. Scans were done in the W configuration with fixed values of $k_f = 1.75$ and $k_f = 1.25$ Å^{-1}, resulting in a q resolution of $\Delta q = 0.005$ Å^{-1} and energy resolutions of $\Delta\hbar\omega = 200\ \mu$eV and 60 μeV, respectively. Dynamic ranges of ∼4.5 meV respectively ∼1 meV were accessible using these two setups.

Figure 2(a) shows neutron reflectivity curves (q_z) taken after the sample cell was closed and at the end of the experiment, after $t = 140$ h. The lamellar spacing, d_z, was determined from the positions of the four well-developed Bragg peaks to be $d_z = 64.5$ Å. Note that this value is slightly lower than the value reported for DMPC under full hydration of $d_z = 66$ Å [18]. From MD simulations [9] ethanol was reported to decrease d_z in DMPC/ethanol stacks. However, the decrease in d_z must also partially be attributed to the osmotic pressure exerted by the addition of PEG to the solution. The inset in Fig. 2(a) depicts the decay of the integrated intensity of the first reflectivity Bragg peak normalized to the initial intensity with time. The solid line is a fit after a single exponential decay. Despite the use of PEG, the amount of lipids in the lamellar structure decayed to about 60% after 50 h. Using the fit function, the counts of all scans were extrapolated to $t = 0$ s such that all scans could be compared and combined.

In-plane diffraction of the DMPC/ethanol system ($q_{||}$) is shown in Fig. 2(b). The total scattering consists of a pronounced central peak at $q_{||} = 0$ Å^{-1} and a (heavy) water peak at about 2.0 Å^{-1}, the nearest-neighbor distance of the water molecules in solution. The structure factor, $S(q_{||})$, of the lipid tails has a maximum centered at $q_{||} = 1.37$ Å^{-1}, corresponding to an average lipid acyl chain distance of $d = 4.60$ Å, slightly larger than in pure DMPC-d54, where 4.50 Å were reported [19]. The corresponding areas per lipid can roughly be estimated from the position of the chain correlation peak [20] to be $A_L = 2.64(9d/8)^2 = 70.7$ Å^2 compared to 67.6 Å^2 for the pure DMPC bilayer. The area per lipid was therefore found to increase by about 4% in the presence of the ethanol molecules. We note, however, that it is not possible to compute the area per lipid directly from the interchain distance [21].

MD simulations of pure DMPC and DMPC-ethanol systems were performed at 303 K in the liquid crystal phase of the membrane. Each system infinitely replicated in a multilamellar array by 3D periodic boundary conditions contained 72 lipids, at excess hydration (∼45 water molecules). We have considered a system at a high ethanol concentration (686 ethanol molecules partitioned in the water baths) and let it relax using constant pressure and constant temperature simulations. After ∼100 ns it equilibrated toward a final configuration where a fraction of ethanol molecules partitioned within the lipid, see Fig. 1(c) for a snapshot of the system. The DMPC and DMPC/ethanol systems were characterized by average areas per lipid of respectively 61.5 and 69.2 Å. These were considered in satisfactory agreement with experiment. Further simulations used to generate the scattering curves were performed at constant volume and constant temperature for duration of 4 ns each in order to cover the length scale corresponding to the experimental resolution. Both, the NVT and the NPT MD simulations were carried out using NAMD2 [22]. The equations of motion were integrated using a multiple time-step algorithm [23]. Short- and long-range forces were calculated every two and four time steps respectively, with a time step of 2.0 fs. Chemical bonds between hydrogen and heavy atoms were constrained to their equilibrium value. Long-range electrostatic forces were taken into account using the particle mesh Ewald (PME) approach [24]. The lipids were described by all-atom, empirical force fields proposed by Hogberg *et al.* [25], the water molecules by the TIP3P model [26], and the ethanol force field was taken from [27]. The connection between the MD trajectories and the inelastic neutron data is via the density correlation function. The correlation function was calculated from the MD trajectory as $I(q_{||},t) = \langle n^*(q_{||},0)n(q_{||},t)\rangle$, where $n(q_{||},t)$ is the generalized density fluctuation, $n(q_{||},t) = 1/\sqrt{N}\sum_\alpha b_\alpha \exp\{iq_{||}\cdot r_\alpha(t)\}$, with $r_\alpha(t)$ the position of the αth scatterer at time t and b_α its neutron scattering length density and N the number of scatterers. $S(q_{||},\hbar\omega)$ was calculated as a Fourier transform of $I(q_{||},t)$ [28]. For each wave vector selected in the range [0.4 Å^{-1} and 2 Å^{-1}], the $I(q_{||},t)$s were averaged over values obtained considering a minimum of 20 randomly selected q values, providing a 2d powder average of the scattering. Here we focused on the lipid tail dynamics and therefore considered only contributions from the C atoms in the hydrocarbon chains so the experimental and simulated data can be compared directly. In addition, simulation data were convoluted with an energy resolution of 80 μeV, comparable to the experimental instrumental resolution. The MD data were also used to calculate the transverse dynamics of the lipid tails. The transverse current spectra, $C_T(q_{||},\omega)$, were

[1] In multilamellar DMPC-d54 bilayers the transition from the gel into the fluid phase occurs at $T_m = 21.5°\text{C} = 294.7$ K [19].

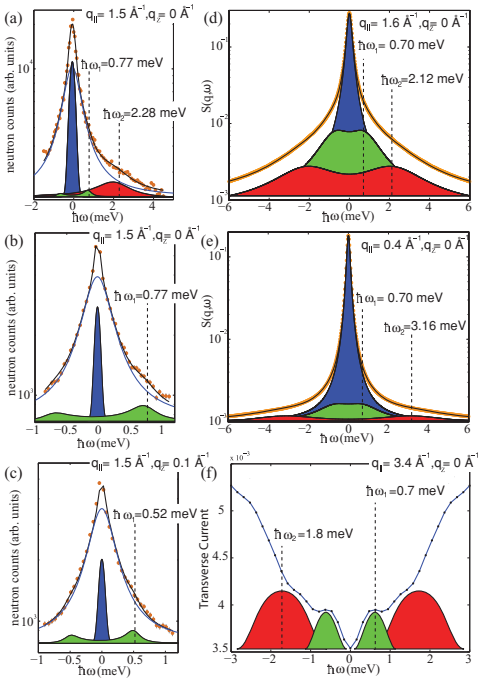

FIG. 3. (Color online) Spectra from experiment [(a), (b) and c)] and simulations [(d) and e)]. Two excitations are visible at $q_{||} = 1.5$ Å^{-1} in (a). Part (b) depicts the low-energy excitation at a higher energy resolution. In (c) a small q_z component was added to the total scattering vector and an excitation was observed at 0.5 meV. Simulation data are shown for $q_{||} = 1.6$ Å^{-1} (d) and $q_{||} = 0.4$ Å^{-1} (e). (f) Calculated transverse current spectra. Two propagating modes are visible at high $q_{||}$.

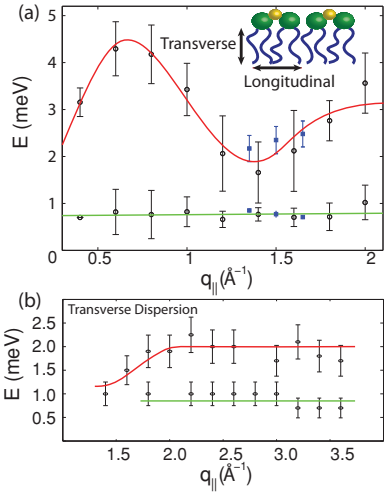

FIG. 4. (Color online) (a) Phonon energies as determined from experiment (■) and simulation (○). While the upper branch is also found in pure lipid bilayers, the low-energy branch is attributed to the presence of the ethanol molecules in the bilayers. (b) Dispersion of the calculated transverse current spectra. Propagating transverse modes were observed for $q_{||}$ values greater than 1.5 Å^{-1}. Solid lines are guides for the eye.

calculated following [29]. Note that these dynamics are not directly accessible experimentally [29].

Figure 3 shows the collective short wavelength dynamics of the DMPC-ethanol system from experiment and simulations. The neutron data in Figs. 3(a), 3(b), and 3(c) show a central (Gaussian) peak due to instrumental resolution and a quasielastic broadening centered at energy transfer $\hbar\omega = 0$ meV. This quasielastic component has contributions from coherent and incoherent scattering of the bilayers and solvent and could well be fitted by a Lorentzian peak shape. In addition, inelastic peaks were observed due to propagating collective in-plane dynamics of the deuterated membrane core. Two peaks were observed in Fig. 3(a), one at an energy of 2.28 meV and a second one at a smaller energy of 0.77 meV. The latter is more evident in the high-resolution experiment [Fig. 3(b)]. The corresponding energies were determined by fitting damped harmonic oscillators (DHO) to the spectra. Phonon energies were determined at $q_{||}$ values of $q_{||} = 1.35$, 1.5, and 1.65 Å^{-1}, around the lipid correlation peak, where the coherent scattering of the sample was found to be dominated by the coherent scattering of the lipid membrane core [19]. Note that the momentum transfer in the scans in Figs. 3(a) and 3(b) was longitudinal and the observed modes have longitudinal properties. To determine an additional potential transverse character, additional scans have been conducted by adding a small q_z component to the total scattering vector **Q**. In the corresponding scan in Fig. 3(c), an excitation at slightly smaller energy values of 0.5 meV was observed. Selected $S(q_{||},\hbar\omega)$ spectra evaluated from the MD simulations trajectories of the DMPC-ethanol system are shown in Figs. 3(d) and 3(e). The spectra were fit using the effective eigenmode model [28], which consists of a central heat mode and propagating sound modes located at $+\hbar\omega$ and $-\hbar\omega$. Two such modes were visible in the spectra and their energies were determined from the position of asymmetric Lorentzian peak shapes. Figure 3(f) shows the transverse current spectra at $q_{||} = 3.4$ Å^{-1}. Two excitations are visible, one at 1.8 meV and a second, low-energy, excitation at 0.7 meV. These energy values correspond to the excitation energies in the longitudinal scans within the given errors. Propagating modes could be identified in the transverse current spectra at $q_{||}$ values higher than about 1.5 Å^{-1} only, corresponding to less than a nearest-neighbor lipid tail distance. The transverse dynamics are most likely relaxational at smaller $q_{||}$ values as the shear modulus is expected to be small in the fluid phase of the membranes.

The dispersion relations for longitudinal and transverse dynamics are shown in Fig. 4. Two branches are visible in the longitudinal spectra in Fig. 4(a). The dispersive mode at higher energies of about 4 meV coincides well with the mode previously reported for pure lipid bilayers from simulations [21,28] and experiments [19,30]. The new mode at lower

energies of about 0.8 meV appears to be less dispersive. Experimental and computational data for pure DMPC bilayers were analyzed in parallel and no sign of this low-energy mode was found. The latter mode was therefore attributed to the presence of the ethanol molecules in the bilayer. Two branches are also visible in the transverse current spectra in Fig. 4(b), as determined from the simulations.

An acoustic phonon branch was previously observed in lipid bilayers. This phonon has a typical shape: It shows a linear increase at small $q_{||}$ values due to long wavelength sound propagation, and a pronounced minimum at $q_{||}$ values corresponding to the nearest-neighbor distances of lipid acyl tails. Our data suggest that this mode is not altered by the presence of the ethanol molecules. The mode at $\sim$0.8 meV not present in the pure lipid shows little or no dispersion. This conclusion is, however, mainly based on simulation data as the experimental data cover a much smaller $q_{||}$ range. The position of the low energy excitation in the experiment appears to be sensitive to the perpendicular direction as it shifts when adding a small q_z component. Both simulations and experiment therefore point to a partial transverse, out-of-plane character of this mode. Both modes are also observed in the calculated transverse current spectra. The molecular motions associated with these modes can thus be pictured as coherent displacements of the carbon atoms in the lipid tails in the plane of the membrane, and partially also along the bilayer normal. As the collective lipid tail dynamics is related to the mobility of kink defects and small voids in the hydrophobic membrane core [6], both modes might be important for transmembrane transport. In particular the low energy mode in the presence of ethanol could be related to the enhanced transmembrane transport of small molecules. However, further investigations are needed in order to pinpoint the molecular origin of this mode.

In summary, we present the first inelastic scattering experiments to study collective lipid dynamics of supported bilayers in a water-ethanol solution complemented by all atom MD simulations. Experiment and simulation reveal an additional low-frequency collective mode associated with the acyl chain dynamics, when ethanol is embedded within the lipid bilayers. From experiment and simulations the collective hydrophobic membrane core dynamics show transverse properties, related to molecular motions perpendicular to the membrane. Whether these modes are related to transmembrane transport of small molecules will be an important question in future experiments and simulations.

We acknowledge financial support from the Natural Sciences and Engineering Research Council and National Research Council of Canada and thank the Institut Laue-Langevin for the allocation of beam time. V.C.-N. has carried out research under an HPC-EUROPA2 project (project number 228398). We are grateful to W. Treptow for help on the simulations of the initial ethanol water systems. Calculations were performed at the CINES supercomputer center (Montpellier, France).

[1] S. Singer and G. Nicolson, Science **175**, 720 (1972).
[2] D. M. Engelman, Nature **438**, 578 (2005).
[3] M. Rheinstädter, K. Schmalzl, K. Wood, and D. Strauch, Phys. Rev. Lett. **103**, 128104 (2009).
[4] D. Huster *et al.*, Biophys. J. **73**, 855 (1997).
[5] B. Deamer and J. Bramhall, Chem. Phys. Lipids **40**, 167 (1986).
[6] S. Paula *et al.*, Biophys. J. **70**, 339 (1996).
[7] G. Lahajnar *et al.*, Biochim. Biophys. Acta **1235**, 437 (1995).
[8] J. A. Barry and K. Gawrisch, Biochemistry **33**, 8082 (1994).
[9] J. Chanda and S. Bandyopadhyay, Chem. Phys. Lett. **392**, 249 (2004).
[10] M. Patra *et al.*, Biophys. J. **90**, 1121 (2006).
[11] S. Feller *et al.*, Biophys. J. **82**, 1396 (2002).
[12] H. Komatsu and S. Okada, Chem. Phys. Lipids **85**, 67 (1997).
[13] H. V. Ly and M. L. Longo, Biophys. J. **87**, 1013 (2004).
[14] M. Vogel, C. Munster, W. Fenzl, and T. Salditt, Phys. Rev. Lett. **84**, 390 (2000).
[15] U. Mennicke and T. Salditt, Langmuir **18**, 8172 (2002).
[16] G. Georgiev, G. Georgiev, and Z. Lalchev, Eur. Biophys. J. **35**, 352 (2006).
[17] M. Jansen and A. Blume, Biophys. J. **68**, 997 (1995).
[18] N. Chu, N. Kucerka, Y. Liu, S. Tristram-Nagle, and J. F. Nagle, Phys. Rev. E **71**, 041904 (2005).
[19] M. Rheinstädter, C. Ollinger, G. Fragneto, F. Demmel, and T. Salditt, Phys. Rev. Lett. **93**, 108107 (2004).
[20] A. Spaar and T. Salditt, Biophys. J. **85**, 1576 (2003).
[21] J. S. Hub *et al.*, Biophys. J. **93**, 3156 (2007).
[22] L. Kalé *et al.*, J. Comput. Phys. **151**, 283 (1999).
[23] J. A. Izaguirre, S. Reich, and R. Skeel, J. Chem. Phys. **110**, 9853 (1999).
[24] T. Darden, D. York, and L. Pedersen, J. Chem. Phys. **98**, 10089 (1993).
[25] C.-J. Högberg, A. Nikitin, and A. Lyubartsev, J. Comput. Chem. **29**, 2359 (2008).
[26] W. L. Jorgensen *et al.*, J. Chem. Phys. **79**, 926 (1983).
[27] M. Tarek, D. Tobias, and M. Klein, Physica A **231**, 117 (1996).
[28] M. Tarek, D. J. Tobias, S. H. Chen, and M. L. Klein, Phys. Rev. Lett. **87**, 238101 (2001).
[29] M. Sampoli, G. Ruocco, and F. Sette, Phys. Rev. Lett. **79**, 1678 (1997).
[30] S. H. Chen *et al.*, Phys. Rev. Lett. **86**, 740 (2001).

Chapter 8

Vapour Phase Ethanol Experiments

The presence of a new low energy mode with perpendicular character in DMPC-Ethanol systems warrants further investigation. As mentioned in chapter 2, the difficulty in constructing lipid bilayers in ethanol is that it is not naturally incorporated into the bilayer, and must be added either from the aqueous or vapour phase. The presence of the intense heavy water scattering at $\boldsymbol{q}_{||} = 2$ Å^{-1} and strong elastic contribution near the tail-tail interaction peak limited the experimentally accessible lipid signal in neutron scattering experiments of DMPC immersed in water-ethanol solutions. Thermal unbinding and vertical sample orientation also limited stable DMPC-Ethanol systems to ethanol concentrations of 5%. The x-ray hydration chamber allowed hydration of 100% DMPC samples from the vapour phase and in a horizontal orientation. In this configuration, the ethanol concentration is tunable by adjusting the contents of the hydration chamber trough, and stable DMPC bilayers could be prepared in the presence of ethanol solutions at concentrations up to 20% by mass.

8.1 X-ray Experiments

Stacked DMPC-ethanol systems were examined with x-ray diffraction using the Biological Large Angle Diffraction Experiment (BLADE). Solid supported multilamellar DMPC bilayers with ∼5000 layers were prepared on 1 × 1 cm^2 Silicon (111) wafers

according to the APTES preparation method described in chapter 3. DMPC samples were carefully aligned in the center of the x-ray hydration chamber pillar before adding 5 mL of ethanol water solution to the trough. Precise sample alignment was performed by BLADE software for consistency throughout the experiment. Ethanol-water solutions were prepared at concentrations of 0, 1, 5, 10 and 20 % ethanol by mass. Samples were allowed to equilibrate for at least 2 hours after closing the x-ray hydration chamber to ensure consistent hydration. X-ray 2D in-plane scans were performed over a period of 18h at 299 K. This provided scattered x-ray intensity maps between -0.3 to 3.0 Å^{-1} $\boldsymbol{q}_{||}$ and 0 to 1.4 Å^{-1} $\boldsymbol{q}_z$. Two high temperature air guns were arranged around the sample hydration chamber to blow hot air over the Kapton windows for the duration of the experiment. The increased window temperature prevented condensation on the Kapton windows and enhanced condensation on the sample. Air guns were set to 115^{o}C and 100^{o}C for the large and small Kapton windows respectively. Temperature inside the chamber was controlled by adjusting the temperature of the water bath which is pumped directly underneath the hydration chamber trough and sample pillar (see Figure 5.12c). The final 20% ethanol solution was also saturated with K_2SO_4 to produce a relative humidity of 97% and reduce condensation on the hydration chamber pillar surrounding the sample.

A 2D in-plane scan of a dry 100% DMPC control sample at 299 K is shown in Figure 8.1. Displacement along the x-axis indicates a decrease in in-plane lengthscale and displacement in the y-direction indicates decreasing perpendicular lengthscale. At $\boldsymbol{q}_{||} = 0$, a series of high intensity spots appear along the $\boldsymbol{q}_z$ axis. At large in-plane lengthscales the bilayer stack appears as a series of flat layers. The high intensity spots are indicative of this three dimensional long range order of the bilayer stack and correspond to Bragg reflections from different layers of the sample. The circular arc of intensity surrounding these peaks is a powder average result of the mosaicity of the sample. Deviations from the horizontal bilayer plane orientation indicate the contribution from the bilayer spacing is no longer aligned with $\boldsymbol{q}_z$, but also has a $\boldsymbol{q}_{||}$ component, which leads to Bragg peak shifting off the $\boldsymbol{q}_z$ axis. The in-plane ordering of the bilayers is demonstrated by rod-like structures at $\boldsymbol{q}_{||} = 1.4$ Å^{-1} and 1.0 Å^{-1}. The rod at $\boldsymbol{q}_{||} = 1.4$ Å^{-1}, corresponding to lengthscales of 4.5 Å demonstrates the two dimensional ordering of the lipid tails. The rod at $\boldsymbol{q}_{||} = 1.0$ Å^{-1} demonstrates

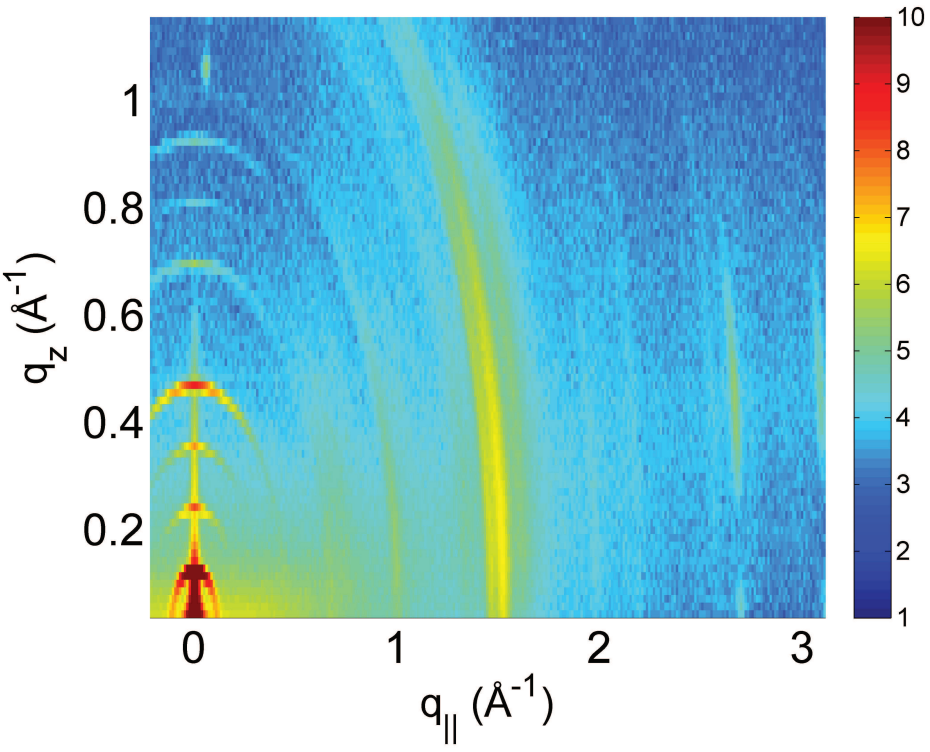

Figure 8.1: 18 hour 2D in-plane scan of an unhydrated pure DMPC sample at 299 K. In-plane and perpendicular structure are not coupled. Sample imperfections lead to the very small (log scale) arc structures seen in intensity peaks.

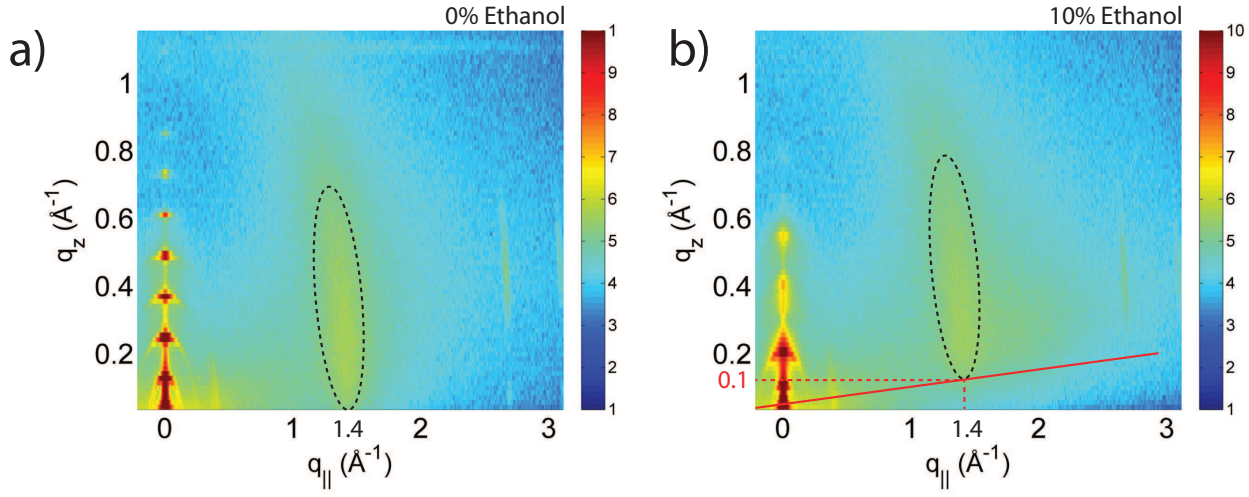

Figure 8.2: a) Depicts a 2D in-plane scan of a pure DMPC bilayer hydrated with pure water at 299 K. Note the position of the tail-tail interaction peak at $\boldsymbol{q}_z = 0$. b) 2D in-plane scan of a pure DMPC bilayer hydrated with pure water and 10% ethanol at 26^{o}C. Here we see the peak has shifted upwards in $\boldsymbol{q}_z$ by $\sim$0.1 Å^{-1}. This points to an increase in the perpendicular dynamics in the DMPC-ethanol system. The observed lengthscale corresponds to 63 Å, approximately equivalent to one bilayer thickness.

the headgroup ordering associated with an increase in lipid molecular order in the gel ($L_{\beta'}$) phase. A similar powder average pattern is observed for both of these rod structures which is again indicative of the sample mosaicity.

2D in-plane scans of vapour hydrated 100% DMPC samples in pure water and 10% ethanol solutions at 299 K are shown in Figure 8.2. The hydrated scans demonstrate an increase in disorder which leads to a diffusion of the scattering signal called *diffuse scattering*. Well defined Bragg peaks are still visible as well as the lipid tail-tail interaction signal at $\boldsymbol{q}_{||} = 1.4$ Å^{-1}. The signal at $\boldsymbol{q}_{||} = 1.0$ Å^{-1} corresponding to headgroup spacing is not present, which is consistent with a transition to the fluid (L_α) phase. The primary difference between the pure water and 10% ethanol scans shown is the position of the tail-tail interaction signal. In the pure water and dry scan, the intensity of the tail-tail rod begins at $\boldsymbol{q}_z = 0$ Å^{-1}. In the 10% ethanol scan this peak has shifted upwards to begin at $\sim \boldsymbol{q}_z = 0.1$ Å^{-1}. This displacement corresponds to a lengthscale of $\sim$63 Å which is similar to the fluid phase DMPC bilayer thickness $d_z = 62.6$ Å [10] and to the thickness observed in our previous neutron experiments

($d_z = 64.5$ Å). A consistent displacement in the $\boldsymbol{q}_z$ position of the tail-tail interaction peak was observed for ethanol concentrations of 1, 5, 10 and 20%. A plot of the $\boldsymbol{q}_z$ shift as a function of ethanol concentration is shown in Figure 8.3. Error bars represent uncertainty as a result of excess diffuse scattering and pillar condensation (discussed below). The $\boldsymbol{q}_z$ displacement demonstrates a slope of 0.002 Å^{-1}/% which may indicate a constant displacement of $\sim$0.1 Å^{-1} with the addition of ethanol.

8.2 Discussion

A positive $\boldsymbol{q}_z$ displacement with the addition of ethanol is consistent with and complimentary to our previous neutron experiments. The displacement of the pure water tail-tail interaction peak at $\boldsymbol{q}_z = 0$ Å^{-1} demonstrates that lipid tail fluctuations have long characteristic lengthscales in the z direction. The displacement of the ethanol tail interaction peak of $\boldsymbol{q}_z = 0.1$ Å^{-1} relative to the pure water tail interaction peak represents a decrease in the significant lengthscale of tail interaction in the z direction. The tail-tail interaction peak in the ethanol samples exhibits z-direction lengthscale of one bilayer thickness or less, which indicates coherent tail fluctuations of these wavelengths are the most common. This is consistent with the perpendicular character observed in the acoustic phonon in the neutron experiments as well as the idea that coherent lipid tail fluctuations aid passive membrane transport. However, further examinations are required to quantify $\boldsymbol{q}_z$ displacement and identify its nature.

Some challenges remain for hydrating lipid bilayer samples with ethanol from the vapour phase. A major experimental difficulty was the accumulation of condensation in the path of the x-ray beam. Condensation on the Kapton windows could be limited by adjusting the position of air guns, but significant condensation built up on the sample pillar during the 18 hour scans. Large water droplets in the path of the beam lead to an increase in diffuse and water scattering unrelated to the sample hydration and obscured bilayer reciprocal space structural features (see Figure 8.4). Condensation could be limited in certain areas by adjusting the air guns. It is also difficult to determine the true concentration of ethanol on the sample. For the purposes of these preliminary experiments, the ethanol-water mixture was assumed to be ideal such that the concentration of ethanol condensing on the sample is the same

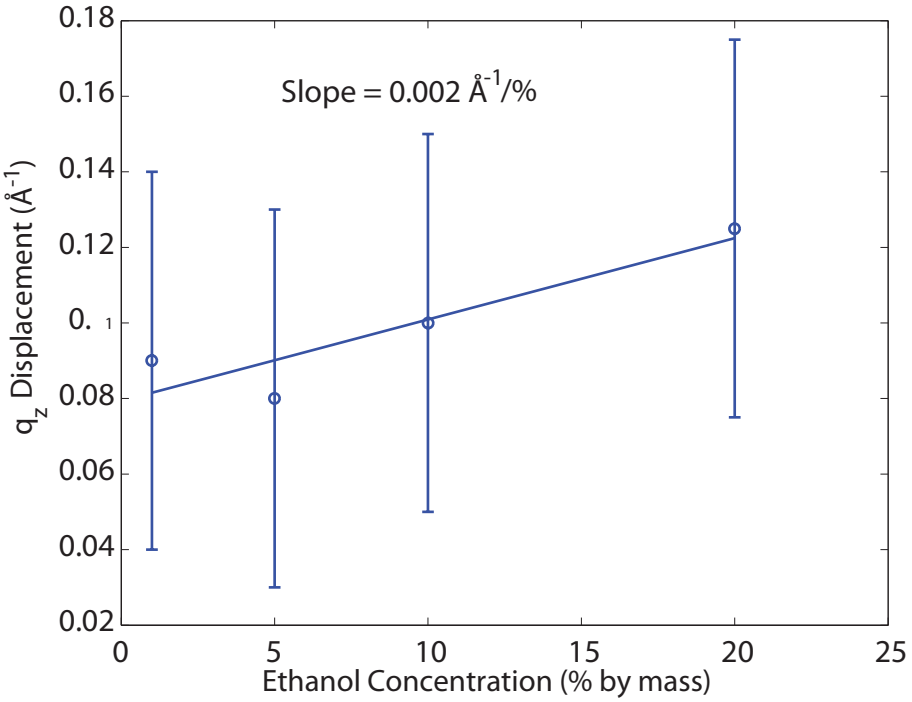

Figure 8.3: Shift in q_z observed with change in ethanol concentration. The errors reported are a result of the high degree of diffuse scattering present in the hydrated samples which partially obscured the tail interaction peaks at some concentrations.

as that of the liquid. The relative concentrations of ethanol and water vapour between their 351 K and 393 K is well defined, and indicates that at a given temperature more ethanol will be exchanged to the vapour phase, which results in higher re-condensed ethanol concentrations [74]. This issue is shown in Figure 8.5, where a solution with 30% ethanol will boil at ∼355 K and produce a vapour with nearly 60% ethanol. However, to my knowledge the concentration of ethanol in ethanol-water vapours below 351 K is undefined.

Despite these experimental difficulties, x-ray diffraction investigations of DMPC-ethanol systems show qualitative agreement with previous neutron experiments. Further diffraction experiments may reveal more about the perpendicular nature of lipid tail fluctuations in this system. High resolution reflectivity scans of DMPC-ethanol systems may also be performed to investigate perpendicular structural changes with the addition of ethanol at high resolution.

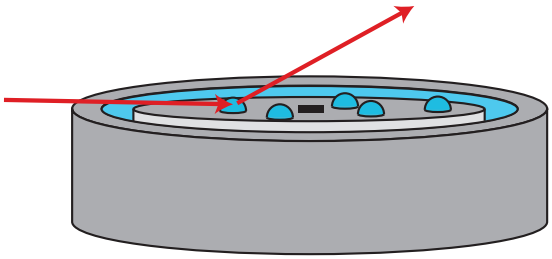

Figure 8.4: The presence of large water droplets on the x-ray hydration chamber sample pillar may create more diffuse and water scattering, which contributes to a diffuse scattering background.

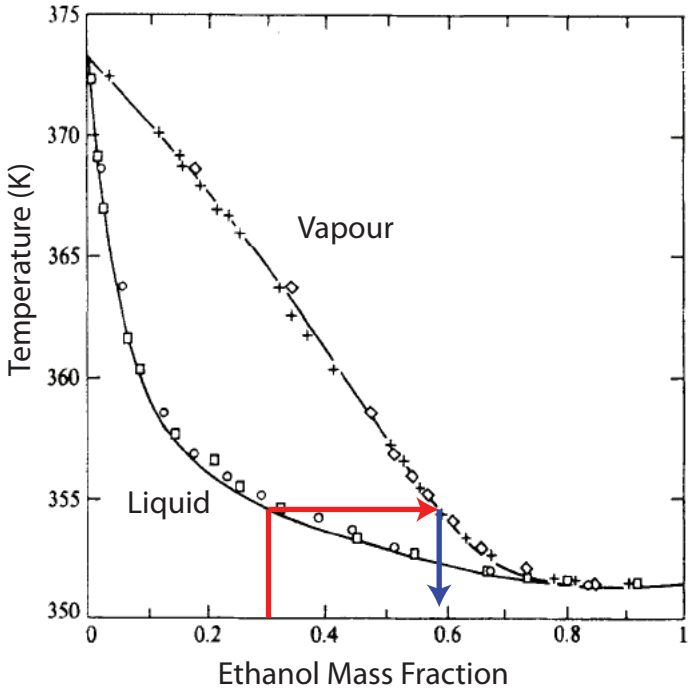

Figure 8.5: The vapour-liquid phase diagram for water-ethanol mixtures. At a given mass fraction of ethanol, the boiling point is defined by the liquid curve and the ethanol vapour content is defined by the vapour curve [74]. The pathway for evaporation (red) and subsequent re-condensation (blue) is indicated by arrows for an ethanol concentration of 30%.

Conclusions

In the work presented in the preceding document, we have studied the structure and dynamics of lipid bilayer systems. In particular, neutron and x-ray scattering techniques were employed to investigate the diffusion of single solid supported lipid bilayers and the impact of ethanol on collective lipid tail dynamics.

State of the art neutron backscattering spectrometry studies of single solid supported bilayers demonstrated for the first time that the time and lengthscales associated with single bilayer diffusion are accessible to neutron scattering. Diffusion constants for single solid supported DMPC bilayers were found to be consistent with previous macroscopic studies in multilamellar bilayers. However, the diffusion exhibited continuous character rather than a flow-like diffusion which was found in multilamellar bilayers. An enhanced diffusion was also observed at lengthscales of 6 Å near the lipid nearest neighbour distance. This may correspond to void formation in the liquid phase bilayers. The enhanced diffusion and continuous character observed may be a result of enhanced lipid order enforced by restriction to the substrate. The feasibility of neutron scattering studies of single supported bilayers opens the door for the investigation of more complex single solid supported bilayer systems containing macromolecules such as cholesterol or ethanol.

The collective dynamics of lipid-ethanol systems were also investigated. Inelastic neutron scattering and all atom molecular dynamics simulations were employed to study the collective dynamics of DMPC bilayers immersed in a 5% ethanol solution. Both experiment and simulation revealed an additional low-frequency mode in the lipid tails of the DMPC-ethanol system, which is not present in pure lipid systems.

The higher energy acoustic mode previously associated with lipid tail dynamics in pure lipid systems is also observed in the DMPC-ethanol system. Experiment and simulation reveal that these dynamics exhibit transverse character which may be associated with molecullar motions perpendicular to the bilayer. This may be related to the enhanced permeability observed in ethanol-membrane systems. X-ray diffraction studies of the DMPC-ethanol system hydrated from the vapour phase indicate that lipid tail fluctuations exhibit characteristic lengthscales equal to or less than one bilayer thickness. Passive transport of small molecules through the membrane core may be achieved by the formation and perpendicular motion of small kink defects. This is consistent with the enhanced collective dynamics and characteristic lengthscale observed, as well as the increased permeability in ethanol-membrane systems. However, further studies are required to fully characterize the molecular motions associated with the new dynamic mode and its relation to membrane permeability.

Bibliography

[1] S.J. Singer and G.L. Nicolson. The fluid mosaic model of the structure of cell membranes. *Science*, 175:720–731, 1972.

[2] R. Lipowsky and E. Sackmann, editors. *Structure and Dynamics of Membranes*, volume 1 of *Handbook of Biological Physics*. Elsevier, Amsterdam, 1995.

[3] G. Pabst, N. Kučerka, M. P. Nieh, M. C. Rheinstädter, and J. Katsaras. Applications of neutron and x-ray sccattering to the study of biologically relevant model membranes.

[4] R. Philips, J. Kondev, and Julie Theriot. *Physical Biology of the Cell*. Garland Science, Taylor & Francis Group, New York, New York, 2009.

[5] E. Fahy *et. al.* A comprehensive classification system for lipids. *Eur. J. Lipid. Sci. Technol.*, 107:337–364, 2009.

[6] E. Fahy *et. al.* Update of the lipid maps comprehensive classification system for lipids. *Journal of Lipid Research*, 50:S9–S14, 2009.

[7] B. Ramstedt and J. P. Slotte. Membrane properties of sphingomyelins. *FEBS Letters*, 531:33–37, 2002.

[8] J. K. Dhont, G. Gompper, and D. Richter, editors. *Soft Matter: Complex Materials on Mesoscopic Scales*. Forschungszentrum Jülich GmbH, Jülich, Germany, 2002.

[9] D. Marsh. *CRC Handbook of Lipid Bilayers*. CRC Press, 1990.

[10] N. Kučerka, Y. Liu, N. Chu, H. I. Petrache, S. Tristram-Nagle, and J. F. Nagle. Structure of fully hydrated fluid phase DMPC and DLPC lipid bilayers using x-ray scattering from oriented multilamellar arrays and from unilamellar vesicles. *Biophys. J.*, 88:2626–2637, 2005.

[11] M. Rheinstädter, C. Ollinger, G. Fragneto, F. Demmel, and T. Salditt. Collective dynamics of lipid membranes studied by inelastic neutron scattering. *Phys. Rev. Lett.*, 93:108107, 2004.

[12] D. Marsh. Intrinsic curvature in normal and inverted structures and in membranes. *Biophysical Journal*, 70:2248–2255, 1996.

[13] P. A. Janmey and P. K. J. Kinnunen. Biophysical properties of lipids and dynamic membranes. *TRENDS in Cell Biology*, 2006.

[14] G. S. Smith, E. B. Sirota, C. R. Safinya, R. J. Plano, and N. A. Clark. X-ray study of freely suspended films of a multilamellar lipid system. *Mol. Cryst. Liq. Cryst.*

[15] G. S. Smith, E. B. Sirota, C. R. Safinya, and N. A. Clark. Structure of the L_β phases in a hydrated phosphatidylcholine multimembrane. *Phys. Rev. Lett.*

[16] D. Chapman, R. H. Williams, and B. D. Ladbrooke. Physical studies on phospholipids. iv. thermotropic and lyotropic mesomorphism of some 1,2-diacylphosphatidylcholines (lecithins). *Chem. Phys. Lipids*, 1:445–475, 1967.

[17] W. J. Sun, R. M. Suter, M. A. Knewtson, C. R. Worthington, S. Tristram-Nagle, R. Zhang, and J. F. Nagle. Order and disorder in fully hydrated unoriented bilayers of gel phase dppc. *Phys. Rev. E.*, 49:4665–4676, 1994.

[18] M. C. Rheinstädter, W. Häussler, and T. Salditt. Dispersion relation of lipid membrane shape fluctuations by neutron spin-echo spectrometry. *Phys. Rev. Lett.*, 97:048103 (4 pages), 2006.

[19] J. M. Carlson and J. P. Sethna. Theory of the ripple phase in hydrated phospholipid bilayers. *Phys. Rev. A*, 36:3359–3374, 1987.

[20] A. Schäfer, T. Salditt, and M. C. Rheinstädter. Atomic force microscopy study of thick lamellar stacks of phospholipid bilayers. *Phys. Rev. E*, 77:021905 (8 pages), 2008.

[21] V. A. Raghunathan and J. Katsaras. Structure of the $L_{c'}$ phase in a hydrated multilamellar system. *Phys. Rev. Lett.*, 74:4456–4460, 1995.

[22] J. F. Nagle and S. Tristram-Nagle. Structure of lipid bilayers. *Biochim. Biophys. Acta*, 1469:159–195, 2000.

[23] E. Nováková, K. Giewekemeyer, and T. Salditt. Structure of two-component lipid membranes on solid support: An x-ray reflectivity study. *Phys. Rev. E*, 74:051911 (9 pages), 2006.

[24] V. Luzzati and F. Husson. The structure of the liquid-crystalline phases of lipid-water systems. *J. Cell Biol.*, 12:207–219, 1962.

[25] T. Bayerl. Collective membrane motions. *Curr. Opin. Colloid Interface Sci.*, 5:232–236, 2000.

[26] S. Paula *et al.* Permeation of protons, potassium ions, and small polar molecules through phospholipid bilayers as a function of membrane thickness. *Biophys. J.*, 70:339–348, 1996.

[27] S. H. Chen *et al.* Collective dynamics in fully hydrated phospholipid bilayers studied by inelastic x-ray scattering. *Phys. Rev. Lett.*, 86:740–743, 2001.

[28] J. S. Hub, T. Salditt, M. C. Rheinstädter, and B. L. de Groot. Short range order and collective dynamics of DMPC bilayers. A comparison between molecular dynamics simulations, x-ray, and neutron scattering experiments. *Biophysical J.*, 93:3156–3168, 2007.

[29] H. Bary-Soroker and H. Diamant. Surface relaxation of lyotropic lamellar phases. *Europhys. Lett.*, 73:871–877, 2006.

[30] V.P. Romanov and S.V. Ul'yanov. Dynamic and correlation properties of solid supported smectic-a films. *Phys. Rev. E*, 66:061701 (9 pages), 2002.

[31] D. M. Engelman. Membranes are more mosaic than fluid. *Nature*, 438:578–580, 2005.

[32] N. Kučerka, J. D. Perlmutter, J. Pan, S. Tristram-Nagle, and J. Katsaras. The effect of cholesterol on short- and long-chain monounsaturated lipid bilayers as determined by molecular dynamics simulations and x-ray scattering.

[33] M. Patra *et al.* Under the influence of alcohol: The effect of ethanol and methanol on lipid bilayers. *Biophys. J.*, 90:1121–1135, 2006.

[34] E. Falck, M. Patra, M. Karttunen, M. T. Hyvönen, and I. Vattulainen. Impact of cholesterol on voids in phospholipid membranes. *J. of Chem. Phys.*, 121:12676–12689, 2004.

[35] T. P. W. McMullen and R. N. McElhaney. Physical studies of cholesterol-phospholipid interactions. *Curr. Opin. Coll. Int. Sci.*, 1:83–90, 1996.

[36] E. Falck, M. Patra, M. Karttunen, M. T. Hyvönen, and I. Vattulainen. Lessons of slicing membranes: Interplay of packing, free area, and lateral diffusion in phospholipid/cholesterol bilayers. *Biophys. J.*, 87:1076–1091, 2004.

[37] Z. Chen and R. P. Rand. The influence of cholesterol on phospholipid membrane curvature and bending elasticity. *Biophys. J.*, 73:267–276, 1997.

[38] N. Kučerka, D. Marquardt, T. A. Harroun, M. Nieh, S. R. Wassall, and J. Katsaras. The functional significance of lipid diversity: Orientation of cholesterol in bilayers is determined by lipid species. *J. Am. Chem. Soc.*, 131:16358–16359, 2009.

[39] F. J.-M. de Meyer, A. Benjamini, J. M. Rodgers, Y. Misteli, and B. Smit. Molecular simulation of the dmpc-cholesterol phase diagram. *J. Phys. Chem.*, 114:10451–10461, 2010.

[40] J. Pan, T. T. Mills, S. Tristram-Nagle, and J. F. Nagle. Cholesterol perturbs lipid bilayers nonuniversally. *Phys. Rev. Lett.*, 100:198103 (4pages), 2008.

[41] J. Henriksen, A. C. Rowat, E. Brief, Y. W. Hsueh, J. L. Thewalt, M. J. Zuckermann, and J. H. Ipsen.

[42] S. Feller *et al.* Nuclear overhauser enhancement spectroscopy cross-relaxation rates and ethanol distribution across membranes. *Biophys. J.*, 82:1396–1404, 2002.

[43] J. A. Barry and K. Gawrisch. Direct nmr evidence for ethanol binding to the lipid-water interface of phospholipid bilayers. *Biochemistry*, 33:8082–8088, 1994.

[44] H. V. Ly and M. L. Longo. The influence of short-chain alcohols on interfacial tension, mechanical properties, area/molecule, and permeability of fluid lipid bilayers. *Biophys. J.*, 87:1013–1033, 2004.

[45] H. Komatsu and S. Okada. Effects of ethanol on permeability of phosphatidylcholine/cholesterol mixed liposomal membranes. *Chem. Phys. Lipids*, 85:67–74, 1997.

[46] J. Nagle *et al.* Theory of passive permeability through lipid bilayers. *J. Gen. Physiol.*, 131:77–85, 2007.

[47] H. Träuble. The movement of molecules across lipid membranes: A molecular theory. *J. Membrane Biol.*, 4:193–208, 1971.

[48] J. F. Nagle and H. L. Scott. Lateral compressibility of lipid mono- and bilayers: Theory of membrane permeability. *Biochim. Biophys. Acta.*, 513:236–243, 1978.

[49] D. Huster *et al.* Water permeability of polyunsaturated lipid membranes measured by ^{17}O NMR. *Biophys. J.*, 73:855–864, 1997.

[50] T. Salditt, M. Vogel, and W. Fenzl. Thermal fluctuations and positional correlations in oriented lipid membranes. *Phys. Rev. Lett.*, 90:178101 (4 pages), 2003.

[51] R. R. Netz and Reinhard Lipowsky. Unbinding of symmetric and asymmetric stacks of membranes. *Phys. Rev. Lett.*, 71:3596–3599, 1993.

[52] M. Vogel, C. Münster, W. Fenzl, and T. Salditt. Thermal unbinding of highly oriented phospholipid membranes. *Phys. Rev. Lett.*, 84:390–393, 2000.

[53] U. Mennicke and T. Salditt. Preparation of solid-supported bilayers by spin-coating. *Langmuir*, 18:8172–8177, 2002.

[54] G. Georgiev, G. Georgiev, and Z. Lalchev. Thin liquid films and monolayers of dmpc mixed with peg and phospholipid linked peg. *Eur. Biophys. J.*, 35:352–362, 2006.

[55] Y.-H. M. Chan and S. G. Boxer. Model membrane systems and their applications. *Current Opinion in Chemical Biology*, 11:1–7, 2007.

[56] E. Sackmann. Supported membranes: Scientific and practical applications. *Science*, 271:43–48, 1996.

[57] C. Hamai, T. Yang, S. Kataoka, P. S. Cremer, and S. M. Musser. Effect of average phospholipid curvature on supported bilayer formation on glass by vesicle fusion. *Biophys. J.*, 90:1241–1248, 2006.

[58] M. Seul and M. J. Sammon. Preparation of surfactant multilayer films on solid substrates by deposition from organic solution. *Thin Solid Films*, 185:287–305, 1990.

[59] E. T. Castellana and P. S. Cremer. Solid supported lipid bilayers: From biophysical studies to sensor design. *Surface Science Reports*, 61:429–444, 2006.

[60] R. Richter, A. Mukhopadhyay, and A. Brisson. Pathways of lipid vesicle deposition on solid surfaces: A combined QCM-D and AFM study. *Biophys. J.*, 85:3035–3047, 2003.

[61] M. C. Hull, L. R. Cambrea, and J. S. Hovis. Infrared spectroscopy of fluid lipid bilayers. *Anal. Chem.*, 77:6096–6099, 2005.

[62] P. Sneil, R. R. Turkington, and R. Harris-Lowe. Simple, demountable, cryogenic, vacuum seal. *Rev. Sci. Instrum.*, 59:2618–2619, 1988.

[63] C. Li, D. Constantin, and T. Salditt. Biomimetic membranes of lipid-peptide model systems prepared on solid support. *J. Phys.: Condens. Matter*, 16:2439–2453, 2004.

[64] Z.-H. Wang and G. Jin. Silicon surface modification with mixed silanes layer to immobilize proteins for biosensor with imaging ellipsometry. *Colloids and Surfaces B: Biointerfaces*, 34:173–177, 2004.

[65] E. T. Vandenberg, L. Bertilsson, B. Liedberg, K. Uvdal, R. Erlandsson, H. Elwing, and I. Lundström. Structure of 3-aminoproyl triethoxy silane on silicon oxide. *Journal of Colloid and Interface Science*, 147:103–118, 1991.

[66] A. Wexler and S. Hasegawa. Relative humidity-temperature relationships of somem saturated salt solutions in the temperature range 0^oc to 50^oc. *Journal of research of the National Bureau of Standards*, 53:19–26, 1954.

[67] A.-J. Dianoux and G. Lander, editors. *Neutron Data Booklet, Second Edition*. Old City Publishing Group, Philadelphia, 2003.

[68] Sunil K. Sinha. Theory of inelastic x-ray scattering from condensed matter. *J. Phys. Condens. Matter.*, 13:7511–7523, 2001.

[69] L. Liang, R. Rinaldi, and H. Schober, editors. *Neutron Applications in Earth, Energy and Environmental Sciences*. Springer Science and Business Media, 2009.

[70] J. M. Carpenter. Pulsed spallation neutron sources for slow neutron scattering. *Nuclear Instruments and Methods*, 145:91–113, 1977.

[71] D. L. Price. *Methods of Experimental Physics: Neutron Scattering: Part A*. Academic Press, Inc., Orlando, Florida, 1986.

[72] M.. Laing. *An Introduction to the Scope, Potential and Applications of X-ray Analysis*. University College Cardiff Press, Cardiff, United Kingdom, 1981.

[73] J. T. Bushberg, J. A. Seibert, E. M. Leidholdt Jr., and J. M. Boone. *The Essential Physics of Medical Imaging: Second Edition*. Lippincott Williams & Wilkins, Philadelphia, PA, 2001.

[74] R. C. Pemberton and C. J. Mash. Thermodynamic properties of aqueous non-electrolyte mixtures ii. vapor pressures and excess gibbs energies for water + ethanol at 303.15 to 365.15 determined by an accurate static method. *J. Chem. Thermodynamics*, 10:867–888, 1978.